# Nuclear structure studies in the vicinity of the double-magic $^{132}$Sn nucleus

*Memoria que presenta para optar al grado de*
*Doctora en Ciencias Físicas*

**Lucía Cáceres**

*Dirigida por*

**Andrea Jungclaus**
**José Luis Egido de los Ríos**

Departamento de Física Teórica
Facultad de Ciencias
Universidad Autónoma de Madrid
Septiembre de 2008

# Contents

# Introduccion

Es conocido que el núcleo está formado por nucleones, protones y neutrones. Los primeros son partículas cargadas mientras que los segundos, como su propio nombre indica, son neutros. Si en el núcleo solo existiese la fuerza coulombiana, el sistema no estaría ligado debido a la fuerza repusiva de Coulomb. Por lo tanto, debe haber otra fuerza atractiva que ligue a los nucleones dentro del núcleo sobreponiendo la repulsion electromagnetica, la fuerza fuerte. No se conoce exactamente como esta fuerza actúa en los núcleos, pero a través de los resultados experimentales en conjunto con los modelos teóricos se esta empezando a entender sus propiedades. Una de las primeras observaciones experimentales fue la medida de las energías de ligadura por nucleón de diferentes isótopos. Se observó, que éstas aumentaban con la masa hasta alcanzar su máximo de 8.5 MeV/u a $A \sim 10 - 20$ y se mantenían constante una vez alcanzado este valor. Este resultado llevó a la conclusión de que la fuerza nuclear tiene la propiedad de saturación; ésto significa que a primera aproximación se puede considerar que la fuerza actúa a dos cuerpos únicamente. Otros resultados han sido de gran importancia para aumentar nuestro entendimiento de la estructura nuclear. La energía de separación de los protones aumenta cuando el número de neutrones también aumenta y disminuye cuando $Z$ aumenta. Se observa a su vez el mismo comportamiento con respecto a la energía de separación de los neutrones y el aumento o disminución del número de protones. Esta propieda tiene como consecuencia que los núcleos tienen tendencia a estar formados por un valor $N/Z$ que no sea extremo, por lo tanto, todos aquellos núcleos que tenga esta relación entre el número de protones y neutrones muy grande se consideran sistemas o núcleos exóticos y son inestables, desintegrándose $\beta$ hacia el valle de estabilidad. Con respecto a la energía de separación de protones o neutrones se observó además otro fenómeno interesante. Cuando el núcleo estaba formado por cierto número carasterístico de protones o neutrones, las energías de ligadura eran máximas y su valor disminuía abruptamente justo después de este número. Apareciendo los comunmente llamados números mágicos, que son exactamente aquellos números característicos de protones o neutrones donde este fenómeno es observado. Otros resultados experimentales que confirman la existencia de los números mágicos provienen de la medida de las energías de excitación del primer estado $(2^+)$ en los núcleos. Se observó que estas energías tenían un valor máximo justo en los número mágicos. Este efecto es causado por una energía de ligadura extra (apareamiento) que los nucleones sienten justo a números mágicos y llevó a la idea de organizar al los nucleones dentro del núcleo tal y como se encuentran los electrones dentro del átomo. La existencia de la energía de apareamiento se observa de forma mas explícita cuando se comparan la masa de núcleos con números pares de protones y neutrones con la masa de núcleos compuestos por par-impar número de nucleones. Esta fuerza de apareamiento es la causante de que el estado fundamental de los núcleos con números pares de nucleones este formado por el momento angular total antialineado $0^+$. Otra observación experimental es la masa de núcleos espejo (a saber, núcleos con el mismo $A$ pero número intercambiado de protones y neutrones). Esta masa es la misma si se suprime la repulsión colombiana, además los estados excitados en estos núcleos se encuentras más o menos a la misma energía, con lo que se concluye que la fuerza fuerte es independiente de la carga. Esto significa que la interacción entre $\pi - \pi$, $\nu - \nu$ y $\pi - \nu$ es equivalente, de esta manera los modelos nucleares pueden ser desarrollados en el formalismo de isospín, el cual considera a los protones y neutrones como diferentes estados del nucleón. Aunque haya bastantes características conocidas del núcleo, existen todavía preguntas que han de ser contestadas. El desarrollo de los aceleradores de partículas ha abierto nuevos campos de trabajo y está permitiendo explorar los límites de la tabla nuclear acercándonos a las líneas de goteo de protones y empezando a aproximar a la de los neutrones. Con ello, se han observado diferentes características en estos núcleos exóticos. De entre todas ellas, la evolución y el reordenamiento de los niveles de energía de las partículas han despertado el interés tanto de los físicos experimentales como de los teóricos.

# Chapter 1

# Introduction

As it is well known the nucleus is formed by nucleons, protons and neutrons. The first are charged particles while the second are neutral. If in the nucleus the only existing force would be the Coulomb force, the system would not be bound due to the Coulomb repulsion. Therefore there must be another strong attractive interaction which binds the nucleons together overcoming the electromagnetic repulsion, the strong force. This force is not completely understood, but there is some experimental evidence which gives a glance of its main characteristics.

One of the empirical observations were the measurement of the binding energies per nucleon of different isotopes. It is noticed that first the binding energy increases with the mass number, reaching a maximum of 8.5 MeV/u at $A \sim 10 - 20$ and remains roughly constant afterwards (Figure 1.1). This observation lead to the conclusion that the nuclear force saturates, meaning that in first approximation it can be considered as a two body interaction between nucleons. Some other experimental results have been of outstanding importance to increase the understanding of nuclear structure. The proton separation energies ($S(p)$) increase when increasing the neutron number and decrease when $Z$ increases. A similar behavior is found for the neutron separation energy with respect to adding and removing protons and neutrons, respectively. This effect of the nuclear force prevents that the nucleus is formed with an extreme proton-to-neutron ratio ($N/Z$). Therefore all systems with extreme $N/Z$ value are considered exotic and are instable $\beta$-decaying towards the valley of stability. Additionally, the proton and neutron separation energies show a particularly large value for certain numbers of protons and neutrons and then a sudden drop. The numbers were this phenomenon appears are called *magic numbers*. More evidence supporting the existence of magic numbers arises from the measurement of the first excited states, as shown in Figure 2.6 for nuclei with $Z = 46 - 60$. The $2^+$ energies have larger values at the magic numbers and decrease rapidly afterwards. This effect is caused by an extra binding energy (*pairing*) that the nucleons feel at those numbers, leading to the idea to structure the nucleons inside the nucleus as the electrons are inside the atom. The pairing force is exhibited when looking to mass differences between nuclei with odd-even neutron-proton number and even-even nucleon numbers (Figure 1.2). The pairing interaction is the cause why nucleons pair to maximun antialigned total angular momentum in the ground state of the nucleus. Consequently the ground state of all even-even nuclei has spin and parity $0^+$. The curve shown in Figure 1.2 represents the empirical $12\mathrm{A}^{-1/2}$

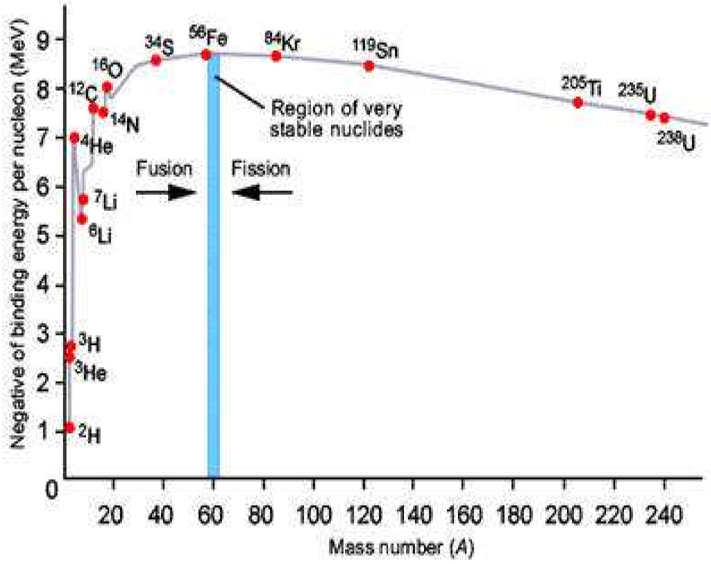


Figure 1.1: *Binding energy per nucleon. The solid curve is the result of the semi-empirical mass formula.*

mass dependence of the pairing force.

The masses of mirror nuclei (i.e. nuclei with the same $A$ but exchanged number of protons and neutrons) are the same once the Coulomb repulsion is subtracted. In addition the excited states in these nuclei are roughly at the same energy. This observation lead to the conclusion that the nuclear force is charge independent, meaning that $\pi$-$\pi$, $\nu$-$\nu$ and $\pi$-$\nu$ are equal, and therefore the nuclear models could be developed in the isospin formalism (considering the proton and the neutron as two different states of the nucleon), simplifying considerably the calculations. Although there are some general characteristics of the nuclear force known, there are still many questions to be answered. The new development of radioactive beam facilities opens new fields of research and allows to explore the extremes of the nuclidic chart. By producing exotic nuclei, the changes in nuclear structure when approaching the limits, i.e. systems with extreme number of protons and/or neutrons, can be studied. Among all the new effects observed at these limits, the shell evolution and reordering of the single particle energy levels have awaken the interest of both theoreticians and experimentalists.

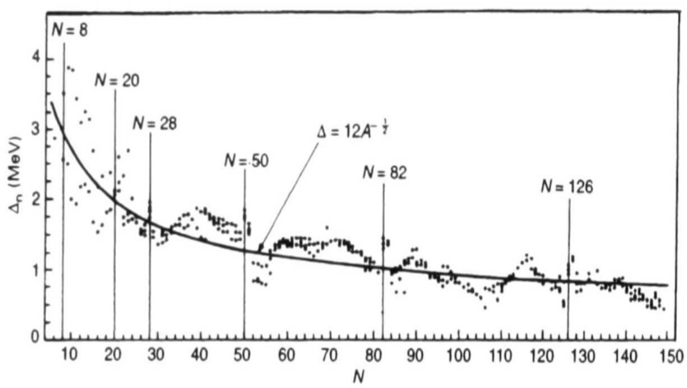


Figure 1.2: *Mass difference between nuclei with odd-even neutron-proton numbers and even-even nucleon numbers. The curve represents the empirical* $12A^{-1/2}$ *mass dependence of the pairing force. The extra binding at the magic numbers is visible.*

# Chapter 2

# Motivation

The development of the new radioactive beam facilities allowed to access experimentally nuclei with extreme $N/Z$ ratio, reaching the proton drip line and going towards the neutron drip line. The experimental information obtained reveal important differences with respect to the nuclear structure of nuclei in the valley of stability, as for example the evolution of the single particle energy levels. This caused that the nuclear structure models had to be reviewed in order to reproduce the experimental data. Although the experimental information is increasing considerably in recent years, there is a need for further experiments in order to provide the unknown parameters required for the different model calculations. Little information is available concerning mass measurements in the $^{132}$Sn region which is a necessary input for Large Scale Shell Model (LSSM) calculations as well as for the r-process solar abundance models. Additionally, the decay pattern of the waiting point nuclei below $Z = 50$ remain unknown. Those are examples of the needs of experimental information for the nuclear models. In this chapter, the basic concepts of the nuclear shell model will be reviewed in Section 2.1. A description of the electromagnetic transitions will be given in Section 2.2 followed by an overview of nuclear isomerism. The nuclear structure characteristics of the $^{132}$Sn region will be reported in Section 2.4, with special emphasis on the aspects related to this thesis work.

## 2.1 The Nuclear Shell Model

The correct description of the shell structure of atomic nuclei was first given by Goeppert-Mayer [1, 2, 3], Haxel, Jensen and Suess [4]. The authors proposed a model of independent nucleons confined in an isotropic harmonic oscillator plus a spin-orbit term and an orbit-orbit potential that corrects for the bad surface behavior of the harmonic oscillator. Assuming two-body interactions the nuclear Hamiltonian can be described as a sum of the kinetic-energy terms and a potential which describes the two-particle interaction, see References [5, 6] among others,

$$H|\psi >= (T + V)|\psi >= \left[ \sum_{i=1}^{A} T(k) + \sum_{i>k=1}^{A} V_{i,k} \right] |\psi >, \tag{2.1}$$

where $T_i$ is the kinetic energy of the i-th nucleon, $V_{ij}$ is the two-body interaction and $A$ is the number of nucleons in the nucleus. By introducing a central potential ($U(r_i)$) in the Hamiltonian, the many-body problem can be reduced to an independent particle motion Hamiltonian and a residual interaction treated as perturbation of the system:

$$H = \sum_{i=1}^{A}(T_i + U(r_i)) + \left[\sum_{i>k=1}^{A} V_{i,k} - \sum_{i=1}^{a} U(r_i)\right] = H_0 + H_1 \tag{2.2}$$

where $H_0$ describes the independent particle motion and $H_1$ is the residual interaction which accounts for the fact that the particles do not move completely independent. The eigenstates obtained when resolving the Schrödinger equation with $H_0$ lead to the single-particle wave functions and its eigenvalues are the single particle energies. The single particle/hole states are among the basic ingredients in shell model calculations and are normally taken from experimental values.

The dimension of the residual interaction Hamiltonian increases considerably with the number of nucleons and their possible coupling, which causes that only systems with $A \leq$ *12* [7, 8] can be fully calculated. For larger masses, the definition of a hard core, consisting of inactive particles, is introduced. This will reduce the matrix dimensions to be diagonalized in the calculation. The matrix dimension is related to the model space chosen. This model space consists of a number of shell model orbitals, the occupancies of these orbitals and valence nucleons outside the core. Only the valence nucleons give the spin and energy of states with respect to the ground state of the core nucleus, therefore for each region of the Segré chart different model spaces have to be considered.

The basic concepts for the extraction of the residual interaction two-body matrix elements (TBME) will be explained in the following sections. With the restriction to two-body interactions the interaction energy in a many-particle configuration can be reduced to a weighted sum over TBME only. In a single-j shell the following expression can be deduced,

$$< j^n J\alpha | V_{res} | j^n J\alpha' > = \sum_{J'} c_2(n, j, \alpha, \alpha', J, J') < j^2 J' | V_{res} | j^2 J' >, \tag{2.3}$$

where $j$ is the angular momentum of a single nucleon, $J$ is the total angular momentum, $\alpha$ and $\alpha'$ are the rest of the quantum numbers necessary to define the sate and $n$ is the number of nucleons coupled to angular momentum $J$. The coefficients $c_2(n, j, \alpha, \alpha', J, J')$ relate the angular momentum coupling coefficients and fractional parentage coefficients (see Reference [9] for a brief description).

There are two common approaches to extract the TBME, the empirical shell model and the realistic shell model.

### 2.1.1 Empirical Shell Model

The TBMEs are extracted from experimental data, in the simplest way from the binding energy difference between a doubly-closed shell nucleus and its one and/or two particle/hole neighbours. Another method to extract the TBMEs for not too large model spaces is a $\chi^2$-fit to a set of experimental binding and excitation energies of states that can be assigned to the model space ([10, 11] among many others). The fitting procedure can be simplified by assuming a schematic interaction that can be defined by few parameters (i.e. Yukawa [12], Gaussian [12] and others).

The calculated energies (pairing, level density) and electromagnetic transition rates (configuration mixing) have discrepancy with the experimental values. A detailed description can be found in Reference [13]. The wave functions calculated with empirical interactions have little resemblance to the true wave functions.

### 2.1.2 Realistic Shell Model

In the first step for the extraction of the TBMEs, the nucleon-nucleon scattering data are fitted to the experimental data. The strong repulsive core in the nucleon-nucleon interaction is eliminated and the G-matrices are produced. The TBMEs are extracted from the G-matrices for a given model space, therefore this method is model dependent. The calculated energy levels of nuclei close to the shell closure are in good agreement with the experimental values. Since the single particle energy levels can not be extracted they are normally taken from experimental data or extrapolation from known single particle states if no experimental information is available. The reasons why the single particle energy levels can not be extracted are [6]:

- The single particle energy levels are affected by particle-hole excitations across the closed shell
- Three-body forces are not included

The experimental results presented in Chapter 5 are compared to the realistic shell model calculations (refered from now on as Large Scale Shell Model, LSSM calculations), which provide information on the wave functions of the states measured. A detailed description of this type of calculations can be found in Reference [14].

## 2.2 Electromagnetic transitions

The main source of information for the spin and parity assignment of states is obtained from the study of electromagnetic transitions, since the electromagnetic interaction is well understood, in contrast to the nuclear forces [15]. The study of $\gamma$-ray emission in combination with its competing process, internal electron conversion, has become the standart technique of nuclear spectroscopy.

### 2.2.1 The internal electron conversion

Internal conversion is an electromagnetic process competing with $\gamma$ emission. The electromagnetic fields of the nucleus interact with the atomic electrons and cause one of those electrons to be emitted from the atom. The probability of this process to occur is inversely proportional to the energy difference between initial and final state. Therefore a reduction of the $\gamma$ ray intensity is expected for low energy transitions. The internal conversion coefficient is defined as the probability of an electron emission relative to $\gamma$ emission, thus the total transition intensity is

$$I_t = I_\gamma(1+\alpha); \tag{2.4}$$

where $I_t$,$I_\gamma$ are the total and the measured $\gamma$ transition intensity, respectively. $\alpha$ is the total conversion coefficient. This coefficient can be extracted experimentally in the case of a $\gamma$ ray when no competing branches formed by $\gamma$-rays also converted are emitted in parallel (Section 4.2). The conversion coefficients are specific for each $\gamma$ energy, multipolarity, atomic number and type of the transition and can help in assigning the spin/parity of excited states. By comparing the theoretical and experimental conversion coefficients it is possible to determine the character (i.e. type and multipolarity) of the $\gamma$ ray emitted. In the case that the $I^\pi$ of one of the levels involved in the decay is known, the possible spin and parity assignment for the other level can be inferred by means of the selection rules for electromagnetic transitions [16].

### 2.2.2 Electromagnetic transition operators

The decay rate for emission of a photon of a given multipole type, summed over the magnetic substates of the photon and the final state, is given by [17]

$$T(\sigma\lambda; I_i \rightarrow I_f) = \frac{8\pi(\lambda+1)}{\lambda\left[(2\lambda+1)!!\right]^2}\frac{1}{\hbar}\left(\frac{E_\gamma}{\hbar c}\right)^{2\lambda+1} B(\sigma\lambda; I_i \rightarrow I_f) \tag{2.5}$$

where $\sigma$ is the multipole type, $\lambda$ is the multipole order, $I_i$ and $I_f$ are the initial and final states, respectively, $E_\gamma$ is the energy of the photon emitted in MeV and $B(\sigma\lambda; I_i \rightarrow I_j)$ is the reduced transition probability. The decay rate can be related to the half-life as

$$T(\sigma\lambda; I_i \rightarrow I_j) = \frac{ln2}{T_{1/2}(1+\alpha)}. \tag{2.6}$$

In this equation $T_{1/2}$ is the half-life of the initial state and $\alpha$ is the total conversion coefficient of the $\gamma$ ray emitted. From Equation 2.5 and Equation 2.6 the expression to calculate $B(\sigma\lambda; I_i \rightarrow I_j)$ can be extracted

$$B(\sigma\lambda; I_i \rightarrow I_f) = \frac{\hbar ln2}{T_{1/2}(1+\alpha)}\frac{\lambda\left[(2\lambda+1)!!\right]^2}{8\pi(\lambda+1)}\left(\frac{\hbar c}{E_\gamma}\right)^{2\lambda+1}. \tag{2.7}$$

The reduced transition probability is given in units of e$^2$(fm)$^{2\lambda}$ for the electric transitions and $(\mu_N = \frac{e\hbar}{2M_pc})^2(\text{fm})^{2\lambda-2}$ for magnetic transitions. It is common to relate the experimental reduced transition probabilities with the corresponding Weisskopf estimates [18]. These estimates are based on a model with the following assumptions [19]:

- The nucleus consists of an inert core plus one active particle.
- The transition takes place between states $j_i = L \pm 1/2$ and $j_f = 1/2$
- The radial parts of the initial- and final-state wave functions are constant inside the nucleus and vanish outside.

The corresponding reduced transition probabilities are given by [17]

$$B_W(E\lambda) = \frac{(1.2)^{2\lambda}}{4\pi}\left(\frac{3}{\lambda+3}\right)^2 A^{2\lambda+3}e^2(fm)^{2\lambda} \tag{2.8}$$

$$B_W(M\lambda) = \frac{10}{\pi}(1.2)^{2\lambda-2}\left(\frac{3}{\lambda+3}\right)^2 A^{(2\lambda-2)/3}\left(\frac{e\hbar}{2M_pc}\right)^2(fm)^{2\lambda-2} \tag{2.9}$$

Since it is assumed that only a single nucleon participates in the transition a large deviation of the experimental reduced transition probability values compared to their Weisskopf estimate might be an indication of a certain degree of collectivity for the transition.

The reduced transition probability is related to the electromagnetic one-body operator as [17]

$$B(\sigma\lambda; I_i \to I_f) = \frac{1}{2I_i+1}| < I_f\alpha||O^{\sigma\lambda}||I_i\alpha_i > |^2 \tag{2.10}$$

where $O^{\sigma\lambda}$ the electromagnetic operator of order $\lambda$. Similar to the two-body interactions (Section 2.1), the reduced matrix elements of the one-body operator can be decomposed into a sum over single particle transition matrix elements [6]

$$< I_f\alpha||O^{\sigma\lambda}||I_i\alpha_i >= \sum_{j_f\alpha_f j_i\alpha_i} c_1(l_f, j_f, I_f, \alpha_f, l_i, j_i, I_i, \alpha_i) < l_fj_f||O^{\sigma\lambda}||l_ij_i > \tag{2.11}$$

The coefficients $c_1$ are calculated from the amplitude of the configurations composing the wave function. The absolute value of the reduced matrix element is invariant with respect to the exchange of the initial and final state, therefore the inverse transition will follow the expression [20]

$$B(\sigma\lambda; I_f \to I_i) = \frac{2I_i+1}{2I_f+1}B(\sigma\lambda; I_i \to I_f) \tag{2.12}$$

From Equation 2.7 and 2.10 the experimental and theoretical reduced transition probabilities can be compared. In general it is observed that the experimental values are larger than the calculated ones. This effect has its origin in the fact that in the calculations not all the space is considered, i.e. the selection of a model space. In order to account for it, an effective operator is defined such that the same results are obtained in the complete configuration space and in the restricted model space [21]. Therefore a new renormalization of the electromagnetic operator is necessary depending on the model space selected. In case of the *E2* operator, the loss of theoretical strength can be compensated by introducing proton and neutron effective charges, typical values are 1.5 $e$ for protons and 0.5 $e$ for neutrons. The difference between the effective charge and the free nucleon values is defined as polarization charge. This is understood as virtual particle excitations of the closed shells to states beyond the model space. For the *M1* operator the orbital g-factor is changed by adding $\pm0.1$ to the neutron and proton free values [22, 23, 24], respectively.

## 2.3 Nuclear Isomerism

An excited state is considered isomeric when its half-life is long compared to the half-life of the neighbouring states. The typical decay time of a state is of the order of *ps*, therefore any state with a lifetime longer than that can be considered isomeric. Information on the nuclear structure can be extracted by the study of the decay pattern of these isomeric states. The existence of isomeric states has been prooven all along the nuclidic chart, from the very proton rich nuclei up to the very neutron rich systems, although the reason for their formation might be different. In general, an isomeric transition occurs when the wave function of the initial state is very different from that of the final state. In the regions close to double-magic nuclei, the coupling of the valence particles or holes to the core nucleus gives rise to mainly three types of isomerism, namely; spin gap isomers, seniority isomers and isomers due to low transition energy between the initial and final states.

Spin gap isomers are formed when the spin difference between the initial and final state is large. The multipolarity of the $\gamma$ transition will be high and therefore the state from which it decays becomes isomeric. One example of this type of isomer is found in $^{130}$Sn. The spin difference between the $7^-$ and the $2^+$ levels at 1947 keV and 1221 keV excitation energy, respectively, is $5\hbar$. The character of the 726 keV $\gamma$ transition would be E5. Thus the $7^-$ state undergoes $\beta$-decay to $^{130}$Sb with a half-life of 1.7 m [25, 26].

Seniority isomers are formed when the maximun spin for a given seniority (number of unpaired particles in a state of angular momentum $J$) and configuration is reached. This type of isomers are found generaly close to doubly magic nuclei and in general the $\gamma$ transition is of stretched $E2$ character. The formation of a seniority isomer can be undestood as follows: Considering a nucleus with two valence nucleons in orbitals $j_1$ and $j_2$ which couple to spin $J = j_1 + j_2 .... |j_1 - j_2|$. In aussence of the residual interaction, all these levels will be degenerated, in the presence of the residual interaction the degeneracy will be bronken and the level shifting if delta interaction is taken as apoximation for the residual interaction will be [9]

$$\Delta E(j_1 j_2 J) = F_R(n_1 l_1 n_2 l_2) A(j_1 j_2 J). \tag{2.13}$$

where $n_{1,2}$ and $l_{1,2}$ referes to the quantum numbers of the nucleons in the $j_1$ and $j_2$ orbitals. $\mathrm{F}_R$ depends only on the radial coordinates while $A$ results from an integration over the angular coordinates. In the case of the two like nucleons (either two protons or two neutrons) in the same orbital the $\mathrm{F}_R$ and $A$ function reduce to

$$F_R(nl) = \frac{1}{4\pi} \int \frac{1}{r^2} R^4_{nl}(r) dr \tag{2.14}$$

$$A(j^2 j) = \frac{(2j+1)^2}{2} \begin{pmatrix} j & j & J \\ \frac{1}{2} & -\frac{1}{2} & 0 \end{pmatrix}^2$$

The $3-j$ symbol in the $A$ expression causes the reduction in the levels energy spacings as the excitation energy increasses. When the maximum spin for a given configuration is reached, the difference in energy to the next lower state is minimum and the $E2$ transition became hindered. An example of this type of isomers is the $8^+$ seniority isomer in $^{98}$Cd which decay by a 148 keV $E2$ transition [27] with an isomeric half-life of 170 ns [28].

Isomers can be formed due to the dependence of the reduced transition probability on the $\gamma$ ray energy (Equation 2.7) when the energy difference between the initial and final states is small. This type of transition are normally highly converted for heavy ions, therefore the measurement of the conversion coefficients is crucial to determine the multipolarity of such $\gamma$ rays.

In some cases the effects are combined. One example of an isomer formed due to a spin gap and low transition energy is found in $^{131}$Sn [30, 31], one neutron hole in $^{132}$Sn. The spin difference between the $11/2^-$ first excited state and the $3/2^+$ ground state in $^{131}$Sn [30, 31] is $4\hbar$. Thus a $\gamma$ ray energy of 69 keV [31] must carry $4\hbar$ angular momentum. The probability of this $\gamma$-ray to be emitted is very small, and in any case it will be highly converted. Instead, the $\nu(h_{11/2})^{-1}$ isomer undergoes $\beta$-decay to $^{131}$Sb.

The $10^+$ isomeric state formed by the maximum alignment of the two neutron holes in the $h_{11/2}$ orbital in $^{128}$Sn [26, 29], decays by an 79 keV $E2$ transition to the $I^\pi = 8^+$ state with a half-life of 2.69 $\mu$s. This isomer is a combination of the seniority and low energy type isomers.

## 2.4 Nuclear Structure near the doubly-magic $^{132}$Sn

The research topic of this thesis is the study of the nuclear structure near the doubly-magic nucleus $^{132}$Sn. This region of nuclei has awaken the interest of both theoreticians and experimentalists due to its richness of nuclear properties. The Sn isotopes form the longest isotopic chain in the nuclidic chart serving as a test ground for nuclear structure models. Additionally, the exotics of such nuclei made their production an experimental challenge. In the following sections, an overview of the region with its main nuclear structure characteristics will be given. A special care is taken on the aspects related to this work; the monopole migration of the SPE levels, the effect of the neutron excess on the nuclear potential, the anomalous behavior of the $2^+$ excitation energies in the Cd chain when approaching the $N = 82$ shell closure, the consequences of the nuclear structure with respect to the r-process solar abundance calculations and finally the interpretation of the experimental results in terms of a possible $N = 82$ shell quenching.

### 2.4.1 Single particle energy levels in $^{132}$Sn

The eigenvalues of the nuclear Hamiltonian with the spin-orbit term included yield the single particle energy levels and the reproduction of the so called "magic numbers". Nuclei with a magic number of protons or neutrons have been observed to be particularly stable. It has been noticed over the past 20 years, that the ordering of the single particle states for nuclei in the valley of stability might change when approaching exotic systems, i.e. nuclei with large proton or neutron excess. This phenomenon is known as shell evolution. There are two processes which have been predicted to lead to the reordering of the single particle levels far off stability. The so called monopole migration [33] and the change of the shape of the nuclear potential shape due to neutron excess [34]. The first mechanism is valid for both proton and neutron rich nuclei while the

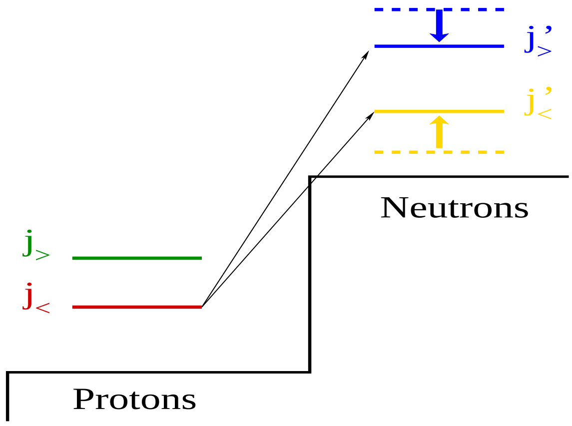


Figure 2.1: *Energy shifting of the neutron single particle levels when filling the proton $j_>$' orbital. See text for details.*

second mechanism has been predicted only for the very neutron rich systems. Without entering into the mathematical formalism of both mechanisms, the physical concepts behind them will be presented in the following.

The monopole migration has been attributed to the tensor part of the nucleon-nucleon interaction. It determines the evolution of single particle/hole energies from one closed shell to the next one. The monopole for a specific multiplet (j, j') is defined by [33, 32]

$$V^T_{j,j'} = \frac{\sum_J (2J+1) < jj'J|V|jj'J >_{JT}}{\sum_J (2J+1)}, \tag{2.15}$$

where $< jj'J|V|jj'J >_{JT}$ are the TBME of two nucleons coupled to total angular momentum $J$ and isospin $T$. Assuming that $j'$ and $j$ refers to a neutron and proton orbitals, respectively, the shift of the single particle energy of $j$ is given by [33]

$$\Delta\epsilon_p(j) = \frac{1}{2}\{V^{T=0}_{j,j'} + V^{T=1}_{j,j'}\}n_n(j') \tag{2.16}$$

where $n_n(j')$ is the expectation value of the number of neutrons in the orbital $j'$, $\Delta\epsilon_p(j)$ is the shift of the proton single particle level $j$ when filling the neutron orbital $j'$, $V^{T=0}_{j,j'}$ and $V^{T=1}_{j,j'}$ are the monopole TBME when the nucleons are coupled to isospin $T=0$ or $T=1$, respectively. The proton-neutron monopole tensor interaction is three times stronger than the T=1 interaction [33]. A similar equation is valid in the case of the shift of a neutron single particle energy. The single particle energies with monopole effect included are called effective single particle energy levels (ESPE).

A schematic representation of how the monopole drives the ESPEs is shown in Figure 2.1. Assuming that the proton orbital $j_<$' is being filled, as consequence of the tensor force the energy of the neutron state $j_>$ will be reduced while the $j_<$ orbital will increase in energy, with $j_>$ and $j_<$ referring to $j=l+1/2$ and $j=l-1/2$, respectively. In other words, the tensor monopole interaction causes a reduction in the spin-orbit splitting of the spin-flip partners $j_<$ and $j_>$. In general, one could say that $j_<$ and $j_>$' or $j_>$ and $j_<$' orbitals attract each other while $j_>$ and $j_>$' or $j_<$ and $j_<$' repeal each other. The criteria for strong monopoles are [32]:

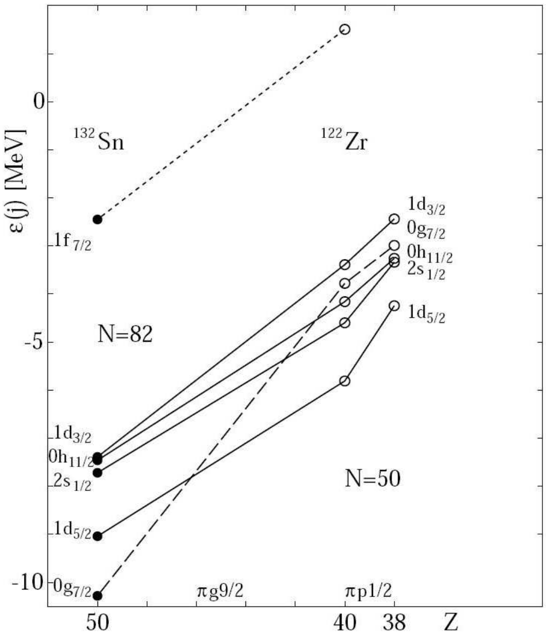


Figure 2.2: *Evolution of the N=82 shell gap bellow $^{132}$Sn as a function of Z. Measured and extrapolated values are indicated by filled and open circles, respectively [36].*

- The interacting nucleons are spin-flip partners
- Δl = 0,1,2
- The radial wave function of the nucleons should have the same number of nodes to maximize the spacial overlap.

When the ESPEs are unknown, they can be extracted by extrapolating experimental data. For example in $^{130}$In, the $1^-$ and $10^-$ states formed by $\pi g_{9/2}^{-1} \nu h_{11/2}^{-1}$ coupling are pure states [39]. Their excitation energy is close related to the $\pi g_{9/2}^{-1} \nu h_{11/2}^{-1}$ monopole. This monopole TBME are modified in the calculations to reproduce the experimental energies of the $1^-$ and $10^-$ states. This value of the monopole will serve to calculate the monopole migration of the $\nu h_{11/2}$ orbital when emptiying the $\pi g_{9/2}$ or viceversa (i.e. $\nu h_{11/2}$ ESPE in $^{129}$Cd or the $\pi g_{9/2}$ ESPE in $^{129}$In). The position of the ESPE levels is driven by the monopole interaction and their evolution from one nucleus to another will be determined by the occupation of the orbitals (Equation 2.16).

An example of the calculated monopole migration for the $N = 81$ neutron-hole orbitals is shown in the Figure 2.2. The single particle energies in $^{132}$Sn are known [35] and are represented by filled circles, while the extrapolated values are open symbols [36]. The extraponation done by H. Grawe mades use of Equation 2.16 employing an interaction determined for a $^{132}$Sn core while the interaction of the $\pi(g_{9/2}, p_{1/2})$ with the $\nu f_{7/2}$ orbital is extrapolated from the $^{208}$Pb region [36]. The evolution of neutron ESPE levels is dominated by the emptying of the $\pi g_{9/2}$ orbital towards $^{122}$Zr, in particular the $g_{7/2}$ orbital is affected which moves up to the Fermi surface at $Z = 40$, while the size of the shell gap stays constant.

The proton and neutron single particle energy levels in $^{100}$Sn and $^{132}$Sn are shown in Figure 2.3. The single particle energy levels for $^{100}$Sn are from Reference [37] while the ones for $^{132}$Sn are from experimental data [38]. When filling the $\nu h_{11/2}$ orbital the strong $\nu h_{11/2}$ -$\pi g_{7/2}$ monopole causes the exchange of the proton $g_{7/2}$ and $d_{5/2}$ orbitals. As it can be seen in Figure 2.3, the first level above the *Z=50* shell gap in $^{132}$Sn is the $g_{7/2}$ orbital in contrast to $^{100}$Sn where the $d_{5/2}$ orbital is lower in energy.

The other mechanism which might affect the SPE levels is predicted only for neutron rich nuclei. In these nuclei the neutron density becomes diffuse and the wave function has a larger extension due to the neutron excess. The neutron excess causes that the shape of the nuclear potential evolves from Woods-Saxon to more harmonic oscillator type restoring the level sequences of the latter. This causes that orbitals with large-l shift towards higher energy and the spin-orbit splitting is reduced. The reordering of the single particle energy levels in neutron rich nuclei is exemplified in Figure 2.4.

This effect has been interpreted as a reduction in the spin-orbit coupling strength caused by a strong interaction between the bound orbitals and the *low-j* continuum states. As a consequence, the $N = 82$ shell gap has been predicted to quench when approaching $Z = 40$ [34].

The results from Hartree-Fock-Bogoliubov calculations of the two-neutron separation energy, which is a measure of the neutron shell gap, along the $N = 82$ isotones are presented in Figure 2.5. The experimental and extrapolated shell gaps shown in Figure 2.2 are represented by vertical bars. It is clear that they are underestimated in the calculations [32].

The quenching of the $N = 82$ shell gap at $^{122}$Zr is only predicted by the mean field calculations. Some experimental results have been interpreted as an evidence of shell quenching at $N = 82$ and $Z = 48$ [40, 41], close to the $^{132}$Sn doubly-closed shell nucleus. This dramatic change of the nuclear structure could only be caused by the diffuseness of the nuclear potential and can not be attributed to monopole migration of the ESPE levels. In this thesis work, the question whether there is shell quenching "south" of $^{132}$Sn at $Z = 48$ will be answered.

### 2.4.2 $\beta$-decay Spectroscopy Studies

Nuclei with proton or neutron excess are known to be unstable, they $\beta$-decay towards the valley of stability. The nuclear $\beta$-decay is caused by the weak interaction the strength of which is orders of magnitude smaller than the one of the electromagnetic interaction. It is therefore common to use perturbation theory for the transition rate calculations. In the weak interaction process, a particle is emitted which characterizes the type of the decay, either an electron ($e^-$) then it is referred to as $\beta^-$-decay and occurs for nuclei with neutron excess or a positron ($e^+$) being defined as $\beta^+$-decay suffered by nuclei at the proton rich side of the nuclidic chart. For the latter, electron capture is a competing process, in this case, an $e^-$ is capture by the nucleus. Additionally, a neutrino $\nu$ or antineutrino $\overline{\nu}$ is emitted during the processes. The different decay channels are

$$ {}_Z X_N \rightarrow_{Z+1} X_{N-1} + e^- + \overline{\nu} \tag{2.17} $$

$$ {}_Z X_N \rightarrow_{Z-1} X_{N+1} + e^+ + \nu \tag{2.18} $$

$$ {}_Z X_N + e^- \rightarrow_{Z-1} X_{N+1} \tag{2.19} $$

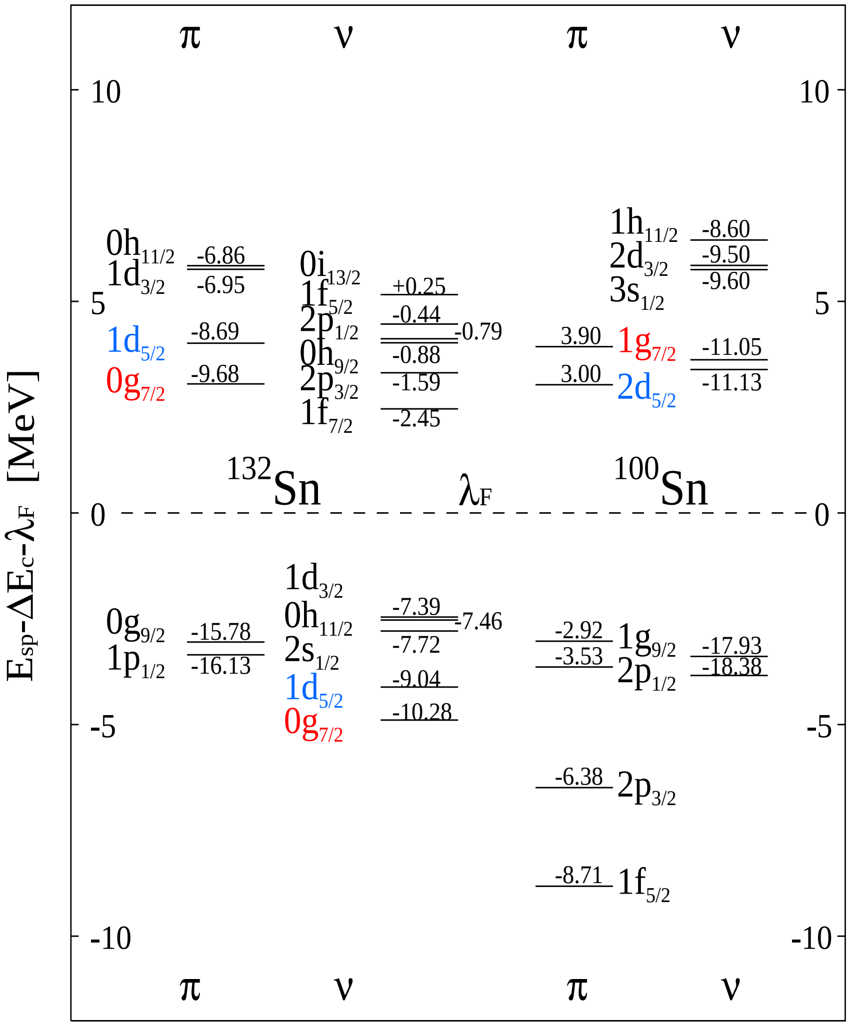


Figure 2.3: *Single particle energy levels in* $^{132}$*Sn [38](left) and* $^{100}$*Sn [6](right). The energies are normalized to the middle of the shell gap* ($\lambda_F$) *which eliminates the Coulomb energy difference* $\Delta E_C$*. The numbers quoted are the absolute single-particle energies including the Coulomb shift.*

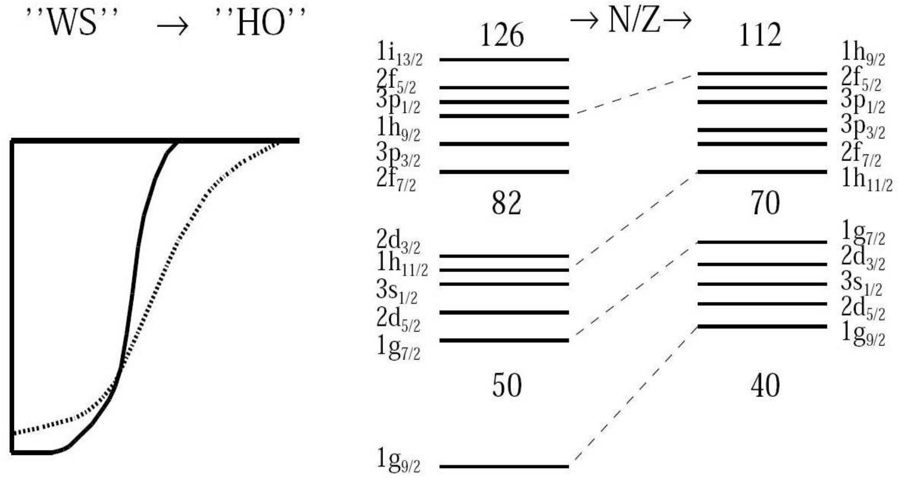


Figure 2.4: *Evolution of the SPE from N=Z towards N/Z»1. The neutron excess causes that the shape of the potential changes from Woods-Saxon to more harmonic oscillator type [32, 34].*

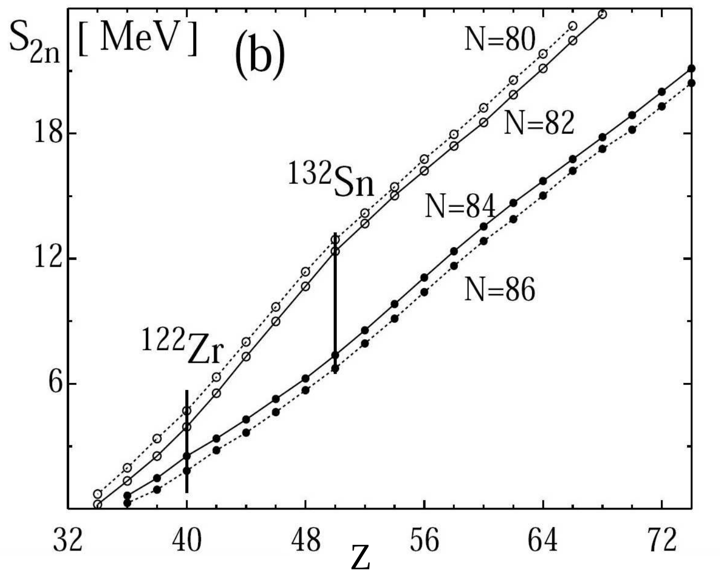


Figure 2.5: *Hartree-Fock mean field calculations of the two-neutron separation energy. The vertical bars are the experimental or shell model extrapolated values for the shell gap [34].*

for the $\beta^-$, $\beta^+$ and electron capture process, respectively.

The $\beta$ transitions are categorized in two types, the so-called allowed transitions and the forbidden transitions. In the first type the nucleons are considered non relativistic and the wave functions of the emitted particles are evaluated at the origin while in the second type those approximations are not applied [42]. Taking into account that the orbital angular momenta of the nucleons are not affected in allowed $\beta$-decay, in this type of transition none of the nucleons can make the single-particle transformation $l_i j_i \rightarrow l_f j_f$ with $l_i \neq l_f$.

The beta transition probability T($\beta$) depends on two different matrix elements and can be written as

$$T(\beta) \propto G_V^2 < M_F >^2 + G_A^2 < M_{GT} >^2, \tag{2.20}$$

where G$_V$ and G$_A$ are the vector and axial-vector coupling constants and $< M_F >$ and $< M_{GT} >$ are the Fermi and Gamow-Teller matrix elements, respectively.

The Fermi operator acts exclusively on the isospin component of the wave functions and is completely independent of the spacial part of the initial and final state wave functions. It is model independent assuming isospin as a good quantum number. Due to the isospin dependence, the Fermi decays are only possible between isobaric analogue states. The Gamow-Teller operator acts additionally to the isospin on the spin component of the wave function. Hence, in a Fermi transition there is no transfer of angular momentum between nucleons and leptons, while in the Gamow-Teller transitions one unit of angular momentum is transferred when allowed transitions are considered only [43].

The total $\beta$-decay rate for the decay from one nuclear state to another is obtained after integration over the electron energy and therefore depends on the maximum energy available for the decay process. It is common to express T($\beta$) in terms of the comparative half-life value $ft$ as

$$f(Z,W)t = f(Z,W)\frac{ln2}{T(\beta)} = \frac{6147}{< M_F >^2 + \left(\frac{G_A}{G_V}\right)^2 < M_{GT} >^2} \tag{2.21}$$

where $f(Z,W)$ is the known statistical function of a $\beta$ transition energy which depends on the atomic number $Z$ and the transition energy $W$, tabulated for a given element in [44, 45], and $t$ is the partial half-life for a $\beta$ transition of intensity $I_\beta$ ($t = T_{1/2}/I_\beta$). The constant 6147(7) s is obtained from experimental data on the $0^+ \rightarrow 0^+$ superallowed Fermi decay [46] and the ratio of the vector to axial vector constants has its free neutron value of -1.262(4) [47, 48].

The $\beta$-decay reduced transition probabilities are related to their matrix elements by [49]

$$B(F) = \frac{1}{2J+1} | < J||M_F||J > |^2 \tag{2.22}$$

$$B(GT) = \frac{1}{J_i+1} | < J_f||M_G||J_i > |^2 \tag{2.23}$$

where $J$ is the total angular momentum of the state and the subindex accounts for initial ($i$) or final ($f$) state. For very neutron rich nuclei, the $\beta$-decay transitions are

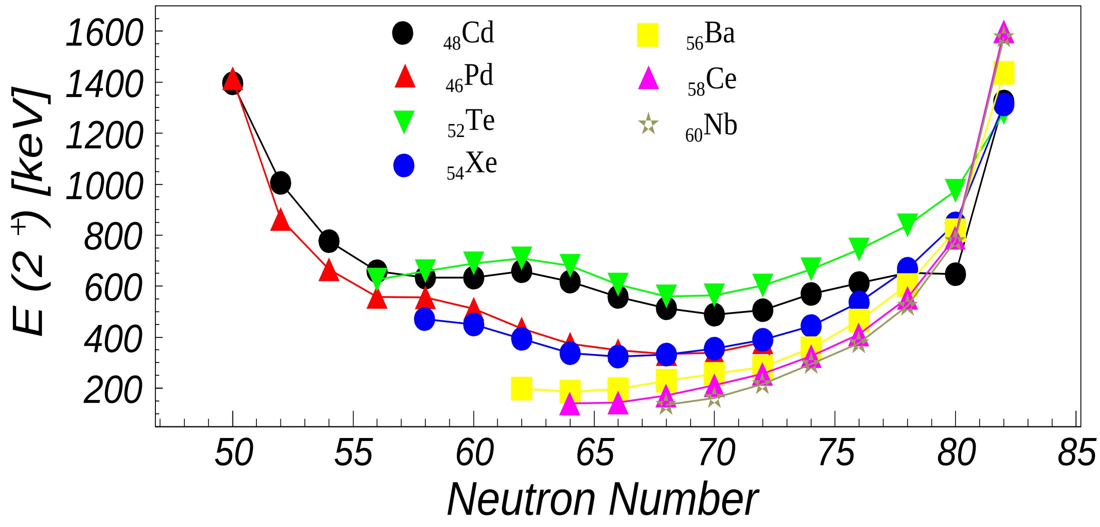


Figure 2.6: *E(2$^+$) excitation energy systematics for nuclei with* $Z = 46$ *to* $Z = 60$*. The anomalous behavior of the* 2$^+$ *energy in the Cd chain when approaching* $N = 82$ *is observed. See text for details.*

dominated by the Gamow-Teller type. Experimentally the reduced transition probability is extracted from

$$B^{exp}(GT) = \sum_i B_i(GT) = \sum_i \frac{3860}{f_i t_i} \tag{2.24}$$

where the subindex $i$ denotes all individually observed transitions. To evaluate Equation 2.24 requires experimental data for the calculation of the $f_i$ function and the partial half-life $t_i$. The statistical $\beta$-decay function depends on the transition energy $W$, which is the difference between the decay energy $Q_\beta$ and the excitation energy of the state in the daughter nucleus populated directly in the $\beta$-decay. In order to evaluate it a measurement of $Q_\beta$ is needed. The partial half-life follows the expression

$$t_i = \frac{T_{1/2}}{(I_\beta)_i} \tag{2.25}$$

For neutron rich nuclei, the dominant transition is the allowed Gamow-Teller transition $\nu g_{7/2} \longrightarrow \pi g_{9/2}$ in systems below $Z = 50$. For nuclei close to the doubly-magic $^{132}$Sn above the proton shell closure, the first forbidden transitions start to play a role due to the completely filled $\pi g_{9/2}$ orbital. In this case the dominant decays are $\nu f_{7/2} \longrightarrow \pi g_{7/2}$ and $\nu g_{7/2} \longrightarrow \pi d_{5/2}$ [32]. Most of the information of neighbouring nuclei close to $^{132}$Sn is provided from $\beta$-decay experiments. In general these experiments were performed in Isotope Separation On-Line (ISOL) type facilities which require a long extraction time from the ion sources before any possible nuclear structure investigation of a specific isotope can be performed. A more detailed description of the ISOL method will be given in Section 3.7. Nowadays with the development of the new radioactive beam facilities alternative production methods for these neutron rich nuclei can be considered.

Concentrating on the Cd isotopic chain, a systematic study of the $2^+$ excitation energies was carried out by Kautzsch et al. [41] in ISOL type $\beta$-decay experiments. In their work, they observed a similar trend of the E($2^+$) for the Cd and Te isotopes from $N = 58$ up to $N = 76$ as shown in Figure 2.6. At lower neutron number, the excitation energy increases when approaching the $Z = 50$ magic number as expected. A similar trend should be visible when the shell closure is at $N = 82$, and indeed it is observed for the Te, Xe, Ba, Ce and Nb chains, but not for the Cd isotopes. The $2^+$ excitation energy in $^{128}$Cd lies 4 keV lower than in $^{126}$Cd. In the same work, a $2^+$ state in $^{130}$Cd at 957 keV has been tentatively assigned. Those results have been interpreted as evidence of a $N = 82$ shell quenching at $Z = 48$ as mentioned in the previous section. In addition, since the possible reduction of the shell gap would result in an increase of collectivity, the authors use the relation between the deformation parameter ($\beta_2$) and the reduced transition probability reported in [50] to estimate a deformation of $\beta_2 \simeq 0.12$. The results presented in this work are interpreted based on LSSM calculations and give an alternative explanation for the anomalous behavior of the $2^+$ excitation energies in the Cd isotopes when approaching the $N = 82$ shell closure.

Additional interesting information from the $\beta$-decay experiments is the weak delayed-neutron branch of $P_n = 3.5(1)$ % observed in the $\beta$-decay of $^{131}$Cd [51]. The experimental results could only be reproduced when a modified Nilsson potential with a 25 % reduction of the $l^2$ term was introduced in their calculations. This reduction lead to a lowering of the pairing energy for neutrons and consequently a reduction of the $N = 82$ shell gap of 1 MeV in $^{131}$Cd.

It is worth to mention that all the available information on single particle/hole states near $^{132}$Sn is a result of $\beta$-decay experiments [38].

### 2.4.3 r-Process

Nuclei heavier than Fe are produced by slow neutron capture ($s$-process) and rapid neutron capture ($r$-process), both processes contributing to the observed solar abundances. Since the $s$-process governs the production of those nuclei which lie close to the valley of stability, its contributions to the solar abundances are relatively well understood. The $r$-process contribution can therefore be deduced from the difference between the $s$-process yields and the observed abundances [52]. The $r$-process in contrast to the $s$-process is responsible to the production of very neutron rich nuclei. The classical $r$-process mechanism is based on a rapid neutron capture by the nuclei, so that the neutron capture rates are much faster than those of $\beta$-decay. Therefore it requires an environment where high neutron densities are available. So far it is not clear which are the astrophysical sites for the $r$-process to take place, although there are two main models which account for such conditions, the neutrino-driven wind model [53] and the neutron star merger model [54].

In the $r$-process the nuclei capture neutrons more rapidly than they undergo $\beta$-decay, thus moving towards the neutron drip line. When increasing the number of neutrons, the neutron separation energy reduces. The r-process occurs until the equilibrium between neutron capture and photodissociations is achieved ((n,$\gamma$)$\rightleftarrows(\gamma, n)$). At this point, for each isotopic chain there will be one nucleus with maximum abundance.

These are the so called "waiting point" nuclei, because the nuclei wait to $\beta$-decay and can not pick up additional neutrons. The waiting-point nuclei with neutron magic numbers have considerably long $\beta$-decay half-lifes and therefore in general larger abundances. As a common feature, the neutron separation energy for the waiting-point nuclei [32, 55] for a given neutron density and temperature is the same.

The exact position of the waiting-point nuclei on the $r$-process path depends on the neutron density, the stellar temperature and the neutron separation [52] or neutron binding energy. Therefore a detailed description of the $r$-process requires knowledge of the nuclear structure of the neutron rich nuclei. Unfortunately, this information is limited due to the experimental difficulties in the production of such nuclei (low fragmentation or fission reaction cross sections and they are not populated in fusion-evaporation reactions). The neutron binding energy is extracted from mass measurements, although there is little information about masses on the neutron rich side of the nuclidic chart. Therefore most $r$-process models rely on calculated masses which have large uncertainties. The $\beta$-decay half-life is another important parameter, mainly because the nuclear abundances depend on it, particularly for nuclei with neutron magic numbers, and therefore the location of the waiting-point nuclei. Additional questions regarding the $\beta$-decay are

- Level densities in the daughter nucleus
- $\beta$-strength functions averaged over the final states in the daughter nucleus
- $\beta$-strength functions taking into account the effects of nuclear structure

All these issues require experimental information which started to be available in the 80's thanks to the increased intensities provided by the radioactive beam facilities.

Focusing on the $^{132}$Sn region, the trough in the solar abundance distribution around $A \simeq 115$ is filled when mass models which include shell quenching at $N = 82$ are used in the $r$-process abundance calculations [55, 56] (Figure 2.7).

Additionally the experimentally extracted large $Q_\beta$ value for the $^{130}$Cd decay is only reproduced by those mass models which include $N = 82$ shell quenching [40]. Some other $r$-process calculations of the solar abundances are able to fill the trough at $A \simeq 175$ even with mass models which consider a strong shell gap, although in this calculation the trough at $A \simeq 115$ is not filled [57]. Additional information concerning the nuclear structure of nuclei close to $^{132}$Sn will provide a better understanding of the $r$-process and therefore the formation of the elements.

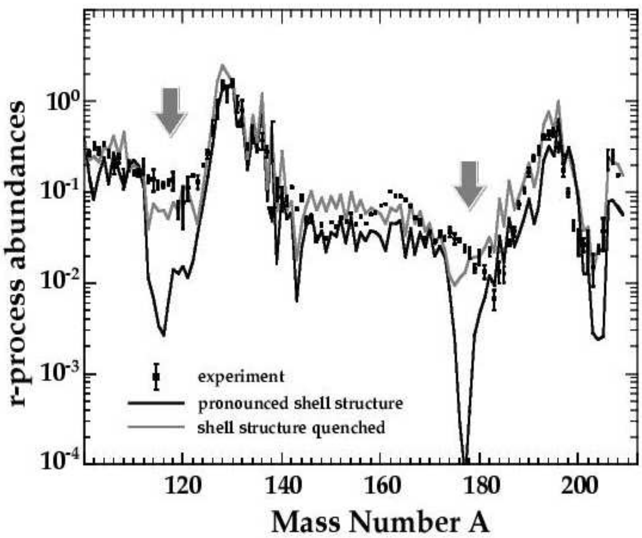


Figure 2.7: *Observed solar abundances distribution compared to two r-process calculations assuming either a pronounced or a quenched N=82 shell gap. A better reproduction of the abundances is obtained when the shell gap is assumed to be quenched [56].*

# Chapter 3

# Analysis of the delayed $\gamma$-ray spectra and Results

The ions continue their flight-path through the S4 area and are stopped in a passive "stopper" in the last focal plane of the FRS. The $\gamma$-radiation emitted by the nuclei was measured with the Ge array placed in close geometry surrounding the "stopper". By requiring coincidence between the identified fragments and the detected $\gamma$ rays over a range from 0 to 24 $\mu$s after the implantation, the $\gamma$ rays can be unambiguously assigned to the isomeric decay of one particular isotope. The time was measured with different precision in two independent electronic circuits, an analogue one with a time resolution of 0.7529 ns/ch and a digital branch with 25ns/ch as explained in Section 3.3.1. The $\gamma$ energy was measured in a range from 30 keV to 6 MeV.

The goal of this work is to study the isomeric decay of very neutron rich nuclei. In particular, the systems with large $N/Z$ ratio close to the doubly-magic $^{132}$Sn nucleus are relevant both due to their implications in the r-process of the nucleosyntesis as well as their importance as test cases for the nuclear models.

Isomeric states in $^{128}$Cd, $^{130}$Cd and $^{131}$In were produced both in the fragmentation of a $^{136}$Xe primary beam at 750 MeV/u and an average intensity of $\sim 7.4\times10^{8}$ ions/s and the fission of a $^{238}$U primary beam at 650 MeV/u and an average intensity of $\sim 2.7\times10^{8}$ ions/s delivered by the accelerator complex of GSI, where the FRS was set to optimize the transmission of $^{130}$Cd ions. The isomeric states in $^{126}$Cd were populated in the fragmentation reaction with the $^{130}$Cd ions describing the central trajectory of the FRS, and afterward for a short period of time the magnets were set to optimize the transmission of the $^{126}$Cd ions. The fragmentation reaction cross sections for all the measured isotopes were previously known and amount to $1.386\times10^{-7}$ barns, $2.57\times10^{-6}$ barns, $2.061\times10^{-5}$ barns and $6.755\times10^{-6}$ barns for $^{130}$Cd, $^{128}$Cd, $^{126}$Cd and $^{131}$In, respectively [93]. Recently, based on a similar study, however without any time correlation, Hoteling et al. [94] have suggested level schemes for $^{126}$Cd and $^{128}$Cd. This work includes half-life and $\gamma\gamma$ coincidence analysis performed for the first time in these very neutron rich nuclei. Both types of analysis are essential to unambiguously construct the level scheme associated to the states populated in the isomeric decay. In addition, in this work the statistics is much higher than in [94], allowing the observation of transitions with the intensity of about 1 % of the main cascade. The $\gamma$ spectra presented in this chapter are obtained from the data based on fragmentation and

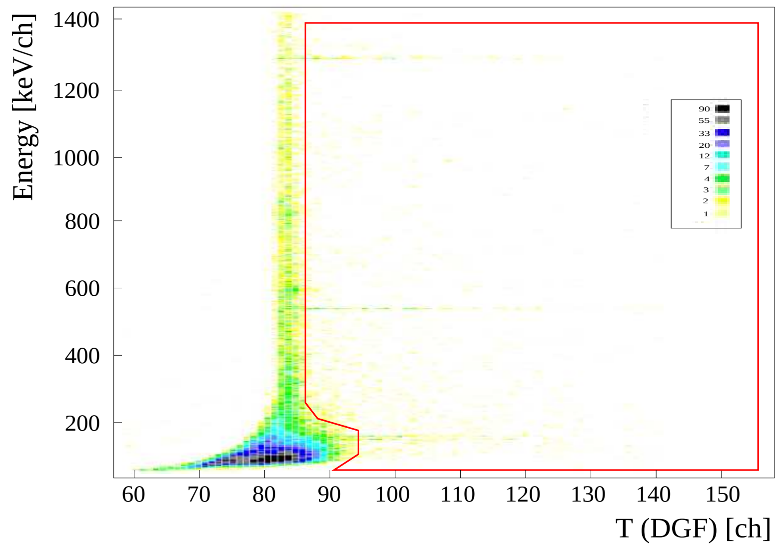


Figure 3.1: *Energy versus time matrix gated by the $^{130}$Cd isotopes. The $\gamma$ rays associated to the isomeric decay are visible. The gate applied to remove the contribution of the "prompt-flash" in the energy spectra is shown by the red curve.*

fission reactions.

## 3.1 The nucleus $^{130}$Cd

The only information available about $^{130}$Cd is provided by $\beta$-decay experiments [40, 41]. The large $N/Z$ ratio of this nucleus makes its production and the study of its nuclear structure properties a challenge. Only one single $\gamma$-ray has been tentatively associated, prior to this work, to the decay pattern of $^{130}$Cd [41]. The improvement of the beam intensities delivered by the GSI accelerator facility allowed to produce this nucleus with high enough statistics to perform $\gamma$ spectroscopy studies. Two different experiment were dedicated to the production of $^{130}$Cd. The FRS was set to optimize the transmission of $^{130}$Cd in the fragmentation and fission reactions. In total 6300 $^{130}$Cd nuclei were produced.

The delayed $\gamma$ singles spectrum in $^{130}$Cd was produced by projecting the walk corrected energy versus time matrix on the energy axis applying a gate to remove the contribution of the prompt flash as it is shown in Figure 3.1 as red curve. All the transitions belonging to the decay of an isomeric state have a time distribution corresponding to the lifetime of the isomeric level and are visible in the matrix. The resulting spectrum is shown in Figure 3.2a. Four different transitions with energies of 128 keV, 138 keV, 539 keV, and 1325 keV are visible. Although the statistics is limited, the high efficiency of the Ge array allowed to perform a $\gamma\gamma$ coincidence analysis. The resulting spectra gated on each of the lines in the $\gamma\gamma$ matrix are shown in Figure 3.2b, c, and d. All these transitions are in mutual coincidence forming a single cascade from the isomeric state to the ground state.

The analysis of isomeric half-lives was based on an exponential decay fit to the time spectrum. The time distributions associated to the $\gamma$ rays were produced by

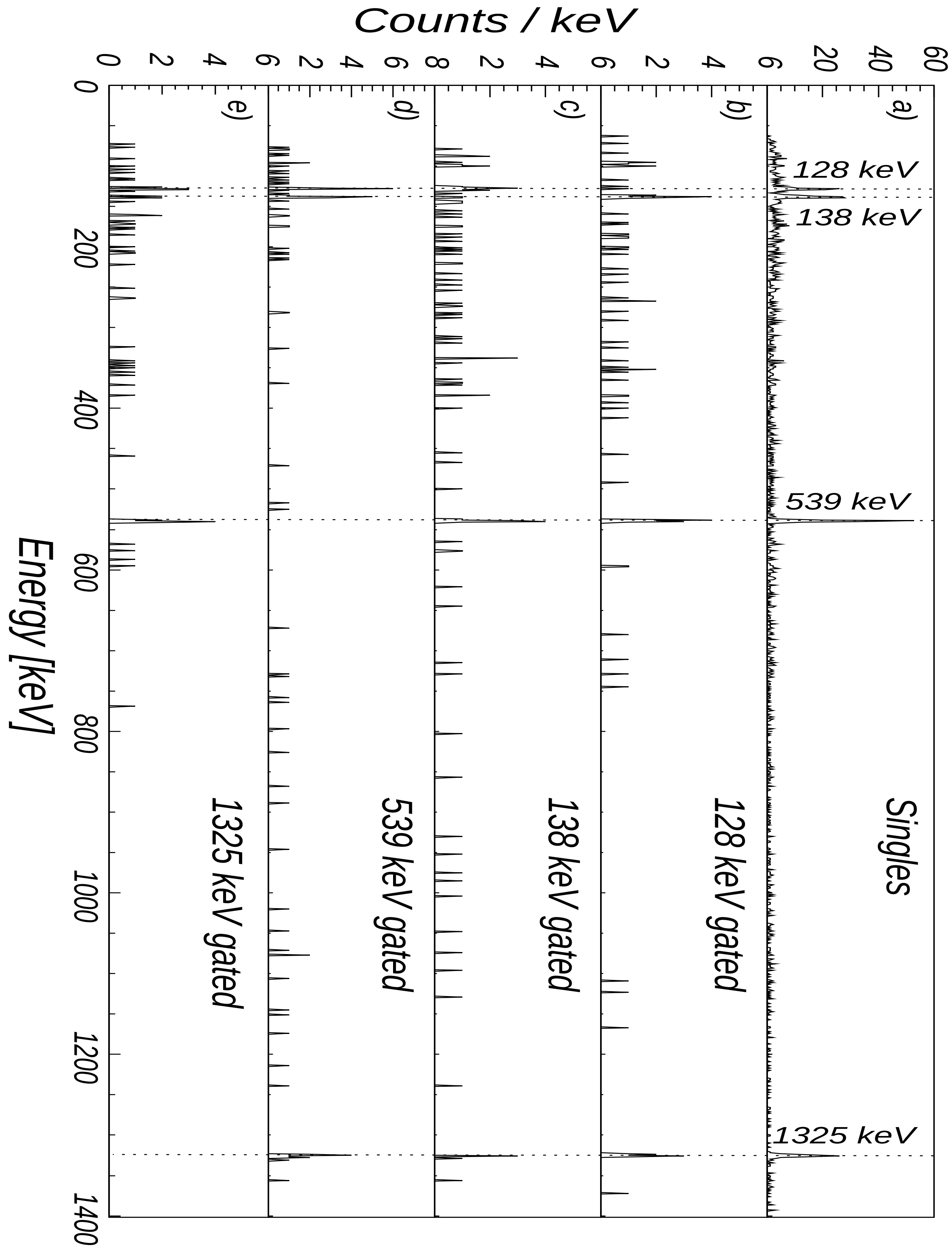


Figure 3.2: *a): Singles $\gamma$ energy spectrum in coincidence with $^{130}$Cd. b), c), d) and e): Coincidence $\gamma$ spectra gated by 128 keV, 138 keV, 538 keV and 1325 keV transitions, respectively.*

Table 3.1: *$\gamma$ ray energies, half-lifers, relative intensities, and experimental conversion coefficients compared to the theoretical values in $^{130}$Cd.*

| $E_\gamma$ [keV] | $T_{1/2}$[ns] | $I_\gamma$[%] | $\alpha_{exp}$ | $\alpha(E1)_{th}$ | $\alpha(M1)_{th}$ | $\alpha(E2)_{th}$ |
|---|---|---|---|---|---|---|
| 128.2(3) | 235(46) | 59(10) | 0.69(27) | 0.08 | 0.23 | 0.62 |
| 138.1(2) | 208(35) | 72(9) | 0.38(18) | 0.07 | 0.19 | 0.48 |
| 539.3(2) | 272(48) | 101(13) | | | | |
| 1325.5(3) | 248(50) | 99(14) | | | | |
| All | 235(53) | | | | | |

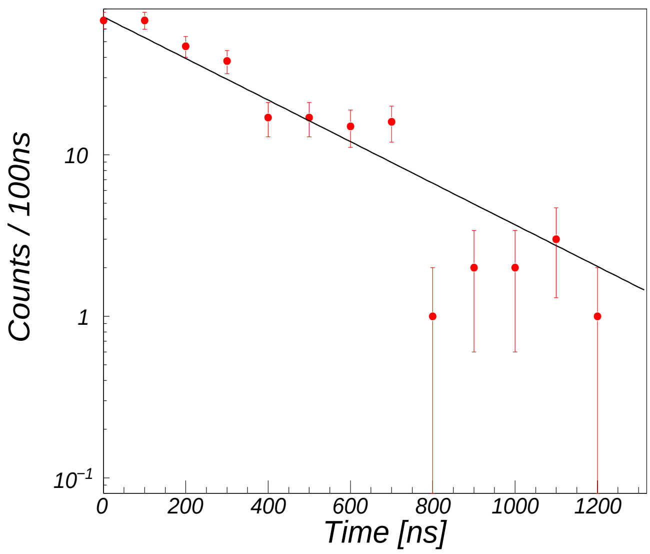


Figure 3.3: *Sum of the time distributions of the four observed $\gamma$ rays in coincidence with $^{130}$Cd with respect to the ion implantation. The result of the individual fit is shown in Table 3.1*

background subtracted gating on each $\gamma$ line in the energy versus time matrix. The least squares fit of the time distribution of each of these $\gamma$ rays with respect to the ion implantation separately with a single exponential decay function described by

$$\frac{dN}{dt} = -\frac{ln2}{T_{1/2}} e^{ln2 \cdot t/T_{1/2}}, \tag{3.1}$$

where $N$ is the level population at time $t$ and $T_{1/2}$ is the half-life of the isomeric state yield the isomeric half-life. The resulting half-life values agree within their statistical errors (Table 3.1). The sum of the time distribution of the four $\gamma$ lines is shown in Figure 3.3.

The relative intensities of the transitions were extracted from the areas of the $\gamma$ lines and the reconstruction of the events lost by the effect of the gate applied to remove the contribution of the prompt-flash in the energy spectrum. The reconstruction was made by means of the measured isomeric half-life. The fraction of nuclei in % remaining for decay was estimated from the following equation

$$\frac{N}{N_0} = e^{ln2\cdot(t_1-t_0)/T_{1/2}}, \tag{3.2}$$

where $N_0$ is the initial population of the state, $N$ is the state population at time $t_1$ defined by the time position of the gate and $t_0$ is the implantation time. The reconstructed $\gamma$ ray intensity is expressed as follows

$$I_r = \frac{I}{e^{ln2\cdot(t_1-t_0)/T_{1/2}}}. \tag{3.3}$$

The gate applied to remove the contribution of the prompt flash was set to 250 ns from the ion implantation for the 128 keV and 138 keV and 75 ns for the 539 keV and 1325 keV transitions. Therefore the fitted $\gamma$ intensities in the singles $\gamma$ spectrum amount to 48(3) % of the total intensity for the 128 keV and 138 keV lines and 86(7) % for the 539 keV and 1325 keV transitions. The relative intensities of the $\gamma$ transitions normalized to the weighted mean intensity of the 539 keV and 1325 keV lines are shown in Table 3.1. Taking into account that the measured four $\gamma$ rays form a single cascade, the missing intensity for the low energy transitions is caused by internal conversion. Based on the comparison between the experimental conversion coefficients extracted from this experiment and the theoretical values assuming different multipolarities, $E2$ character is the most likely assignment for the 128 keV and 138 keV transitions (Table 3.1).

In $^{130}$Cd an $8^+$ isomeric state formed by the maximally aligned two proton holes in the $g_{9/2}$ orbital is expected to exist in analogy to the $8^+$ isomer observed in the valence mirror nucleus $^{98}$Cd [27]. The transition energies in the E2 cascade from the isomeric state to the ground state in $^{98}$Cd are 147 keV, 198 keV, 688 keV and 1395 keV. Therefore the 539 keV and 1325 keV transitions are assigned to form the $4^+ \rightarrow 2^+ \rightarrow 0^+$ cascade. The new E($2^+$) value in $^{130}$Cd is in disagreement with the previously tentatively assigned [41] value of 957 keV for the $2^+$ excitation energy in $^{130}$Cd. Within the experimental sensitivity it was not possible to determine the ordering of the 128 keV and 138 keV transitions. These two $\gamma$ rays form the $8^+ \rightarrow 6^+ \rightarrow 4^+$ sequence. The comparison between the $^{98}$Cd and $^{130}$Cd level schemes is shown in Figure 3.4. The low statistics did not allow to extract the nanosecond half-life expected for the $6^+$ isomeric state when assuming a pure $\pi(g_{9/2})^{-2}$ configuration for the $2^+$ to $8^+$ levels. The experimental B(E2:$8^+ \rightarrow 6^+$) values assuming either the 128 keV or the 138 keV $\gamma$ ray to be the $8^+ \rightarrow 6^+$ transition are 1.11(25) W.u. and 0.83(18) W.u., respectively. The reduced transition probability in $^{130}$Cd compares well with the experimental B(E2) strength of 1.3(4) W.u. in $^{98}$Cd. Based on the experimental results and the comparison to $^{98}$Cd, $I^\pi = 8^+$ is assigned to the isomeric state decaying by $E2$ transitions to the ground state. The interpretation of these results in the framework of the LSSM will be discussed in the next chapter. The results shown in this section are published in Reference [95]

In the following subsections, the study of the effect of the particle gatting in the $\gamma$ spectrum will be shown. This type of analyisis was performed to obtain the "best" $\gamma$ spectrum to be able to shed light of the nuclear properties of the nucleus of interest, with best meaning the higher statistics and lower background. The particle conditions

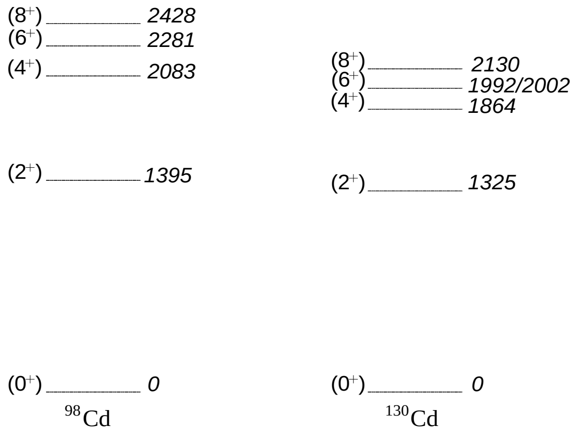


Figure 3.4: *Isomeric decay level schemes for $^{98}$Cd (left) and $^{130}$Cd (right). The spin and parity assignment for the excited states in $^{130}$Cd has been done based on the comparison to the $^{98}$Cd level scheme.*

specified in the corresponding subsection to be kept were applied to $^{126}$Cd, $^{128}$Cd and $^{131}$In particle identification and are used in the $^{130}$Cd identification presented in this section, as well.

### 3.1.1 Effect of the particle selection on the $\gamma$-ray spectrum

For a correct correlation between the ion implantation and its isomeric decay a clean and unambiguous isotope selection is crucial. However some of the particle conditions applied in the analysis might lead to a reduction of the number of the observed $\gamma$-rays due to the low efficiency of some of the particle detectors. Detailed study of the $\gamma$ intensities obtained using different particle conditions was performed. This allowed to select those conditions which providing a clean identification do not contribute to the reduction of the number of counts in the observed $\gamma$ peaks. In the following sections the effect of different particle conditions on the $\gamma$ energy spectrum belonging to the isomeric decay of $^{130}$Cd will be shown.

#### 3.1.1.1 Contamination in the $\gamma$ energy spectrum caused by reactions in the degrader at S4

Table 3.2 summarizes the effect of the reactions in the last degrader on the $\gamma$ energy spectrum. The gate applied is exemplified in Figure **??**. The number of counts in the $\gamma$ transitions were almost the same with and without the gate applied, although an increase of the background in the spectrum was observed when the condition was removed. Defining the quantity peak-to-background (peak-to-bck) as

$$peak - to - bck = \frac{I_\gamma^{background-subtracted}}{I_\gamma}; \tag{3.4}$$

the background can be estimated, where $I_\gamma^{background-subtracted}$ is the intensity of the $\gamma$ transition when a constant background is subtracted, and $I_\gamma$ is the total intensity of the $\gamma$ peak. Based on the numbers presented in Table 3.2, this condition was kept in the data analysis providing a cleaner particle identification and in addition reducing the background observed in the $\gamma$ energy spectrum.

Table 3.2: *Intensity of the $\gamma$ transitions and peak-to-bck observed in the $^{130}$Cd isomeric decay gated and not gated by the ion energy loss in the SCI3 versus Z matrix. See text for details.*

| Energy [keV] | Gated | Not gated | Peak-to-bck [gated] | Peak-to-bck [Not gated] |
|---|---|---|---|---|
| 128 | 63(9) | 65(9) | 82(17)% | 68(17)% |
| 138 | 82(9) | 81(10) | 89(16)% | 66(17)% |
| 539 | 122(11) | 122(12) | 92(10)% | 90(11)% |
| 1325 | 81(9) | 85(10) | 99(12)% | 84(13)% |

#### 3.1.1.2 Ion tracking detectors: The effect of the conditions on the MPWC detectors

The MWPCs were used for the ion tracking and for the correction for the dependence of the energy loss on the ion trajectory measured in the MUSIC detectors. These detectors provide ion position information both in $X$ and $Y$ coordinates. The $X$ position measurement is used in the calculation of the $A/Z$ ratio.

The effect of particle gating in these detectors on the energy spectrum was investigated by comparing the $\gamma$ ray intensities under different gating conditions. The results are shown in Table 3.3. The number of counts in the $\gamma$ peaks when no gate was applied and when a selection in the $X$ coordinate in the MWPC was required is the same (second and third column of the Table 3.3). This is expected because the $X$ position information is required for MUSIC calibration purposes. Any spectrum which is extracted applying a $Z$ selection in the analysis is therefore at the same time already conditioned by the efficiency of the MWPC in the $X$ axis.

A different result is obtained when the gating is done on the $Y$ axis. The number of counts is reduced when the gate was set on both, the $X$ and the $Y$ coordinates of MWPC2 or the $X$ and the $Y$ coordinates in both MWPC. This effect is caused by the low efficiency of the detectors. It is clear that while an implicit selection in $X$ is performed through the calibration coefficients, any explicit gate on $Y$ coordinate must be avoided.

#### 3.1.1.3 Reactions in the MUSIC detectors

When the ions pass through the first ionization chamber at $S4$, 4 % of them undergo nuclear reactions. These nuclei will contribute to an increase of the background in the $\gamma$ energy spectrum. Although the fraction of these ions relative to the total intensity of the secondary beam is small, a gate applied as shown in Figure **??** will eliminate these contaminants and therefore decrease the background. The intensities and peak-to-bck ratios in both cases, with and without gate applied, are shown in Table 3.4. This condition was kept in the analysis.

Table 3.3: *Intensity of the $\gamma$ transitions observed in the $^{130}Cd$ isomeric decay under different particle conditions applied to the ion position measured in the MWPC detectors. See text for details.*

| Energy [keV] | Not gated | X gated | XY (MWPC2) | XY(both) |
|---|---|---|---|---|
| 128 | 63(9) | 65(9) | 51(8) | 48(8) |
| 138 | 82(9) | 74(9) | 60(9) | 54(8) |
| 539 | 122(11) | 122(11) | 95(10) | 95(10) |
| 1325 | 81(9) | 81(9) | 66(8) | 64(8) |

Table 3.4: *Intensity of the $\gamma$ transitions and peak-to-bck ratios observed in the $^{130}Cd$ isomeric decay gated and not gated by the $Z_2$ versus $Z_1$ matrix. See text for details.*

| Energy [keV] | Gated | No gated | Peak-to-bck [gated] | Peak-to-bck [Not gated] |
|---|---|---|---|---|
| 128 | 63(9) | 65(9) | 82(17)% | 75(17)% |
| 138 | 82(9) | 74(10) | 89(15)% | 74(16)% |
| 539 | 122(11) | 120(11) | 92(10)% | 89(10)% |
| 1325 | 81(9) | 82(9) | 99(12)% | 90(13)% |

## 3.2 The nucleus $^{128}$Cd

The $^{128}$Cd nucleus is easier to access experimentally than $^{130}$Cd therefore more information is available provided both from $\beta$-decay [41] as well as delayed $\gamma$ experiments [94]. Nevertheless, no unambiguous level scheme has been constructed up to now.

The $^{128}$Cd nucleus was produced in the experiments when the FRS was set to optimized the transmission of $^{130}$Cd in fragmentation and fission reactions. In total $3.29\times10^5$ ions were identified.

The delayed $\gamma$ singles spectrum following the implantation of $^{128}$Cd was obtained from the energy versus time matrix (Figure 3.5) applying a gate to remove the contribution of the prompt flash as in the $^{130}$Cd case. The resulting spectrum is shown in Figure 3.6a. All previously known transitions [41, 94] are visible and in addition two strong lines at 69 keV and 1224 keV energy are observed for the first time.

The level scheme of the isomeric decay was built based on the $\gamma\gamma$ coincidence analysis and the relative intensity balance. The relative intensities of the $\gamma$ transitions normalized to 646 keV line are observed to depend on the time window set in the energy versus time matrix with respect to the $^{128}$Cd implantation (Figure 3.5), this fact indicates the existence of at least two isomeric states with different lifetimes in $^{128}$Cd. The extracted $I_\gamma$ intensities for two different time windows, one 50 ns from the prompt up to 23.3 $\mu$s, and a second from 50 ns from the prompt up to 850 ns, are summarized in Table 3.5.

Two types of $\gamma\gamma$ matrices were constructed, the first type with open time window

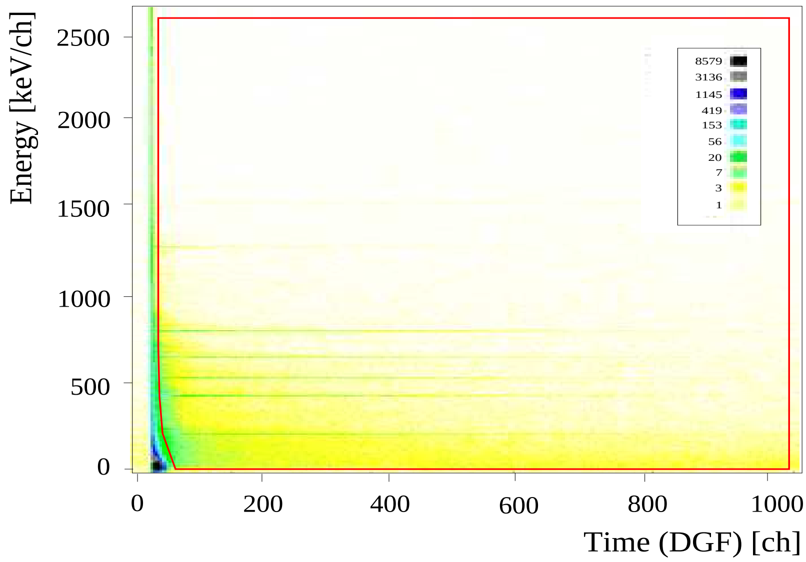


Figure 3.5: *Energy versus time matrix gated by the* $^{128}$*Cd isotopes. The* $\gamma$*-rays associated to the isomeric decay are visible. The gate applied to remove the contribution of the "prompt-flash" in the energy spectra is shown by the red curve.*

and the second with the condition that the maximum time difference between the two coincident $\gamma$'s is smaller than 125 ns (Figure 3.9).

In the $\gamma\gamma$ coincidence analysis with open time condition ($\Delta$t = 23.35 $\mu$s) it was found that all strong $\gamma$ rays seen in Figure 3.6a belong to the main cascade with the exception of the 1224 keV transition which is not observed in coincidence with the 440 keV (Figure 3.7b) and 785 keV lines (Figure 3.6b). The coincidence spectrum with gate on the 1224 keV line is shown in Figure 3.8c. The 785 keV and 646 keV transitions were assigned in [41] to form the $4^+ \rightarrow 2^+ \rightarrow 0^+$ cascade. The ordering of these two transitions is now unambiguously confirmed by the new $\gamma\gamma$ coincidence information. The 440 keV was placed feeding the $4^+$ state and decaying from the 1871 keV level.

The $\gamma$ transitions emitted from states populated in the same isomeric decay are expected to have the same relative intensities in the coincidence spectrum. The $\gamma\gamma$ coincidence analysis requiring the time difference between the two coincident $\gamma$-rays is smaller than 125 ns shows that not all the observed transitions have the same intensity in the coincidence spectra. The spectrum obtained from this matrix by gating on the 238 keV transition shows a strong reduction in the intensity of the 646 keV, 785 keV, 440 keV, and 1224 keV $\gamma$ rays when compared to the 538 keV $\gamma$-peak as it is visible in Figure 3.6c. Analogue coincidence relations were found gating on the 538 keV (Figure 3.10) and 69 keV peaks with respect to the 238 keV intensity compared to the other lines. Additionally it was found that the intensity of the 238 keV, 538 keV, and 69 keV transitions was much smaller than the intensity of the 646 keV line when gating on the 785 keV, 440 keV, or 1224 keV $\gamma$ peaks. The resulting spectra when the gate was set on the 785 keV and 440 keV transitions are shown in Figure 3.7a and b, respectively. This observation confirms the existence of at least two isomeric states in $^{128}$Cd.

The time distributions of the 646 keV, 785 keV, 440 keV and 1224 keV transitions

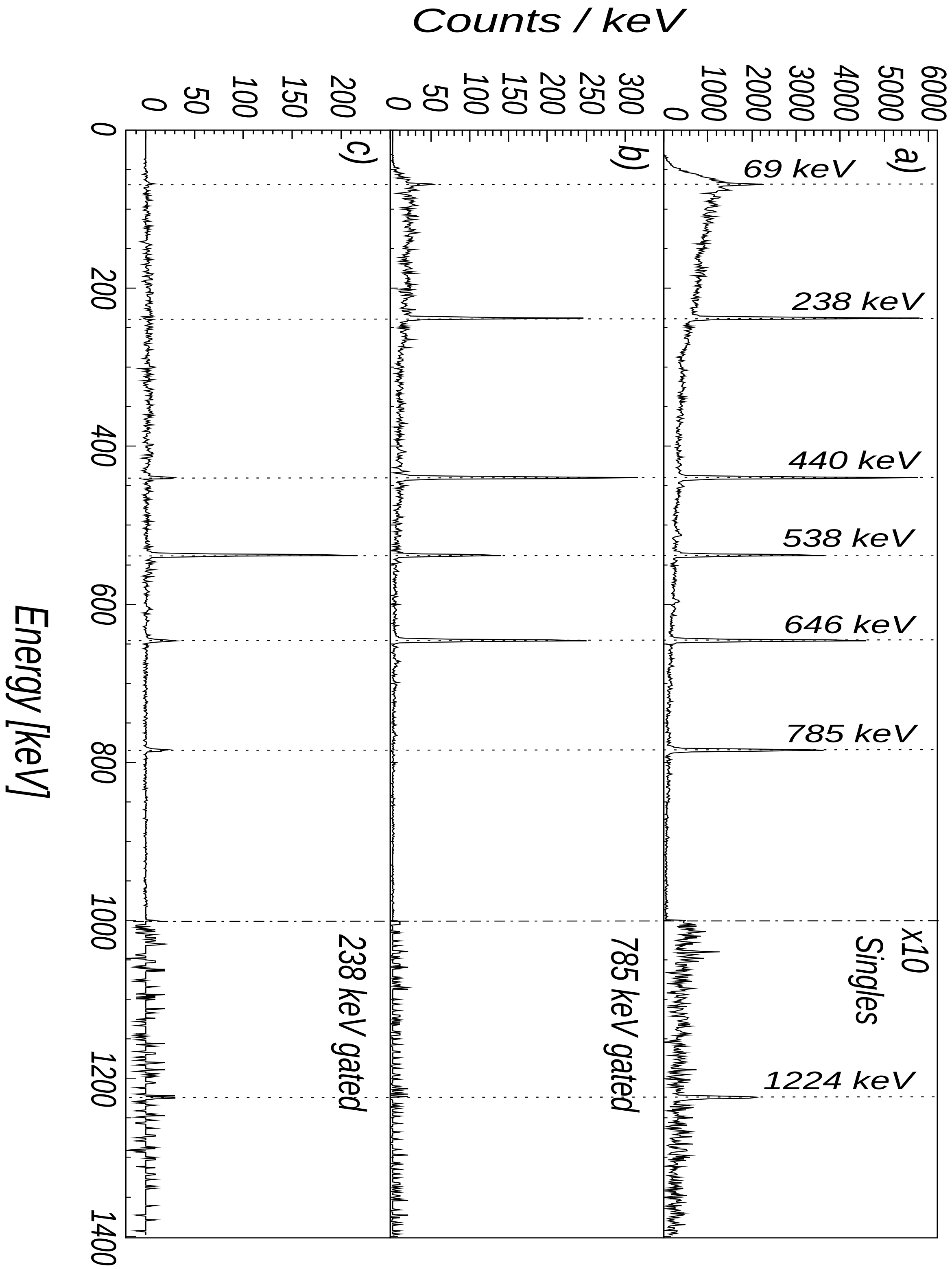


Figure 3.6: *a) $\gamma$ ray energy spectrum in coincidence with $^{128}Cd$ ions. b) Spectrum obtained from the $\gamma\gamma$ matrix gated by the 785 keV transition with open time condition ($\Delta t = 23.25\ \mu s$). c) Spectrum obtained from the prompt $\gamma\gamma$ matrix gated by the 238 keV transition requiring the maximum time difference between the two coincident $\gamma$-rays is smaller than 125 ns. See text for details.*

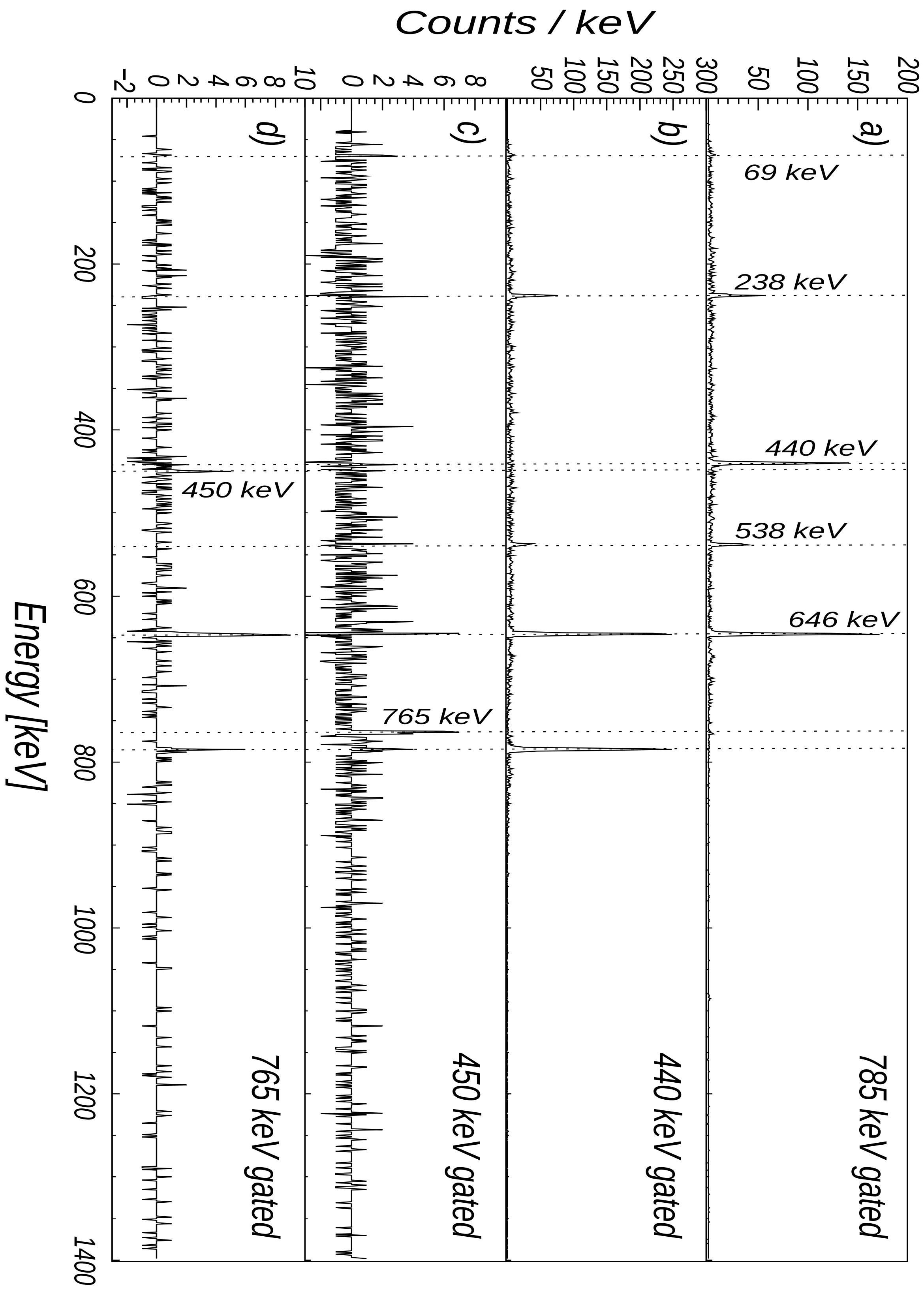


Figure 3.7: $^{128}Cd$ $\gamma$ *energy spectra extracted from the prompt* $\gamma\gamma$ *matrix gated on the 785 keV (a), 440 keV (b), 450 keV (c), and 765 keV (d) transitions requiring the time difference between two coincident* $\gamma$*'s is smaller than 125 ns.*

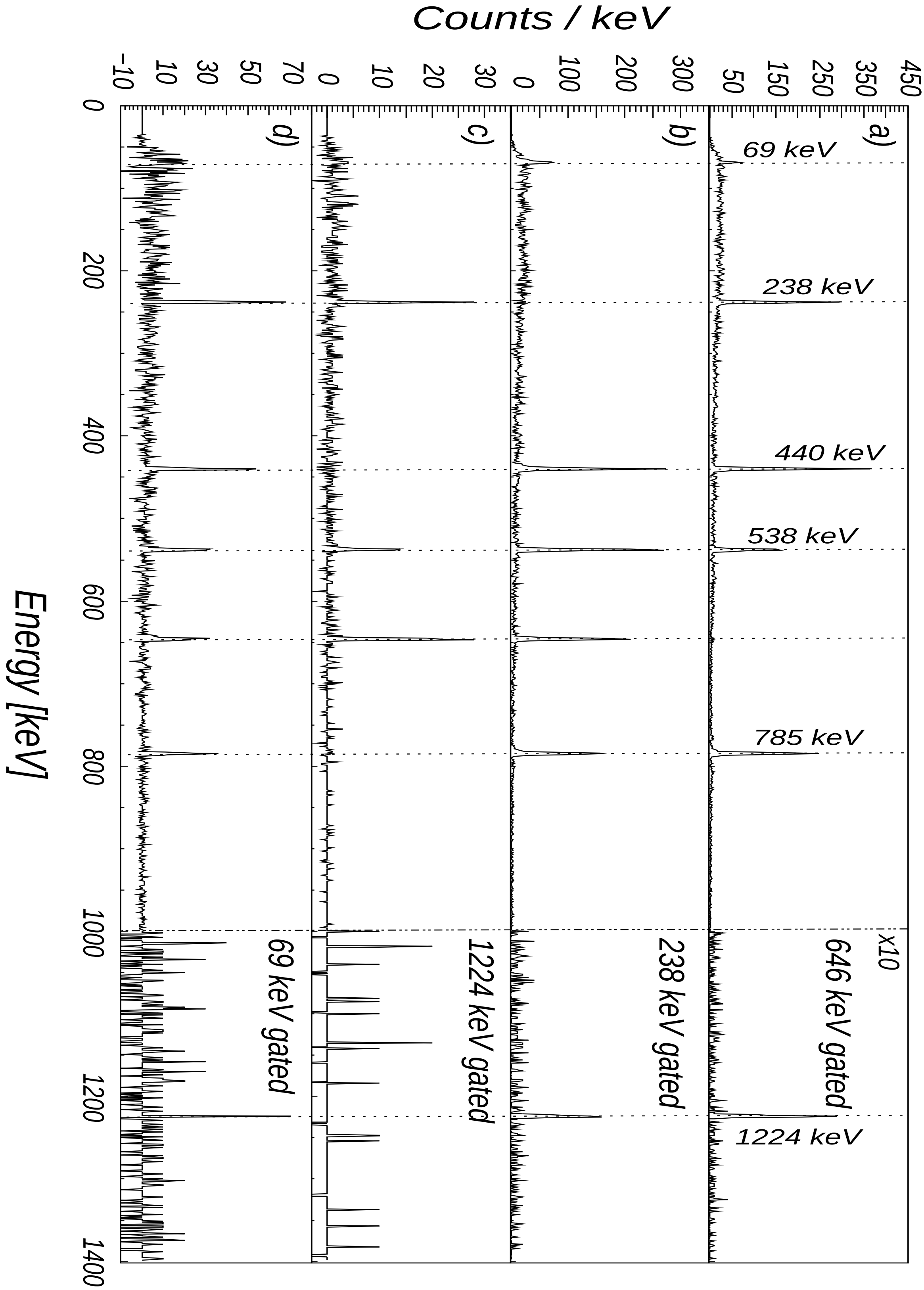


Figure 3.8: $^{128}Cd$ $\gamma$ *energy spectra extracted from the* $\gamma\gamma$ *matrix gated by 646 keV (a), 237 keV (b), 1224 keV (c), and 69 keV (d) lines with open time window.*

Table 3.5: *Relative $\gamma$ ray intensities normalized to the 646 keV transition for two different time windows, $\Delta t$ = 23.25 $\mu s$ (middle column) and $\Delta t$ = 800 ns (right column), set in the energy versus time matrix in coincidence with $^{128}Cd$ for the summed, fragmentation (Frag.) and fission data.*

| | $\Delta$t = 23.25 $\mu$s | | | $\Delta$t = 800 ns | | |
|---|---|---|---|---|---|---|
| $E_\gamma$ [keV] | Summed | Frag. | Fission | Summed | Frag. | Fission |
| 237.9(5) | 39(2) | 40(2) | 34(2) | 8(1) | 8(1) | 8(1) |
| 440.0(3) | 84(4) | 83(4) | 86(5) | 84(4) | 84(4) | 83(3) |
| 450.4(3) | 1.8(3) | 2.0(3) | | | | |
| 537.6(2) | 47(3) | 48(3) | 40(3) | 14(1) | 15(1) | 4(1) |
| 645.8(2) | 100(5) | 100(5) | 100(6) | 100(5) | 100(5) | 100(7) |
| 765.0(3) | 1.2(2) | 1.2(3) | | | | |
| 784.6(1) | 90(5) | 90(5) | 85(5) | 98(5) | 98(5) | 99(7) |
| 1224.0(6) | 11(1) | 11(1) | 10(2) | 11(1) | 12(1) | 9(2) |

below the 1871 keV level show indeed two decay components (Figure 3.11 right and Figure 3.12) while the 238 keV (Figure 3.11 left), 538 keV, and 69 keV (Figure 3.13) transitions decaying from the state at 2714 keV show only a single exponential decay. The least square fit of a single exponential decay function (Equation 3.1) to the added time distributions which showed one component yields an isomeric half-life value of 3.56(6) $\mu$s for the 2714 keV state (Figure 3.13). This value was then introduced as a constant into the two component function used in the fit of the decay curve which shows two components yielding the second isomeric half-life. The two component fitting function used is

$$\frac{dN}{dt} = \frac{ln2}{T^b_{1/2}} \left[ \left( -N^1_0 + \frac{N_0 \cdot T^b_{1/2}}{T^a_{1/2} - T^b_{1/2}} \right) e^{-ln2 \cdot t/T^b_{1/2}} - \frac{N_0}{(T^a_{1/2} - T^b_{1/2})} e^{-ln2 \cdot t/T^a_{1/2}} \right], \qquad (3.5)$$

where $N_0$ and $N^1_0$ are the initial population and the side feeding of the state and $T^{a,b}_{1/2}$ are the half-lives of the isomeric states. The two component fitting function is the decay of a state which belongs to the cascade and has direct feeding, as well. The fit of a two component exponential decay function to the added time distribution of the transitions below the 1871 keV isomeric state yields a half-life of 269(7) ns for this state.

The results of the individual fits to the time distributions of each $\gamma$ transition with respect to the ion implantation extracted from the energy versus time matrix are shown in Table 3.6. The ratio between the direct feeding to the 1871 keV state ($N_0$) and the total population ($N_0$+$N^1_0$) is shown in the last column of the table. The values obtained are in agreement with the relative intensities for the 238 keV and 538 keV transitions presented in Table 3.8.

As an alternative method to extract the half-lives of short lived isomeric states below a longer one which otherwise could have escaped observation, the $\gamma$ energy versus relative $\gamma$ time matrices gated by each of the transitions were created. The matrices

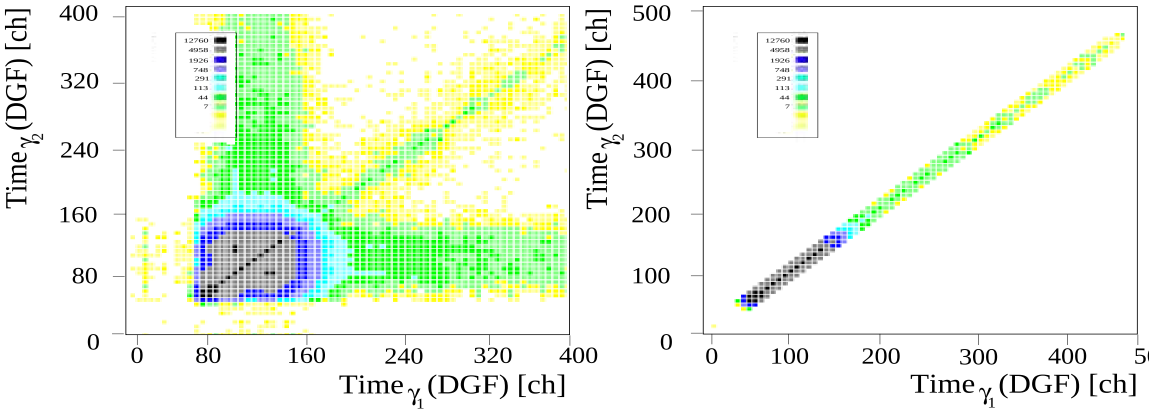


Figure 3.9: *tt matrices gated by $^{128}$Cd ions with different time conditions applied. Left: Without restriction on the time difference between the coincident $\gamma$-rays. Right: Time difference between two coincident $\gamma$ rays is smaller than 125 ns.*

Table 3.6: *$\gamma$-ray energy, fit of each $\gamma$ transition time distribution with respect to the ion implantation, relative intensities and ratio between the direct feeding of the 1871 keV state ($N_0$) and the total population ($N_0$+$N_0^1$) observed in the $^{128}$Cd isomeric decays.*

| $E_\gamma$ [keV] | $t_{1/2}$ [ns] | $t_{1/2}$ [ns] | $I_\gamma$[%] | $N_0/(N_0+N_0^1)$[%] |
|---|---|---|---|---|
| 68.7(1) | 3324(271) | | 13.5(9) | |
| 237.9(5) | 3498(82) | | 39(2) | |
| 440.0(3) | Fix | 261(8) | 84(4) | 48(3) |
| 450.4(3) | 3085(250) | | 1.8(3) | |
| 537.6(2) | 3607(77) | | 47(3) | |
| 645.8(2) | Fix | 272(9) | 100(5) | 46(3) |
| 765.0(3) | 3363(350) | | 1.2(2) | |
| 784.6(1) | Fix | 259(10) | 90(5) | 45(3) |
| 1224.0(6) | Fix | | 11(1) | |
| All | 3560(60) | 269(7) | | |

gated on the 238 keV (right) and 538 keV (left) transitions are shown in Figure 3.14. The time distributions associate to the 646 keV, 784 keV and 440 keV transitions show one decay component as expected (Figure 3.15 and 3.16). The half-life for the 1871 keV state amount to 270(7) ns and is in agreement with the value obtained with the two component fitting method.

The relative time difference between the 238 keV and 538 keV transitions is smaller than the resolution of the DGF electronics. Therefore, in order to determine the ordering of these two $\gamma$ transitions, the energy versus time difference matrices using the LR TDC electronics gated by each of these lines was created as it is shown in Figure 3.17. It is clear from this figure that the 238 keV transition is emitted after the 538 keV $\gamma$ ray.

The relative time distribution of the 538 keV transition with respect to the 238 keV line exhibits a Gaussian shape with an exponential tail as it is shown in Figure 3.18

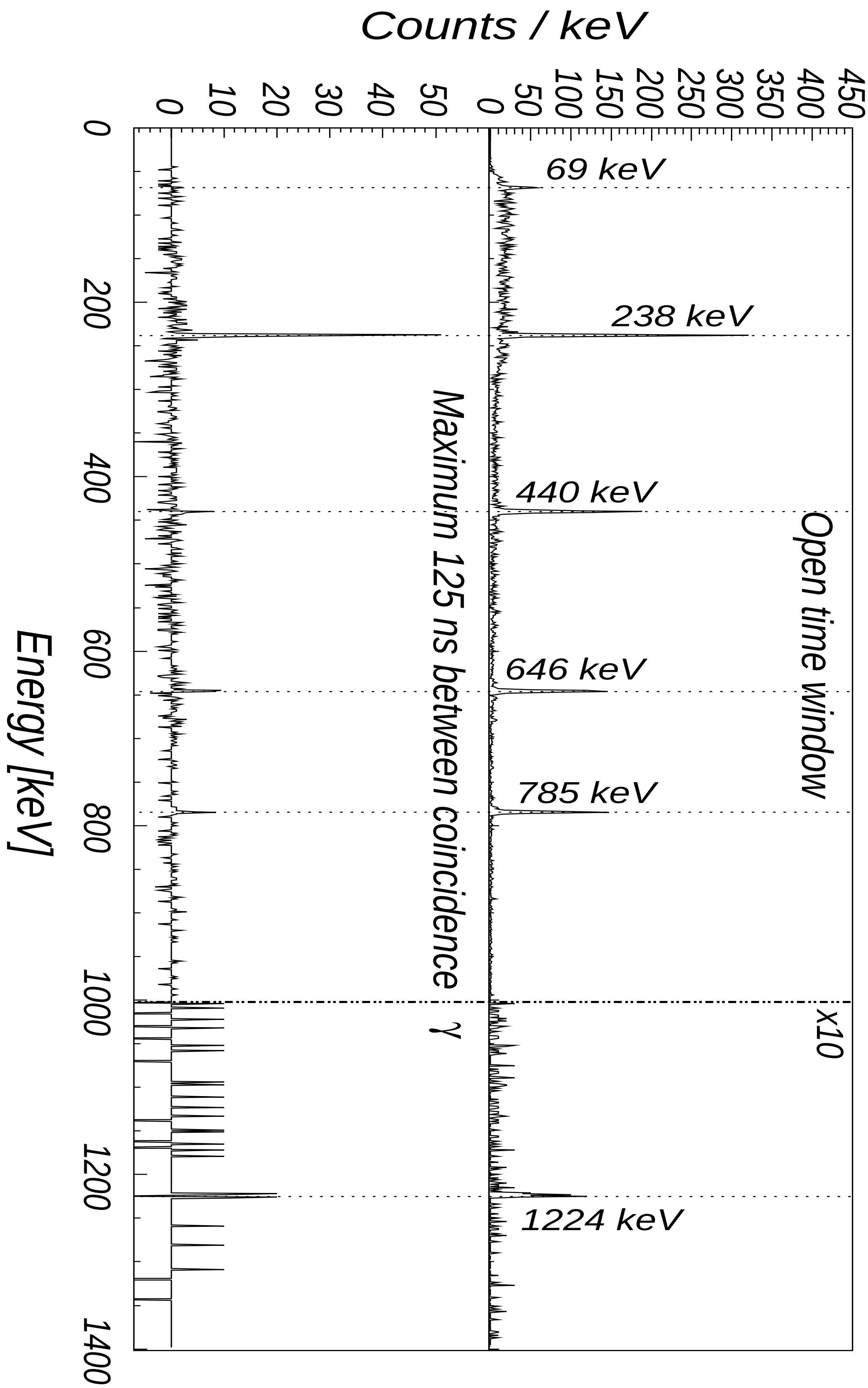


Figure 3.10: *$\gamma$ energy spectra extracted from the $\gamma\gamma$ matrices gated on the 538 keV transition in $^{128}$Cd. Top: With open time window. Bottom: Requiring that the time difference between the two coincident $\gamma$'s is smaller than 125 ns.*

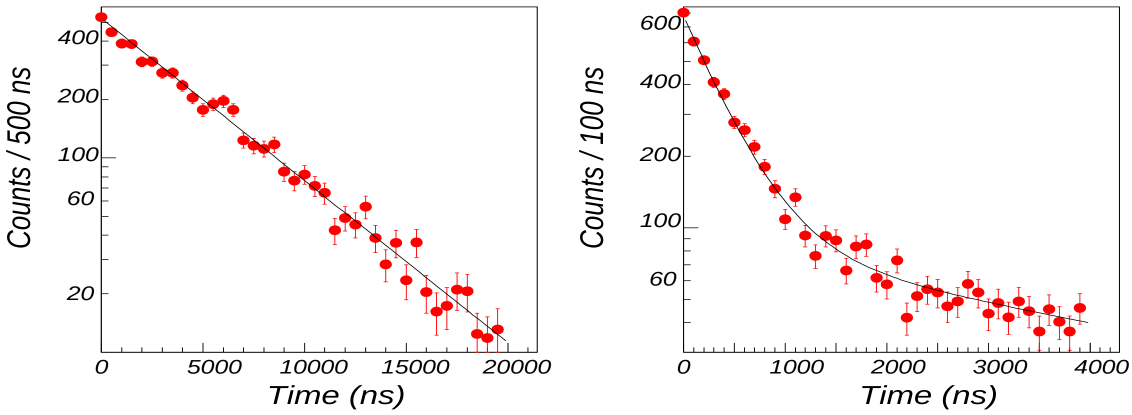


Figure 3.11: *Time distributions of the 238 keV (left) and 646 keV (right) $\gamma$ transitions in $^{128}$Cd relative to the ion implantation. The black curves show the results of the fits and the numerical values are summarized in Table 3.6.*

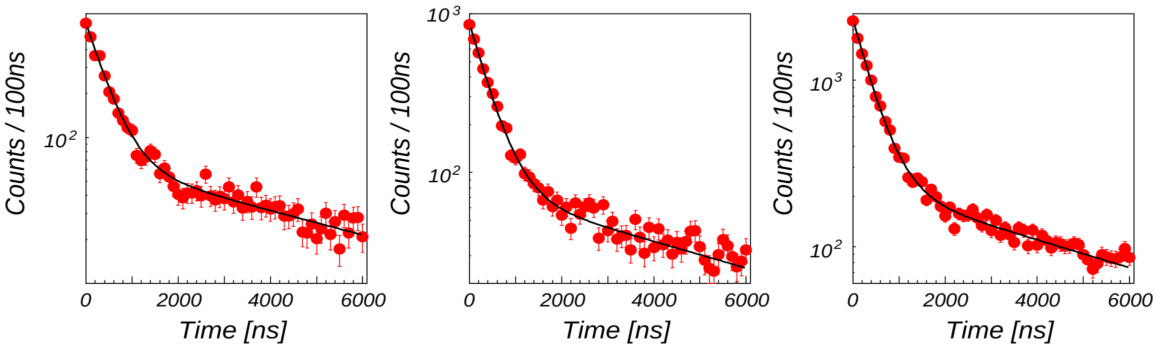


Figure 3.12: *Left: Time distribution associated to the 785 keV transition; Middle: Time distribution associated to the 440 keV transition; Right: Sum of the 646 keV, 784 keV, and 440 keV decay curves with respect to the $^{128}$Cd ion implantation time. The results of the fits are shown in Table 3.6.*

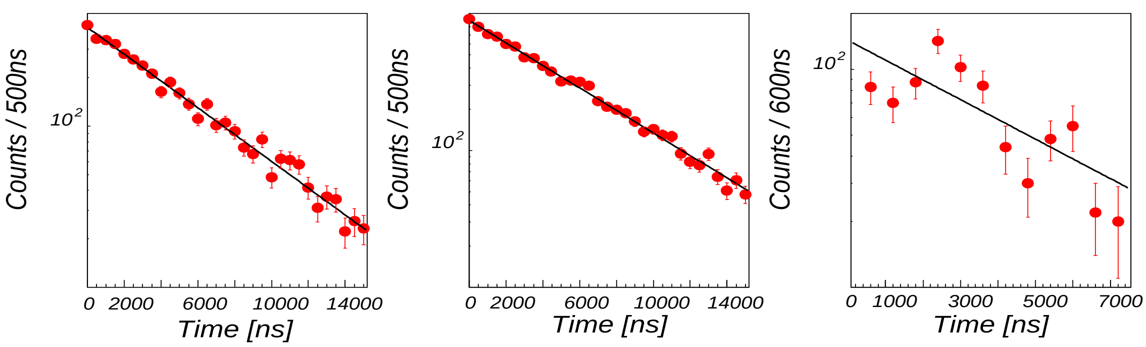


Figure 3.13: *Left: Time distribution associated to the 538 keV transition; Middle: Sum of the 238 keV and 538 keV decay curves; Right: 69 keV time distribution with respect to the $^{128}$Cd ion implantation time. The results of the fits are shown in Table 3.6.*

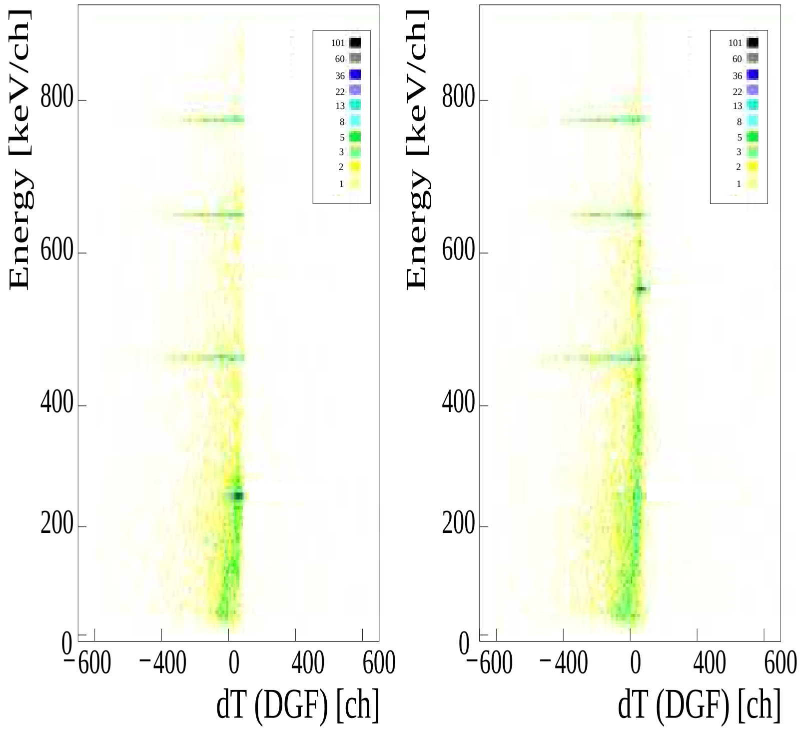


Figure 3.14: *$\gamma\gamma t$ matrices gated by the 538 keV (left) and 238 keV (right) transitions. The Ge digital electronics was used for the information of the $\gamma$-ray time.*

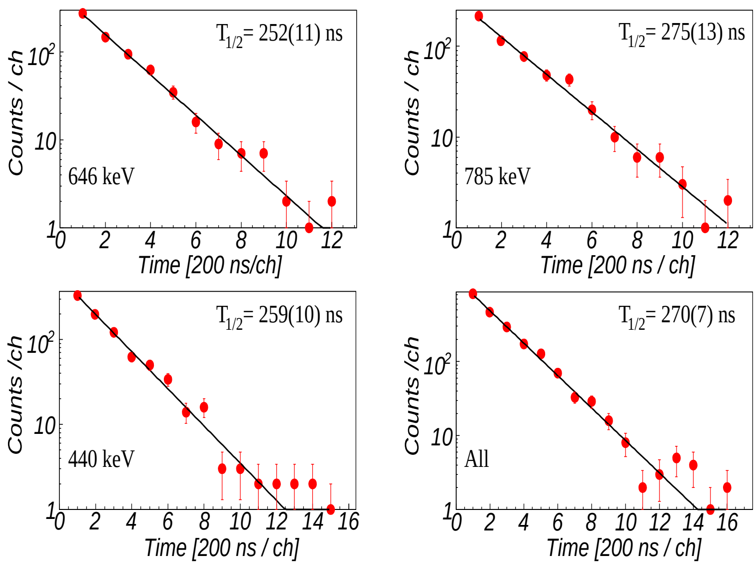


Figure 3.15: Time distributions of the $\gamma$ rays extracted from the $\gamma\gamma t$ matrix gatted by the 538 keV transition.

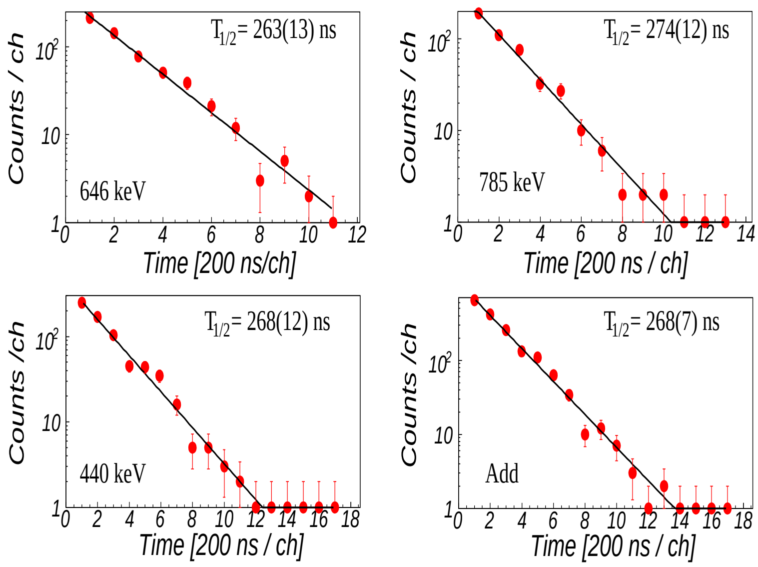


Figure 3.16: Time distributions of the $\gamma$ rays extracted from the $\gamma\gamma t$ matrix gatted by the 238 keV transition.

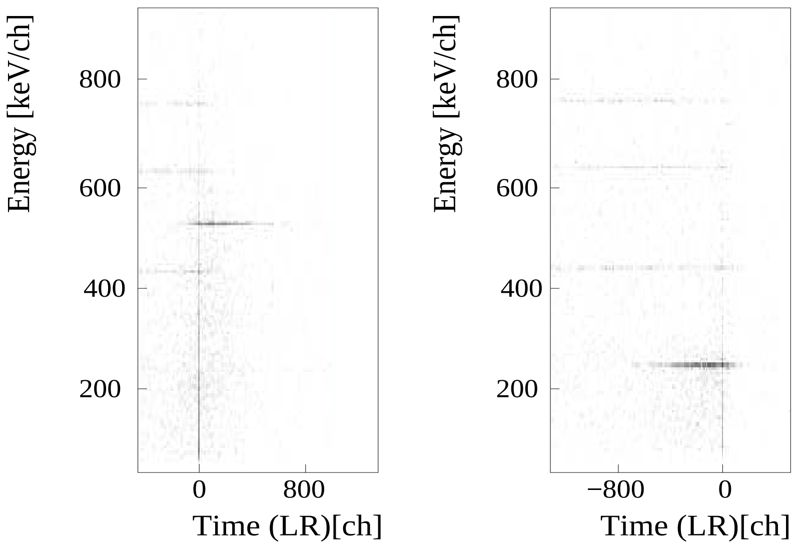


Figure 3.17: *$\gamma\gamma t$ matrices gated by the 538 keV (left) and 238 keV (right) transitions. The LR TDCs were used to obtain the information of the $\gamma$-ray time.*

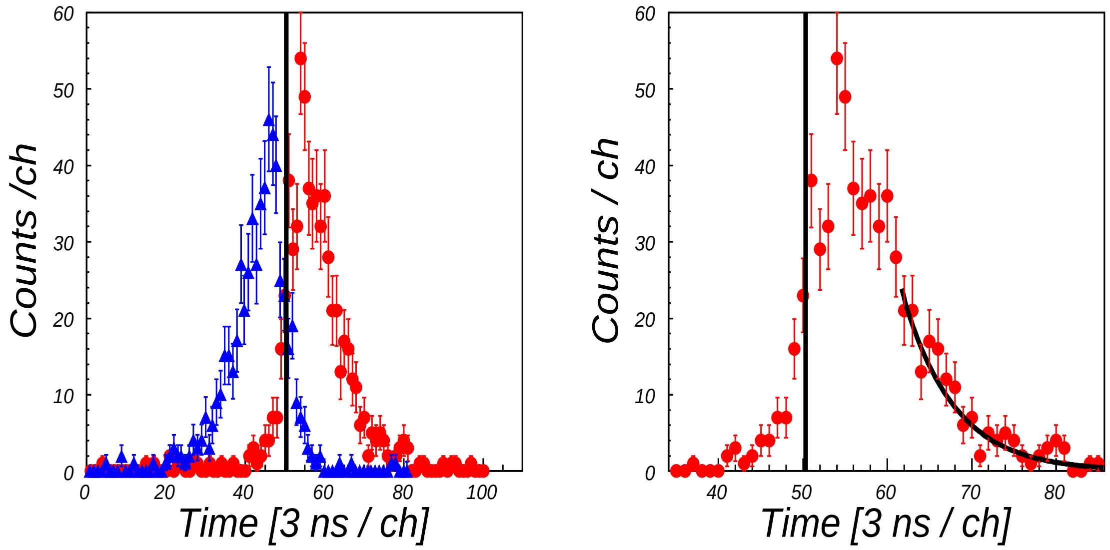


Figure 3.18: *Left: 238 keV time distribution with respect to the 538 keV transition (blue curve) and 538 keV time distribution with respect to the 238 keV transition (red curve). Both time distributions are symmetric with respect to the zero time line (black line). Right: 538 keV time distribution with respect to the 238 keV transition. The black curve represents the result of the least square fit.*

right. This time distribution can be use to extract the half-life of the state between these two $\gamma$ rays and it is analogue to the oposite case where the time distribution of the 238 keV transition with respect to the 538 keV line is analyzed thus the time distributions extracted in this two ways will mirror to each other (Figure 3.18 left). The least squares fit with a single exponential decay curve the exponential tail yields a 12(2) ns half-life for the isomeric state at energy of 2108 keV.

As a cross check, the centroid shift method was employed [96]. The effect of a exponential tail into a Gaussian distribution is a shift of the centroid. This shift can be quantified when comparing the centroids of the time distributions of prompt and delayed $\gamma$ transitions although the zero time line has to be determined. This zero time line is the origin of times which can be extracted by fitting the background around the peak of interest and shifting the curve obtained from the centroids to the position of the centroids of prompt coincidences. This shifting is necessary due to the time necesary for electron collection in the Ge detector for the scattered events [96] and it amounts $\sim$ 1 ns in this experiment. The prompt time distribution for higher energies was extracted from the $\gamma\gamma t$ matrix gating on the 646 keV transition and looking to the time distribution of the 785 keV transition which is prompt with respect to the latter. The fit with a Gaussian function yield to 10(4) ns FWHM. Similar analysis was performed for the time distribution of the 440 keV transition with respect to the 646 keV line. The zero time at lower energies was extracted by the mean value of the centroids of the time distributions of the 238 keV and 538 keV transitions with respect to the 538 keV and 238 keV lines, respectively (Figure 3.18 left). Figure 3.19 shows the background and zero line extracted. The 238 keV centroid with respect to the 538 keV is shown as well, the fact that this centroid appears at lower time than the zero line

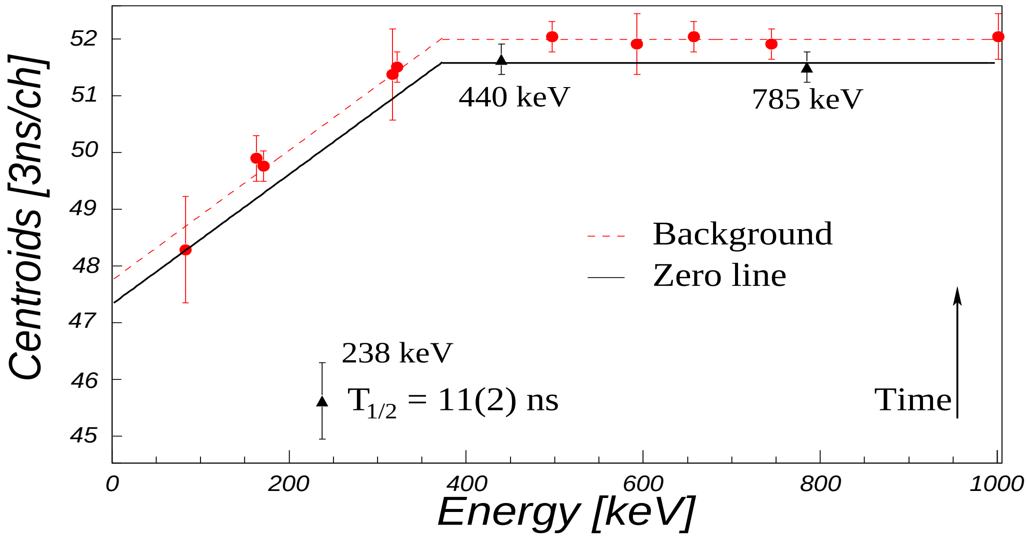


Figure 3.19: *Zero time line and centroid of the prompt component of the time distribution of the 238 keV transition. The shifting of the 238 keV centroid with respect to the zero time line is the half-life value of the 2108 keV state.*

is a probe that the 238 keV transition is emmitted after the 538 keV $\gamma$ ray. The shift amount 11(2) ns half-life for the isomeric state at 2108 keV excitation energy and it is in agreement with the least squares fit value.

Besides the strong $\gamma$-rays mentioned above two more weak transitions at 450 keV and 765 keV (Figure 3.7c and d) are observed in coincidence with the 646 keV and 785 keV lines, but not with the 538 keV transition. The 450 keV transition was placed as proceeding the one with 765 keV based on the weak coincidence relations of the 450 keV line with the 238 keV and 440 keV transitions. These two $\gamma$ rays are not in coincidence with the 765 keV transition. The one single count observed at the energy of 69 keV in the 765 keV $\gamma$ coincidence spectrum is expected considering that the 69 keV transition has only 5 % of the intensity of the 646 keV line. The 450 keV and 765 keV transitions form a parallel branch with an intermediate level at 2195 keV feeding the $4^+$ state at 1430 keV. Their time distributions show one component as expected for to the decay of the 2714 keV level (Figure 3.20). The sum energy of the 538 keV, 238 keV and 440 keV transitions is equal to that of the 450 keV and 765 keV lines forming a state at 2646 keV.

The 69 keV transition is placed decaying from the isomeric state at 2714 keV excitation energy. Due to the side feeding to the state at energy of 1871 keV it was not possible to extract the conversion coefficient of this $\gamma$ line by the missing intensity with respect to the $2^+ \rightarrow 0^+$ transition as it has been done in the case of the 128 keV and 138 keV transitions in $^{130}$Cd. The relative intensity of the 69 keV transition with respect to the 646 keV line was extracted from the areas of the $\gamma$ peaks observed in the 238 keV and 538 keV coincidence spectra extracted from the $\gamma\gamma$ matrices with the condition of open time window applied. The results are summarized in Table 3.7. In addition the experimental conversion coefficient of the 238 keV transition was extracted from the missing intensity with respect to the 646 keV line observed in the 538 keV

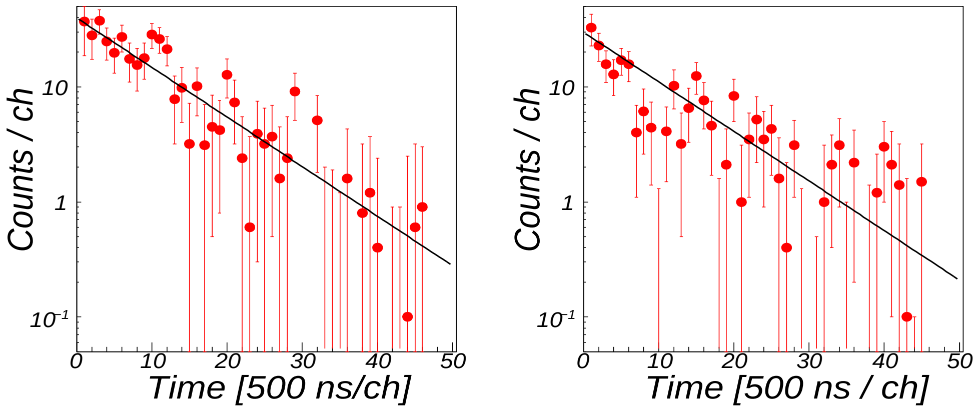


Figure 3.20: *Left: Decay curve of the 450 keV transition. Right: Decay curve associated to the 765 keV $\gamma$ line. Both curves show a single exponential decay component in the time distribution.*

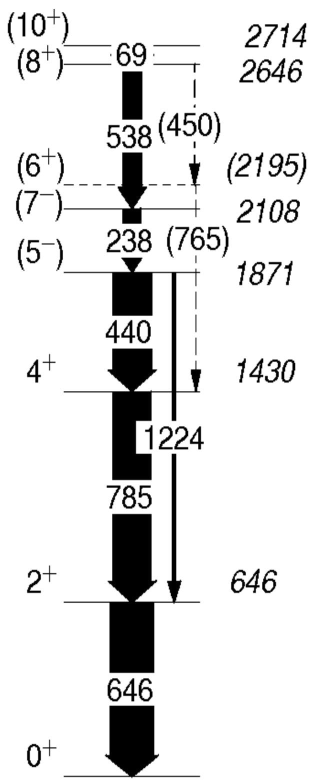


Figure 3.21: *Deduced experimental level scheme for the isomeric deexcitation of $^{128}$Cd.*

coincidence spectrum. The time distribution of the 69 keV transition was extracted from the number of counts observed in the $\gamma$ peak from the spectrum extracted from the energy versus time matrix applying consecutive time windows of 600 ns. The resulting spectrum is shown in Figure 3.13 right. The half-life value (Table 3.6) obtained from the fit of a single exponential decay curve to the time distribution agrees with the value obtained from the fit of the added time distributions of the 238 keV and 538 keV transitions.

Table 3.7: *$\gamma$ ray energies and inferred experimental conversion coefficient compared to the theoretical values in $^{128}$Cd.*

| $E_\gamma$ | 238 keV gate $\alpha_{exp}$ | 538 keV gate $\alpha_{exp}$ | $\alpha$(E1) | $\alpha$(M1) | $\alpha$(E2) |
|---|---|---|---|---|---|
| 68.7(1) | 6.38(86) | 7.84(1.46) | 0.498(7) | 1.392(20) | 5.90(9) |
| 237.9(5) | | 0.0742(0.103) | 0.015(2) | 0.044(1) | 0.0717(10) |

The $\gamma$-ray energies, their relative intensities normalized to the 646 keV transition and the half-lives of the isomeric states in $^{128}$Cd, observed in this experiment are summarized in Table 3.8.

Table 3.8: *Experimental $\gamma$ ray energies, half-lives and deduced spin and parity assignments for the excited states in $^{128}$Cd. The $\gamma$ intensities are normalized to the 646 keV transition.*

| $E_i$ [keV] | $t_{1/2}$[$\mu$s] | $I_i^\pi \rightarrow I_f^\pi$ | $E_\gamma$ [keV] | $I_\gamma$[%] | $\alpha_{exp}$ |
|---|---|---|---|---|---|
| 646 | | $2^+ \rightarrow 0^+$ | 645.8(2) | 100(5) | |
| 1430 | | $4^+ \rightarrow 2^+$ | 784.6(1) | 90(5) | |
| 1871 | 0.269(7) | $(5^-)\rightarrow(4^+)$ | 440.0(3) | 84(4) | |
| | | $(5^-)\rightarrow(2^+)$ | 1224.0(6) | 11(1) | |
| 2108 | 0.012(2)[a] | $(7^-)\rightarrow(5^-)$ | 237.9(5) | 39(2) | |
| 2195 | | $(6^+)\rightarrow(4^+)$ | 765.0(3) | 1.2(2) | |
| 2646 | | $(8^+)\rightarrow(7^-)$ | 537.6(2) | 47(3) | |
| | | $(8^+)\rightarrow(6^+)$ | 450.4(3) | 1.8(3) | |
| 2714 | 3.56(6) | $(10^+)\rightarrow(8^+)$ | 68.7(1) | 13.5(9) | 6.38(86)[b] |

[a ] Extracted from the energy versus time matrix gated on the 537 keV transition.

[b ]Extracted from the $\gamma\gamma$ matrix gating on the 238 keV transition.

In addition to the previously mentioned observed $\gamma$ rays, four weak lines at energies of 214 keV, 432 keV, 528 keV and 572 keV (Figure 3.22a, b, c and d) were observed in coincidence with the 646 keV, 785 keV and 440 keV transitions. However the low statistics did not allow their placement in the level scheme.

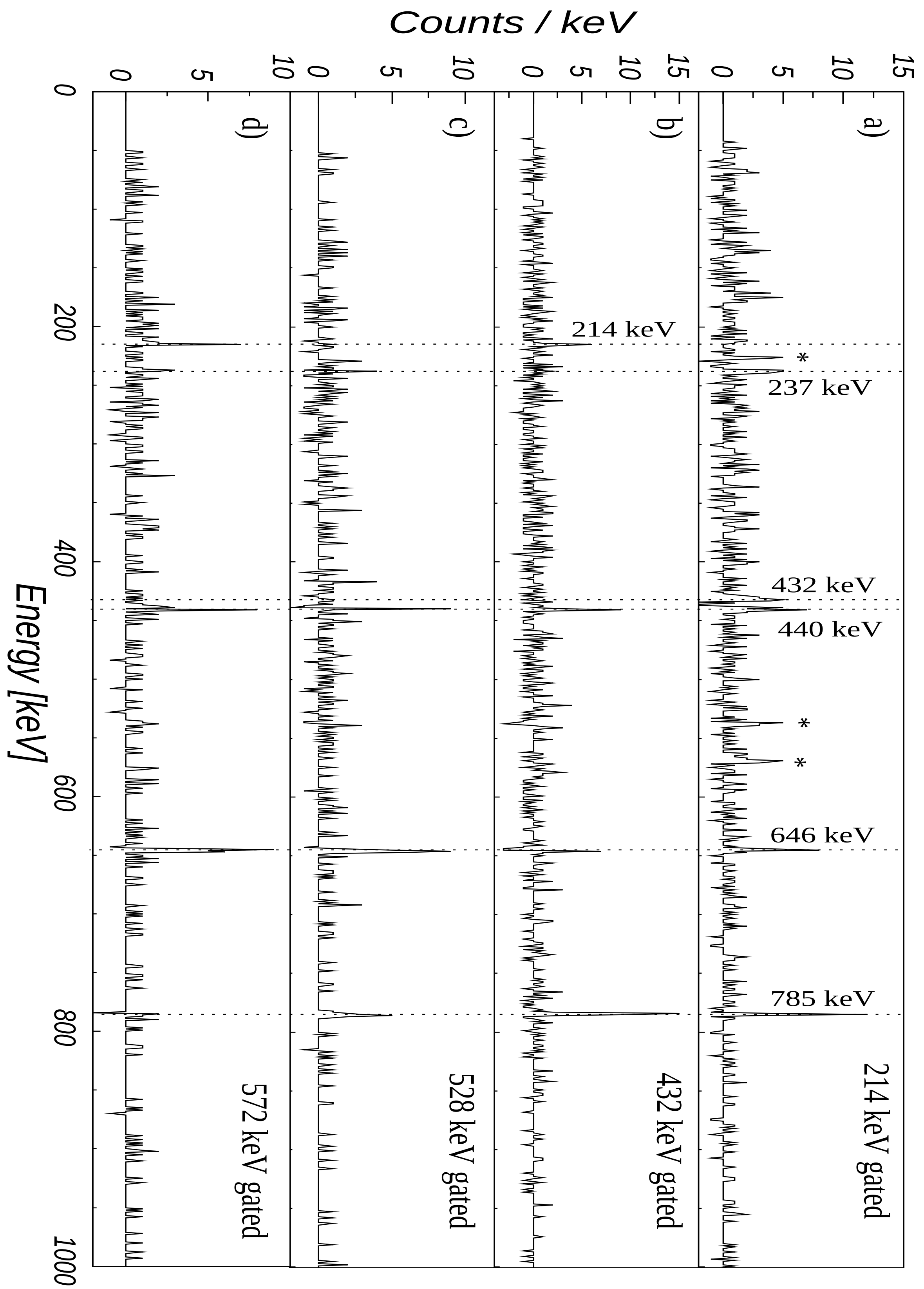


Figure 3.22: *Resulting spectra gated by the 214 keV (a), 432 keV (b), 528 keV (c) and 572 keV (d) transitions. The low statistics did not allow the placement of these $\gamma$ rays in the level scheme.*

The spin and parity assignment for the excited states has been performed based on the electromagnetic transitions probabilities and conversion coefficients (Figure 3.21). The isomeric state at 1871 keV decays mainly by a 440 keV $E1$ $\gamma$ ray to the $4^+$ level with B(E1; $(5^-) \rightarrow 4^+$) = 9.74(61)$\times10^{-9}$ W.u. and a parallel branch to the $2^+$ by the 1224 keV $E3$ $\gamma$ line with B(E3; $(5^-) \rightarrow 2^+$) = 0.125(13) W.u. This $E3$ strength is comparable to the value B(E3; $7^- \rightarrow 4^+$) = 0.133 W.u. in $^{128}$Sn [29] four neutron holes in the doubly-magic $^{132}$Sn. An $E4$ character for the 1224 keV transition would not account for the experimental half-life therefore $I^\pi = (5^-)$ is assigned to the 1871 keV level.

The multipolarity assignments for the 238 keV, 450 keV, 538 keV and 765 keV transitions are based on the following arguments. The 2108 keV isomeric state decays by the 238 keV transition to the 1871 keV level. The experimental conversion coefficient associated to this $\gamma$ ray was measured yielding 0.0742(0.103), a value which compares well to the theoretical $\alpha$(E2) = 0.0717, although the large errors does not permit to discard a possible $M1$ character for this transition. However, since the experimental value is very small it does not allow for any reliable conclusion based on this measurement. Assuming $E2$ character for the 238 keV transition, the B(E2; $(7^-) \rightarrow (5^-)$) = 1.51 (26) W.u. strength is comparable to the $E2$ strength in $^{130}$Sn [26].

The 2646 keV level decays by the emission of a 538 keV $\gamma$-ray to the 2108 keV level and via a weak 450 keV transition to the 2195 keV state. The B(E1; $8^+ \rightarrow 7^-$) $> 3.5\times10^{-6}$ W.u. strength in $^{130}$Sn [26] would correspond to a half-life of $< 0.5$ ns for the 2646 keV state which cannot be excluded from our data. Within the experimental sensitivity the 538 keV transition is emitted promptly after the 69 keV $\gamma$ ray. As the spin difference between the 1430 keV and 2646 keV levels is $4\hbar$ both the 450 keV and 765 keV $\gamma$ rays have to be $E2$ transitions. The assignment of a higher multipolarity to any of those transitions would lead to a half-life longer than 50 $\mu$s for the 2195 keV or 2646 keV states. The latter is therefore assigned to $I^\pi = (8^+)$. The exchange of the spin and parity for the 2108 keV and 2195 keV levels would be at variance with the non observation of a 325 keV transition feeding the 1871 keV state. Therefore $I^\pi = (7^-)$ is assigned to the 2108 keV level and $I^\pi = (6^+)$ to the excited state at 2195 keV. The isomeric state at 2714 keV excitation energy was attributed spin and parity $(10^+)$. It decays by a 69 keV $E2$ transition of 0.39(1) W.u. strength to the 2646 keV level. The experimental conversion coefficient for this $\gamma$ ray was inferred by intensity balance arguments to be 6.38(86) in agreement with the theoretical value of $\alpha_{tot}$(E2) = 5.9 thus corroborating this assignment.

## 3.3 The nucleus $^{126}$Cd

Information concerning the excited states in $^{126}$Cd has been reported in recent publications [94, 97, 41]. The higher production cross section of this nucleus allowed to experimentally access this isotope more easily than the more neutron rich ones. Despite the experimental results previously reported, the nuclear structure associated to the isomeric decay of this nucleus is not completely understood. Motivated by this fact, a specific setting of the FRS was dedicated to the study of $^{126}$Cd. In total $6.57\times10^5$ ions were identified, adding the statistics both when $^{130}$Cd was describing the central trajectory of the FRS and in the $^{126}$Cd setting.

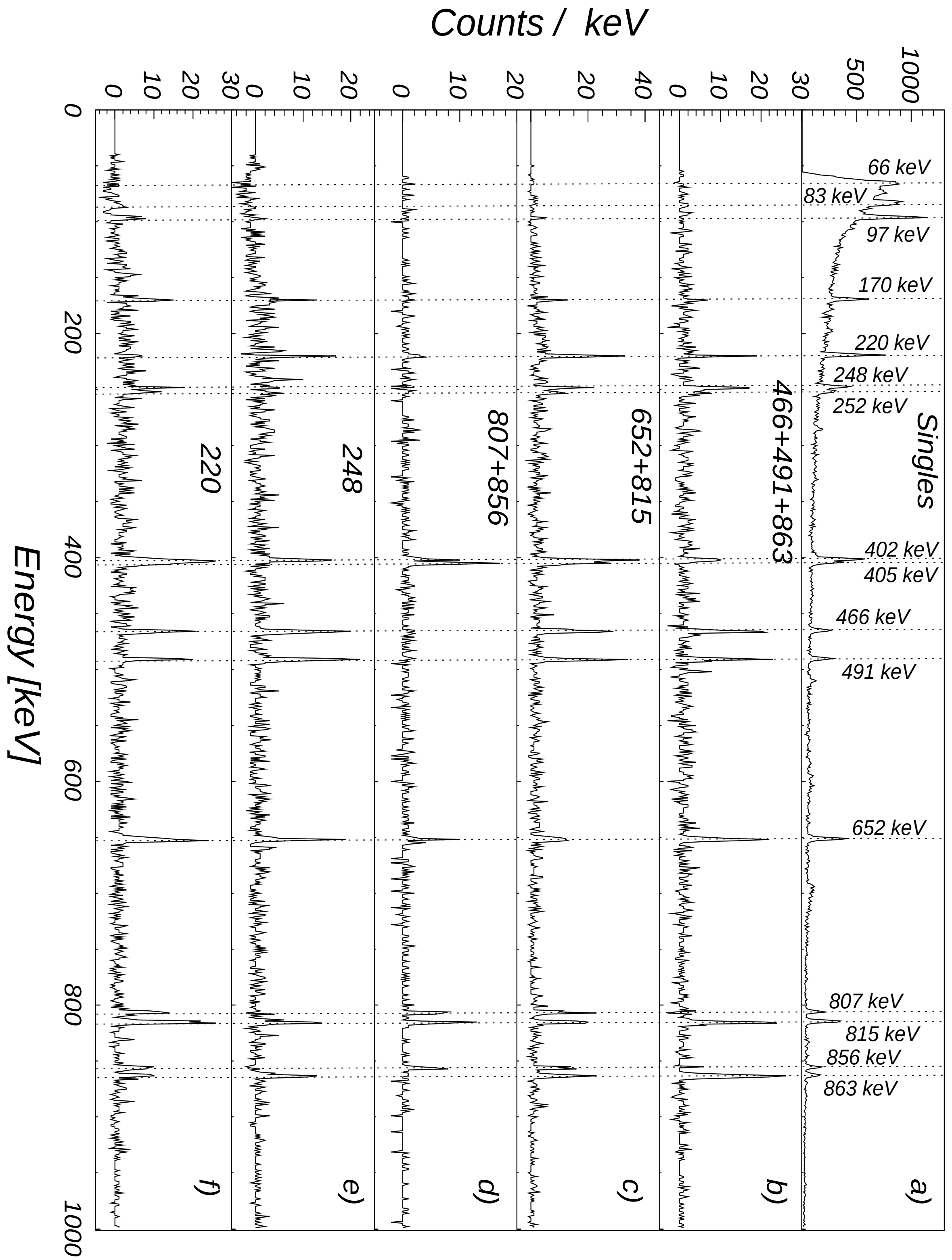


Figure 3.23: *Spectra observed in coincidence with $^{126}$Cd; a): Singles $\gamma$ energy spectrum. Summed spectra extracted from the prompt $\gamma\gamma$ matrix with the condition that the maximum time difference between two $\gamma$ rays is smaller than 125 ns, gated by: b) 466 keV, 491 keV and 863 keV transitions, c) 615 keV and 815 keV transitions, d) 807 keV and 856 keV transitions, e) and f) only 248 keV and 220 keV transitions, respectively.*

The single $\gamma$ energy spectrum in coincidence with $^{126}$Cd is shown in Figure 3.23a. The $2^+ \rightarrow 0^+$ and $4^+ \rightarrow 2^+$ transitions at energies of 652 keV and 815 keV, respectively, are visible. These $\gamma$ rays were reported previously in a $\beta$-decay study of the heavy Ag isotopes [41]. In a later experiment, Walters et al. [97], observed additional $\gamma$ transitions at 219 keV, 248 keV, 401 keV, 583 keV and 807 keV energy. In Reference [94] all these transitions are confirmed to belong to the isomeric decay of $^{126}$Cd with the exception of the line at 583 keV. Additional two $\gamma$ rays at 405 keV and 856 keV energy were reported. The $\gamma$ ray energies from [97] and [94] differ by 1 keV in some cases. In this work, the $\gamma$ peaks observed in [94] are visible and the energies are in agreement to those reported in [94]. Also the non-observation of the 583 keV $\gamma$ line is confirmed. The high efficiency of the Ge array allowed to measure additional $\gamma$ transitions at 863 keV and 252 keV and also at very low-energy at 66 keV, 83 keV and 97 keV. The $\gamma$ energies, their relative intensities with respect to the first excited state and conversion coefficients measured in this experiment are shown in Table 3.9.

Table 3.9: *$\gamma$ ray energies, relative intensities normalized to the 652 keV transition, conversion coefficients and half-lives observed in the $^{126}$Cd isomeric decay.*

| $E_\gamma$ [keV] | $I_\gamma$[%] | $t_{1/2}$[ns] | $\alpha_{exp}$ |
|---|---|---|---|
| 66.4(2) | 66(5) | 1720(70) | 0.51(47) |
| 82.7(2) | 52(7) | | |
| 96.7(1) | 108(9) | | |
| 170.1(1) | 58(5) | | |
| 220.0(1) | 92(7) | | |
| 248.3(1) | 49(4) | | |
| 252.4(1) | 31(3) | | |
| 402.2(1) | 93(7) | | |
| 405.3(1) | 50(5) | | |
| 466.2(1) | 47(4) | | |
| 491.1(1) | 50(5) | | |
| 652.3(1) | 100(8) | | |
| 806.8(1) | 46(4) | | |
| 815.2(1) | 100(8) | | |
| 856.2(1) | 43(4) | | |
| 863.4(1) | 42(4) | | |

The 402 keV transition was placed feeding the 1467 keV level deexciting the 1869 keV state based on the observation of this peak in the previous experiments [41, 94, 97] and the fact that it has the same intensity than the 652 keV transition. Due to the similar energy of the $\gamma$ rays at 402 keV and 405 keV, no analysis of the time distribution of these two lines was performed.

The transitions at 83 keV, 170 keV and 252 keV energy were reported in [98] although no evidence for this observation is shown. These three transitions form two parallel branches depopulating the state at 2122 keV energy.

The $\gamma\gamma$ coincidence analysis was performed based on the analysis of three different

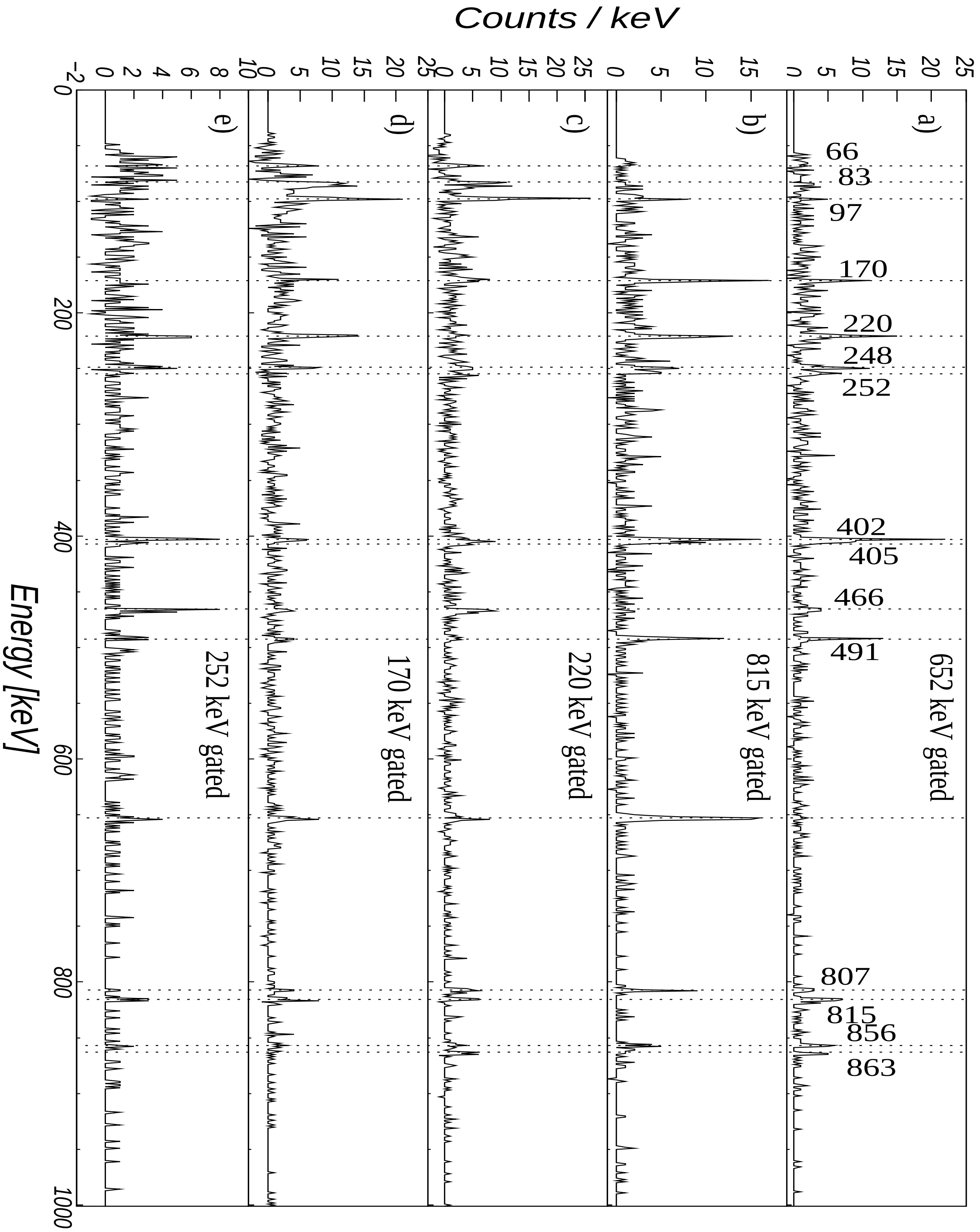


Figure 3.24: *Spectra extracted from the prompt $\gamma\gamma$ matrix with the condition that the maximum time difference between two $\gamma$ rays is smaller than 20 ns; a) gated by 652 keV line, b) gated by 815 keV line, c) gated by 220 keV line, d) gated by 170 keV line and e) gated by 252 keV line.*

type of matrices, namely, without time condition applied and requiring that the time difference between the two coincident $\gamma$ rays is smaller than 125 ns (Figure 3.23) and 20 ns (Figure 3.24, 3.25 and 3.26), respectively. Additional matrices with the condition that the maximum time difference between $\gamma$ rays is smaller than 30 ns, 10.5 ns, 7.5 ns and 3 ns were constructed as well and are shown in Apendix A. The resulting spectra under these last conditions will not be discussed further in view of the analogy with the resulting spectra obtained from the matrices with open, 125 ns and 20 ns conditions applied.

In the $\gamma\gamma$ coincidence analysis with the condition of 20 ns time difference between coincident $\gamma$ rays it is observed that the 170 keV (Figure 3.24d) and 252 keV (Figure 3.24e) transitions are not in coincidence, while the 83 keV $\gamma$ line is visible in the resulting spectrum when gating on the 170 keV line, proving unambiguously the existence of two branches depopulating the state at 2122 keV. This observation is confirmed by the analysis of the $\gamma\gamma$ matrix with the condition of 125 ns time difference between coincident $\gamma$ rays. The 2122 keV state is depopulated by a 252 keV $\gamma$ ray to the 1869 keV state and a parallel branch formed by the 170 keV and 83 keV $\gamma$ rays with an intermediate level at 1952 keV excitation energy. The time distribution associated to the 170 keV and 83 keV transitions with respect to the ion implantation shows a single exponential decay and the least square fit yielded 1720(80) ns and 1730(100) ns (Figure 3.27 left) half-life value, respectively. The analysis of the time distribution associated to the 252 keV transition could not be performed since this line forms a doublet with the 248 keV $\gamma$-ray. The 83 keV, 170 keV and 252 keV conversion coefficients were not possible to extract because it is not possible to estimate if the missing intensity with respect to the 646 keV transition is caused by the branching or by the conversion of the $\gamma$-rays.

The 220 keV transition was placed populating the level at 2122 keV energy based on its strong coincidence with the 815 keV $\gamma$ ray, an observation confirmed from the analysis of the $\gamma\gamma$ matrices both with 125 ns (Figure 3.23c and f) and 20 ns (Figure 3.24c) maximum time difference between two coincident $\gamma$ rays. Based on the same argument the 97 keV was placed feeding the 2342 keV state. The time distributions associated to the 97 keV and 220 keV transitions with respect to the ion implantation were fitted with a single exponential decay function yielding the 1510(60) ns (Figure 3.27 middle) and 2170(100) ns half-lives, respectively.

The 863 keV, 248 keV, 491 keV and 466 keV transitions are in mutual coincidence (Figure 3.23b, 3.25) but not with the 405 keV, 807 keV and 856 keV lines (Figure 3.23c, 3.26). These sets of $\gamma$ rays form two parallel branches depopulating the state at 4507 keV energy. This statement is based on two arguments, the first is that the sum energy of the 863 keV, 248 keV, 491 keV and 466 keV transitions is equal to that of the 405 keV, 807 keV and 856 keV $\gamma$ rays, and the second that the sum of the relative intensities of the two branches is equal to that of the 652 keV transition. The time distributions of all the lines between the 2439 keV and 4507 keV levels present a single exponential decay. The summed distribution of the 863 keV, 491 keV, 466 keV, 807 keV and 856 keV transitions is shown in Figure 3.31 and the fit with a single exponential decay function yield a half-life of 1720(70) ns. The individual time distributions of this $\gamma$ rays are shown in Apendix B. The statistics was not sufficient to perform an angular correlations analysis which would have shed light on the spin and parity assignment

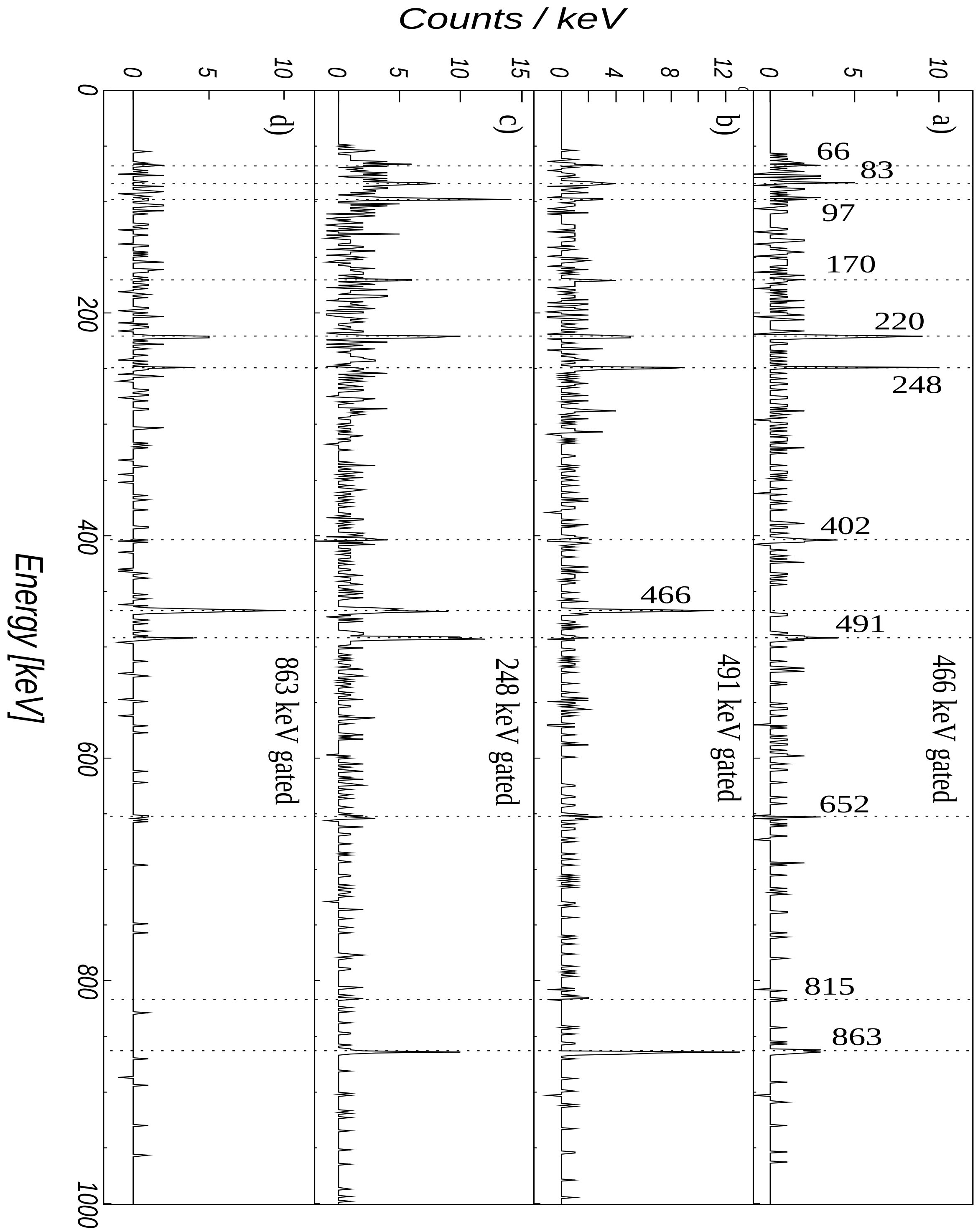


Figure 3.25: *Spectra extracted from the prompt $\gamma\gamma$ matrix with the condition that the maximum time difference between two $\gamma$ rays is smaller than 20 ns; a) gated by the 466 keV line, b) gated by the 491 keV line, c) gated by the 248 keV line and d) gated by the 863 keV line.*

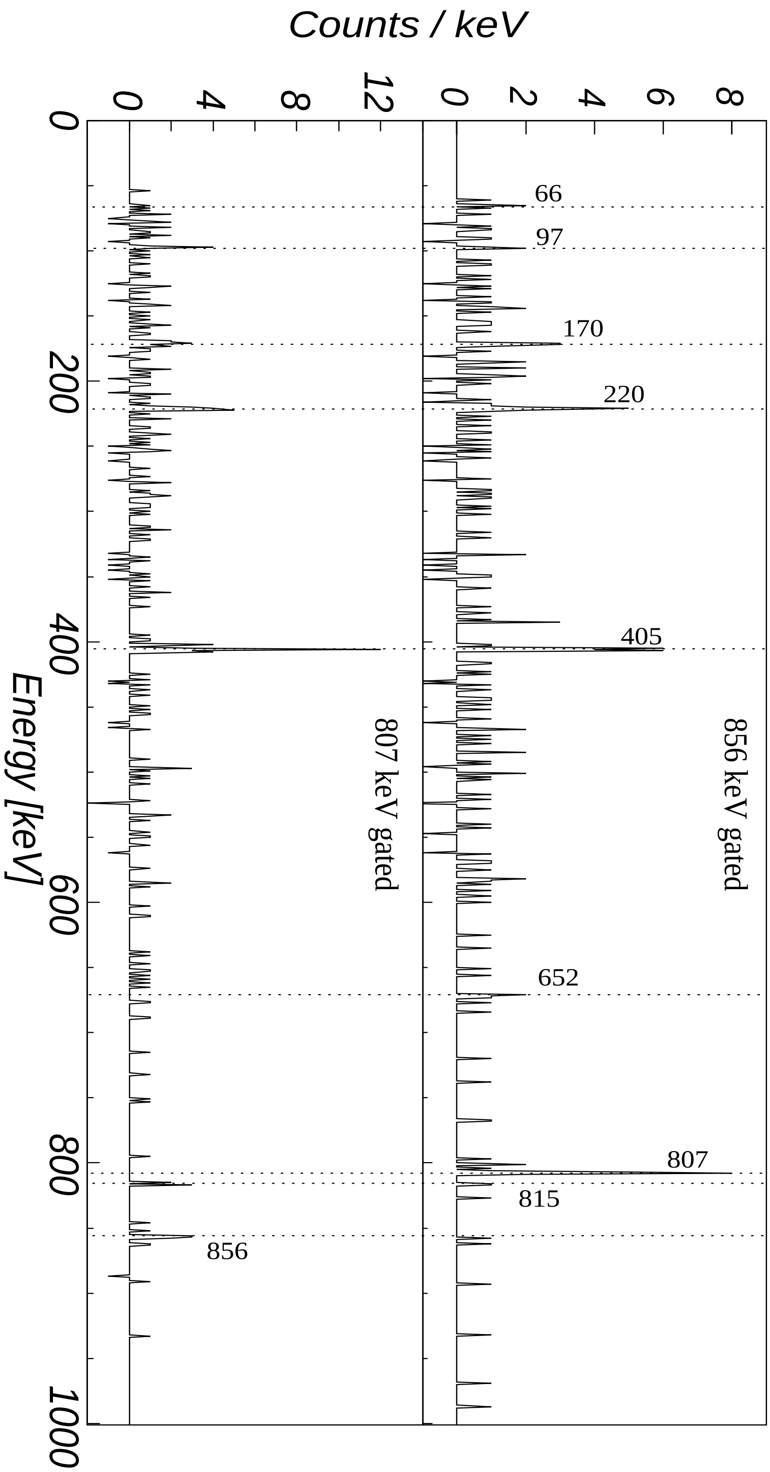


Figure 3.26: *Spectra extracted from the prompt $\gamma\gamma$ matrix with the condition that the maximum time difference between two $\gamma$ rays is smaller than 20 ns; a) gated by 856 keV line and b) gated by 807 keV line*

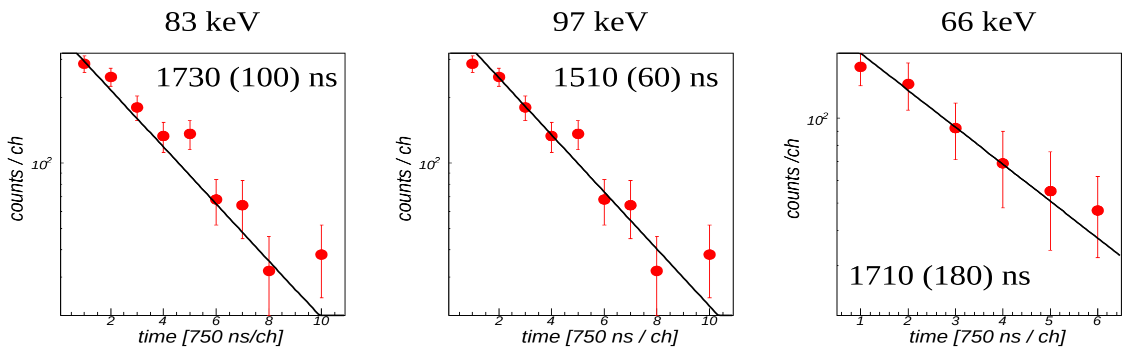


Figure 3.27: *Time distributions with respect to the implantation of $^{126}$Cd for the 83 keV (left), 97 keV (middle) and 66 keV (right) transitions.*

to the intermediate states between the level at 4507 keV and the one at 2439 keV excitation energy.

The matrices of $\gamma$ energy versus time difference between the detected $\gamma$ rays and the transitions between the states at energies of 2439 keV up to 4507 keV were constructed. It is not expected that any of these levels are isomeric, therefore the distribution should be symmetric with respect to the zero time. This zero time is normally extracted by fitting with a Gaussian function the time distributions of the background around the transition of interest [96] and shifting the evolution of the prompt time distribution with the energy to the prompt coincident $\gamma$ transitions. It was not possible to extract the zero time in this way for this data set of $^{126}$Cd due to the low statistics and it was assumed to be as in $^{128}$Cd. The prompt coincidence of the 652 keV line with the 815 keV transition serve as test for this assumption. It was observed that the centroid of the time distribution of the latter is slightly shifted to the $^{128}$Cd zero time (Figure 3.28), although is within the error bars. This effect is caused by the low statistics as mentioned in Reference [96] and the assumption is believed to be correct. The time distributions of the 466 keV, 491 keV and 248 keV transitions were symmetric with respect to the zero time but it was observed that the centroid of the time distribution of the 863 keV transition was shifted when the matrices where gated by the other $\gamma$ rays (Figure 3.29). The Gaussian fit yield to 4(1) ns for the state from where the 863 keV transition is emitted. It is clear that the low statistics introduces an error into the fitted value, therefore this half-life is considered only as an upper limit. Even though, it can be concluded that the 863 keV transition is emitted before than the other three from a state at 3302 keV excitation energy.

From the same matrices the relative time distribution of the 220 keV transition was extracted. It presents a symmetric distribution around the zero point as expected and the fit with a Gaussian function yield to 14(3) ns FWHM (Figure 3.30). This observation lead to the conclusion that the 97 keV transition is not isomeric or its half-life value is smaller than the time resolution of the Ge detectors.

Additionally the relative time distribution of the 652 keV transition was extracted from the matrix of $\gamma$ energy versus time difference between this $\gamma$ rays and any of the transitions between the states at energies of 2439 keV up to 4507 keV. The centroid shift analysis yield a 11(1) ns half-life (Figure 3.28). This value can not be attributed exclusively to any of the transitions between the 2439 keV and 1869 keV, although it is

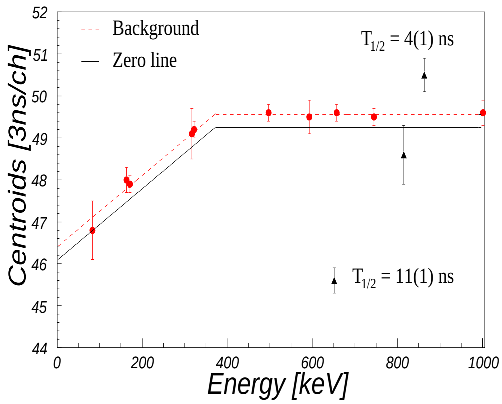


Figure 3.28: *Line zero and centroid of the 652 keV, 815 keV and 863 keV transitions. The centroids of 652 keV and 863 keV lines are shifted with respect to the zero time line demonstrating the existence of isomeric states. See text for details.*

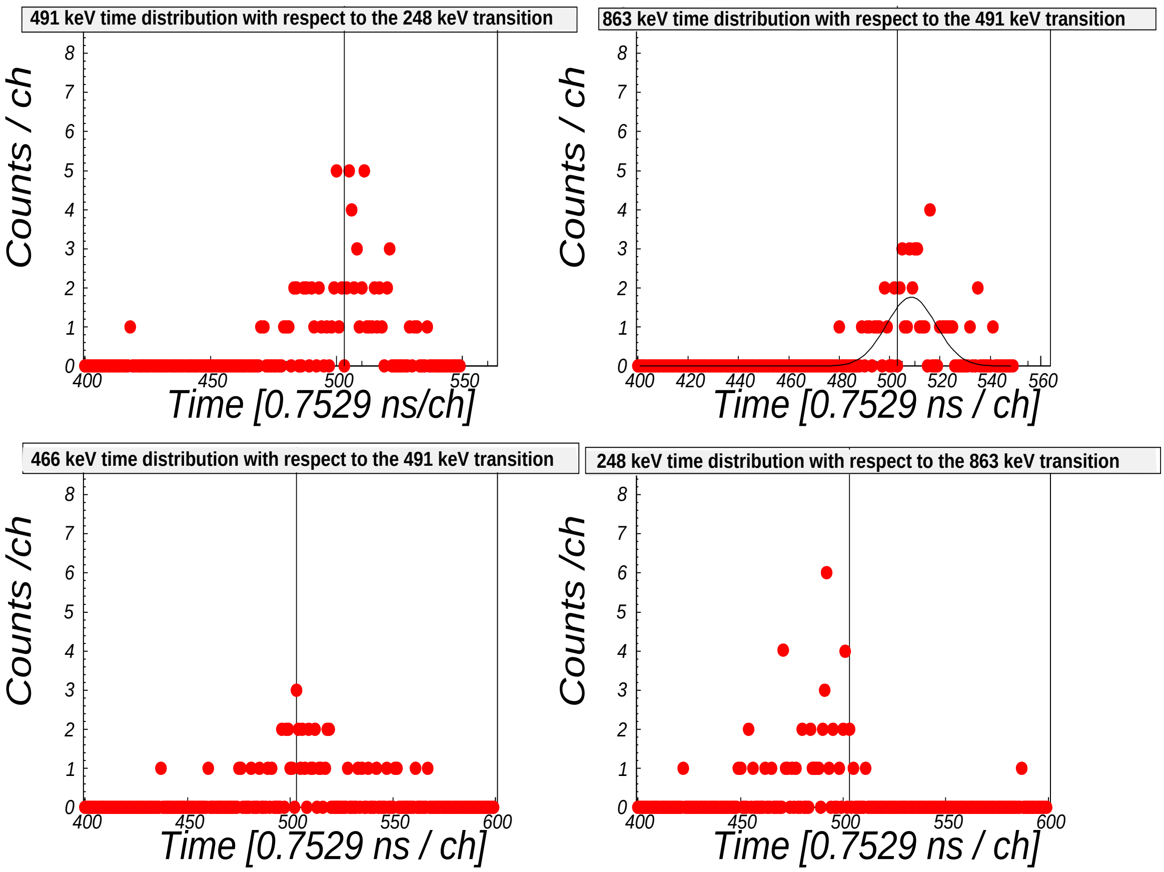


Figure 3.29: Relative time distributions of the 248 keV, 466 keV, 491 keV and 863 keV transitions of $^{126}$Cd. The black line shows the zero time and the black curve represent the Gaussian fit to the time distribution.

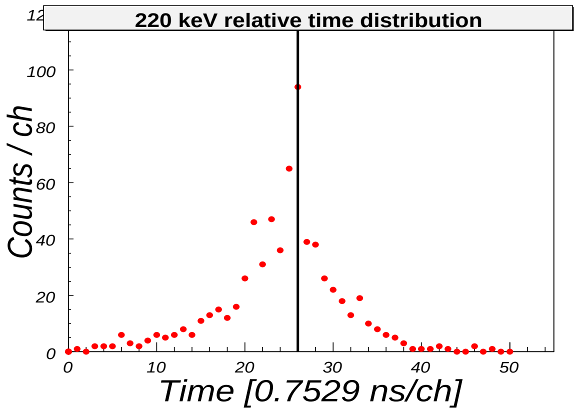


Figure 3.30: Relative time distributions of the 220 keV transition with respect to the lines between the 2439 keV and 4573 keV states of $^{126}$Cd. The black line shows the zero time.

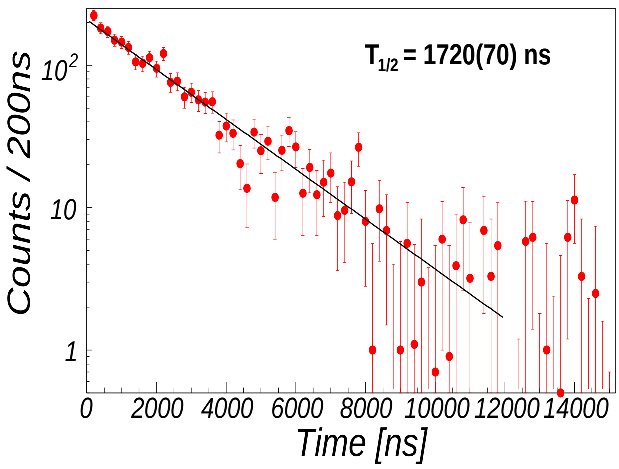


Figure 3.31: *Time distribution associated to the isomeric decay of* $^{126}$*Cd with respect to the ion implantation.*

expected to be associated to the 83 keV transitions due to the 170 keV will have shorter half-lives. Therefore the half-lives resulted from the single exponential decay fit to the time distribution of the 83 keV and 97 keV transitions is an effect due to the feeding of the 2439 keV and 1952 keV levels by the isomeric state at 4573 keV excitation energy.

The 66 keV transition is placed deexciting the isomeric state at 4573 keV excitation energy. The time distribution of this transition with respect to the ion implantation presents a single exponential decay curve yielding a 1710(180) ns half-life as it is shown in Figure 3.27 right. The large errors bars in this fit are due to the low Ge detector response at low energies. The isomeric state at 4573 keV excitation energy has 1720(70) ns half-life. This results is in disagreement with the non observation of isomeric states with half-lives longer than 0.5 $\mu$s in the heavy Cd isotopes reported by Scherillo et al. [100].

It is noticed that in the spectra obtained by gating the $\gamma\gamma$ matrix with the condition of 20 ns maximum time difference between coincidence $\gamma$ rays by the 170 keV and

220 keV transition an additional $\gamma$ line at 87 keV is observed. This extra $\gamma$ line is only visible in these spectra while it is not observed in the rest of the $\gamma\gamma$ coincidence analysis under this time condition, therefore it is not taken into account in the level scheme proposed (Figure 3.32). Additionally, the non observation of cross over transition between the competing branches depopulating the isomeric state will add difficulties to place the 87 keV $\gamma$ ray in the $^{126}$Cd decay pattern.

The deduced experimental level scheme of $^{126}$Cd is shown in Figure 3.32. The $2^+$ and $4^+$ states were known a priori to this work. In the work of Walters et al. [97], the 402 keV transition was assumed to decay from a $5^-$ state at 1869 keV excitation energy populating the $4^+$ state referred as following previous assignment carried out by Krautzsch et al. [99]. In Reference [99], however, no such assignment is performed, and it reports exclusively on $\gamma$ ray energies without entering in a possible spin/parity assignment of the states. From then on, as in Reference [94], the $5^-$ state at energy of 1868 keV is adopted from the work of Walters et al.[97]. In any of those publications, no experimental evidence which lead to the assignment of the spin and parity to that state are presented. In this analysis the 402 keV transition feeding the $4^+$ state at 1467 keV excitation energy is confirmed. However, even from the present experimental information which has higher statistics than previous work, unambiguous spin and parity assignment for the state at energy of 1869 keV could not be performed, yielding to $(5^-)$ or $(6^+)$ as most probable assignments. The B(E1;$5^- \rightarrow 4^+$) = 1.64(15)$\times10^{-5}$ W.u strength in $^{128}$Sn [29] or the B(E2;$10^+ \rightarrow 8^+$) = 0.38(1) W.u. strength in $^{130}$Sn [26] would correspond to 0.2 ns and 3.7 ns half-life for the 1869 keV state, respectively. In both cases the half-life value could have escaped observation under the long lived isomer at 4573 keV energy, therefore is not possible to conclude either $E1$ or $E2$ character for the 402 keV transition.

The conversion coefficients of the 252 keV, 170 keV and 83 keV transitions were not possible to be extracted, therefore different electromagnetic characters for the 252 keV transition were assumed in order to shed light to the spin and parity assignment to the intermediate level at 1952 keV excitation energy. Assuming $E1$ or $M1$ character for the 252 keV transition will lead to a second $(6^+)$ or $(5^-)$ state for the 1952 keV intermediate level which is not expected at so low energy. However $E2$ character for the 252 keV transition will lead to the 170 keV and the 83 keV transitions will have both $E1$ character or $M1$ character. If the 1869 keV state is a $I^\pi = (5^-)$, the cascade from the 2122 keV level to the 1869 keV state will follow $(7^-)\rightarrow(6^+)\rightarrow(5^-)$ sequence, on the other hand, if the 1869 keV state is a $I^\pi = (6^+)$ the sequence will be $(8^+)\rightarrow(7^-)\rightarrow(5^+)$. The 11(2) ns half-life belongs to the state at 1952 keV energy, the B(E1), B(M1) and B(E2) strenghts for the 83 keV transition are 3.3(3)$\times10^{-5}$ W.u., 1.5(2)$\times10^{-3}$ W.u. and 90(25) W.u., respectively. An $E2$ character for this transition is completely excluded while $E1$ or $M1$ are possible.

The 220 keV $\gamma$ ray is assumed to be either an $E1$ or $M1$ transition. An $E2$ character for this transition will lead to an isomeric half-life of 87(6) ns for the 2342 keV state when the B(E2;$10^+ \rightarrow 8^+$) = 0.156(11) W.u. of $^{126}$Sn is taken. Therefore $(8^+)$ spin and parity is assigned for the 2342 keV state fed by the 97 keV transition. Assuming as upper limit 18(1) ns for the half-life of the 2439 keV state, the B(E1) and B(M1) strength for the 97 keV is 1.37(4)$\times10^{-5}$ W.u. 6.67(21)$\times10^{-4}$ W.u., respectively. Both values are reasonable although the B(E1) seems a bit strong while the B(M1) is on

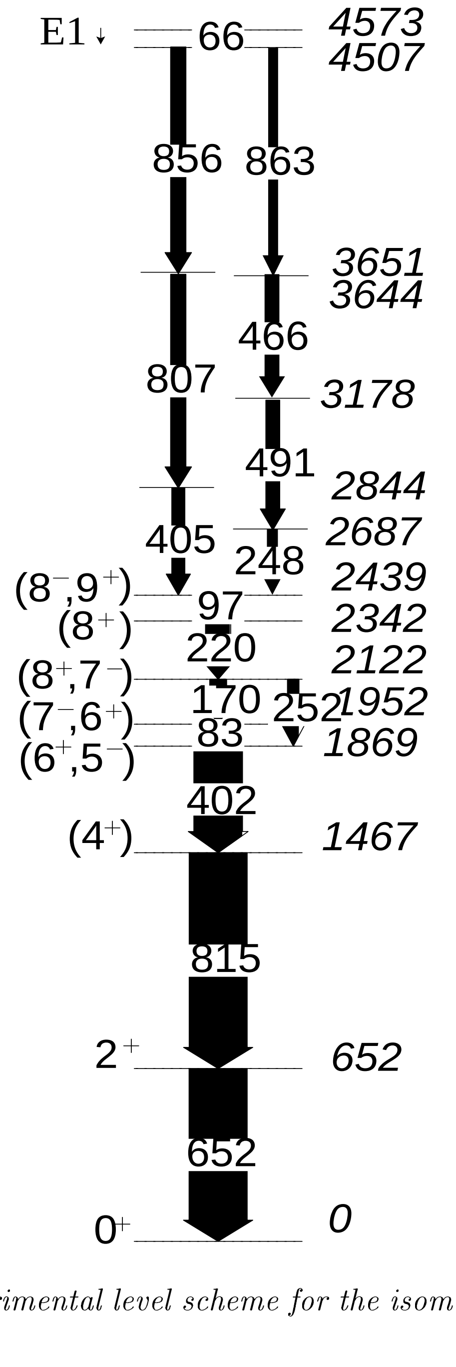


Figure 3.32: *Deduced experimental level scheme for the isomeric deexcitation of $^{126}$Cd.*

the weak side when compared to the strengths in the $^{132}$Sn region. As the 18(2) ns is an upper limit for the half-life and therefore a lower one it is expected thus the reduced transition probabilities strength will increase, the B(E1) strength will became too strong while the B(M1) will be closer to the typical values. Therefore an $M1$ character for the 97 keV transition is the most probable assignment.

There is no firm experimental evidence for the spin and parity assignment of the states between the 4507 keV and 2439 keV levels. Most probably, the two independent branches have different parity, although it can not be proved. The spins and parities shown in Figure 3.32 are tentative assignments among many other possibilities. The two cascades depopulate the level at 4507 keV excitation energy fed by the 66 keV $\gamma$ ray. The conversion coefficient of this transition was extracted as 0.51(47) in agreement with the theoretical $\alpha$(E1) = 0.53. It is concluded that the 66 keV transition has an $E1$ character, most probably depopulating the isomeric ($15^-$) state at 4573 keV excitation energy. The B(E1) strenght for this transition amounts to $3.55(21)\times10^{-7}$ W.u. comparable to the observed values in the $^{132}$Sn region.

## 3.4 The nucleus $^{131}$In

175000 $^{131}$In nuclei were identified in total in this experiment. From the energy versus time matrix, a single $\gamma$ ray at energy of 3782(1) keV in coincidence with the $^{131}$In isotopes was observed. The energy spectrum obtained once the prompt-flash contribution is removed is shown in Figure 3.33. The measured number of counts amounts to 176(10) counts, additional intensity associated to this transition was measured at 3271 keV energy when one of the 511 keV $\gamma$ rays from the pair production process escaped observation. The time distribution associated to the transition with respect to the ion implantation presented a single exponential decay curve, resulting in an isomeric half-life of 630(60) ns, as it is shown in the inset of Figure 3.33. No other $\gamma$ transitions were observed within the experimental sensitivity. The $\gamma$ ray energies versus an extrapolated transition intensity based on the experimental efficiency curve normalized to the number of counts in the 3782 keV transition is presented in Figure 3.34. The efficiency of a $\gamma$ ray energy lower than the observed 3782 keV will be considerably higher than the efficiency of the latter if the transition is not highly converted. The efficiency curves when $E1$, $M1$ and $E2$ multipolarities are taking into account is represented in Figure 3.34, as well. Assuming the same relative intensities for a low energy transition as for the 3782 keV the observational limit for an $E1$, $M1$ and $E2$ transition is 52 keV, 59 keV and 77 keV, respectively. In case that there is a non-observed primary transition following with the 3782 keV $\gamma$ decay, the reduced transition probability limits are $1.44\times10^{-6}$ W.u. $\leq$ B(E1) $\leq 2.78\times10^{-5}$ W.u., $3.81\times10^{-5}$ W.u. $\leq$ B(M1) $\leq 4.34\times10^{-4}$ W.u. and 1.70 W.u. $\leq$ B(E2) $\leq$ 8.56 W.u. when upper limit for the energy transition is taken from the observational limit and the lower limit is defined by the In $L$-binding (6 keV). The M1 character for the non-observed transition can be excluded as the retardation would be an order of magnitude higher that the observed $M1$ transitions between core excited states in $^{132}$Sn [38]. $E2$ character can not be completely excluded although the strength is stronger that i.e. the B(E2;$8^+ \rightarrow 6^+$)= 0.107(5) W.u. between states of the same multiplet in $^{132}$Sn [38]. Allowing $E1$ or $E2$ character for a non-observed isomeric low energy $\gamma$ transition in

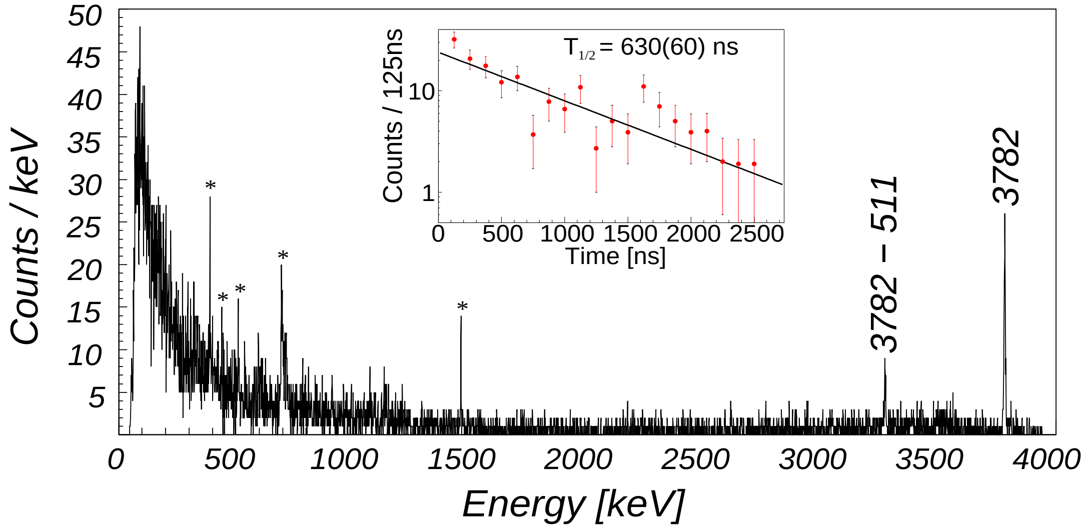


Figure 3.33: *Energy spectrum from the isomeric deexcitation of $^{131}$In. The onset shows the decay curve of the 3782 keV transition with respect to the ion implantation.*

cascade with a $\Delta$ $I$= 0 - 3 fast 3782 keV, the possible spin and parity assignments will be ($15/2^+$,$17/2^+$) and ($11/2^+$, $13/2^-$, $15/2^-$) for the isomer and intermediate state, respectively. However, a 3782 keV primary transition with 630(60) ns half-life is compatible to an $E4$ character yielding to a ($17/2^+$) spin and parity assignment to the isomeric state. The $E4$ strength of 1.48(14) W.u. is similar to those known in $^{132}$Sn and $^{98}$Cd, therefore the 3782 keV is assigned to the ground state decay from the ($17/2^+$) isomer. Any single $\gamma$ ray or cascade feeding the ($1/2^-$) isomer can be excluded due to fast competing branches from the isomer to the ground state or to the ($1/2^-$) state.

Additional argument supporting the assignment of the 3782 keV transition to the principal decay from the isomeric state is the following: the typical transition strength in this region of the nuclear chart are $10^{-7}$ W.u. for $E1$, $10^{-3}$ W.u. for $M1$ and 1 W.u. for $E2$ leading to a 89 $\mu$s half-life for a 52 keV transition, 2.4 ns for a 59 keV and 1.1 $\mu$s for a 77 keV. Based on the measured half-life non of these transitions are expected to populate the level at 3782 keV, and any other transition at higher energy would be visible in the energy spectrum, although a low energy $M1$ character transition can not be excluded from this argument.

The $9/2^+$ ground state [30, 101] in $^{131}$In is know from $\beta$-decay experiments and attributed to one proton hole in the $g_{9/2}$ orbital. The isomeric $1/2^+$ first excited state [30, 101] at 302 keV [31] energy has $p^{-1}_{1/2}$ configuration. A high spin isomeric decay was observed in Reference [30], and tentatively assigned to be ($21/2^+$) based on its feeding to the $19/2^{\pm}$ [30] and $23/2^+$ [31] states in the daughter $^{131}$Sn. The high spin isomeric state has been interpreted as belonging to the $\pi g^{-1}_{9/2} \nu h^{-1}_{11/2} f_{7/2}$ multiplet [30] based on the fact that no proton state configuration could explain the observation of such an isomer. In the present work, the $I^\pi$ for the core excited isomeric state is assigned to be ($17/2^+$) if no other transition contribute in the decay. This state lies above the ($21/2^+$) at 3764(88) keV, and its $E4$ strength of 1.48(14) W.u. can be consider as an upper limit if a non-observed $E2$ transition to ($21/2^+$) is taken into account. Both

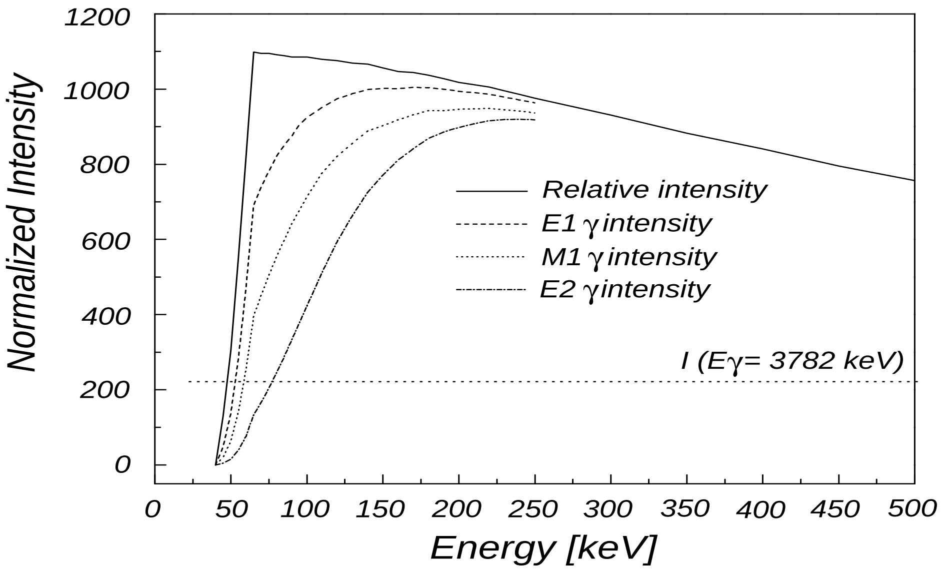


Figure 3.34: *$\gamma$ ray energies versus an extrapolated transition intensity based on the experimental efficiency curve normalized to the number of counts in the 3782 keV transition. The observation limits for a low energy transitions is indicated by an horizontal line.*

states belong to the $\pi\ g_{9/2}^{-1}\nu\ h_{11/2}^{-1}f_{7/2}$ multiplet. Further arguments based on LSSM calculations for the spin and parity assignment of the isomeric state reported in this work will be presented in the next chapter.

This results will be reported in a forthcoming publication by Górska et al. [102]

# Chapter 4

# Discussion

In this chapter the experimental results previously shown will be discussed in terms of LSSM calculations. In the first section the question whether there is $N = 82$ shell quenching below $^{132}$Sn will be answered based on the comparison between the experimentally extracted level schemes of $^{131}$In and $^{130}$Cd and the calculations. The discussion will continue with the consequences of the new results for the r-process. The information concerning the $^{130}$Cd decay pattern will be compared to its analogue nuclei, $^{98}$Cd and $^{78}$Ni, in Section 6.3. The comparison of $^{126}$Cd and $^{128}$Cd level schemes to the LSSM calculations provides information on the $\pi$-$\nu$ interaction and will be discussed in Section 6.4.

## 4.1 N = 82 Shell Quenching

In order to answer the question whether the *N=82* shell quenching exists "south" of $^{132}$Sn at *Z=48*, the level schemes of $^{130}$Cd and $^{131}$In were compared to large scale shell model calculations.

The experimental level scheme of $^{130}$Cd was compared to two different LSSM calculations [95], which will be referred to as SM-1 and SM-2. The SM-1 calculations were performed by G. Martínez-Pinedo, F. Nowacki, A. Poves and K. Langanke while the results from the SM-2 were provided by H. Grawe. Both are based on a $^{88}$Sr core. The G-matrices were derived for different model spaces from the CD-Bonn nucleon-nucleon potential [103] following the method presented in Reference [104]. The model space $p_{1/2}$, $s$, $d$, $g$ and $g_{7/2}$, $s$, $d$, $h_{11/2}$ for protons and neutrons, respectively, was used in SM-1. The selection of this a model space implies that proton excitations across the *Z=50* shell gap are included while excitations across the *N=82* closed neutron shell where not taken into account in the calculations. The monopole component of the nuclear interaction was tuned to experimental data between *N=50* and *N=82* [105] to reproduce the single-particle/ -hole energies in $^{132}$Sn [6, 32]. The calculations were performed with the code ANTOINE [14]. This interaction was found to reproduce the $^{100}$Sn core excitations in the *A=102-130* tin isotopes [106] and to predict the $\beta$ half-life for the *N=82* isotones [107]. Details of the single-particle energies and effective operators used in these calculations are given in References [106, 107, 108]. The SM-2 calculations uses as model space the orbitals $p_{1/2}, g_{9/2}$ for protons and $g_{7/2}$, $s$, $d$, $h_{11/2}$ for neutrons. Consequently in these calculations neither proton nor neutron excitations

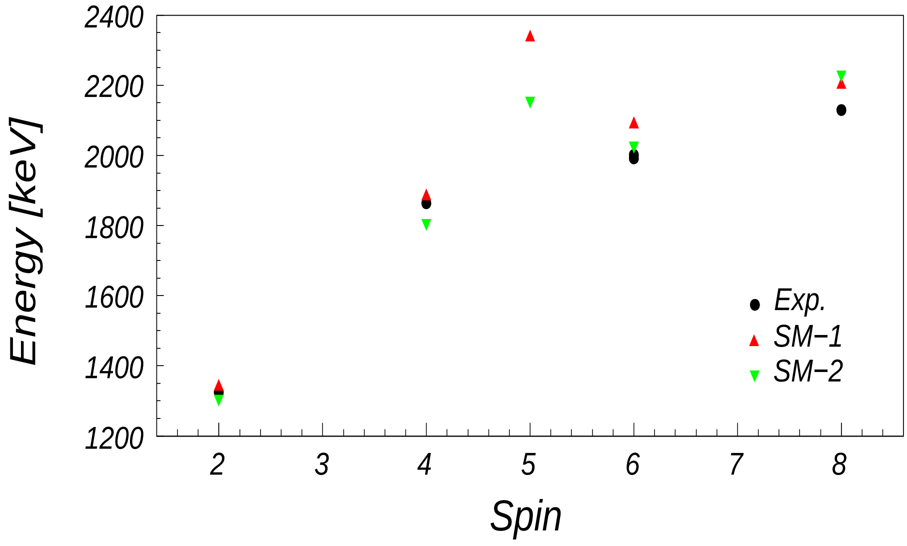


Figure 4.1: *The experimental $^{130}$Cd level scheme is compared to two different shell model calculations. A remarkable similarity between the experimental excitation energies for the states populated in the isomeric decay of $^{130}$Cd and the calculated values is found.*

across the shell gaps were considered. Monopole corrections were applied to describe the evolution of the single particle energies for $^{88}$Sr to $\pi$-hole and $\nu$-particle in $^{100}$Sn [6, 32]. The interaction reproduces high spin states and Gamow-Teller decays in the $^{100}$Sn region [109]. For the $^{132}$Sn region, a $A^{-1/3}$ scaling of the TBMEs was performed and the monopole was tuned to reproduce the single-particle energies in $^{132}$Sn [6, 32]. These calculations were performed with the OXBASH code [110].

The results of both calculations compared to the experimental data are shown in Figure 4.1 clearly exhibiting a remarkable agreement. The calculated $5^-$ state formed by the excitation of one proton from the $p_{1/2}$ to the $g_{9/2}$ orbital is not observed experimentally. The effective charges used in both calculations to calculate the E2 transition strengths were $1.5e$ and $0.5e$ for protons and neutrons, respectively. The calculated B(E2;$8^+ \rightarrow 6^+$) strength was 1.5 W.u. for SM-1 and 1.2 W.u. for SM-2. Both values agree with the experimental E2 strength of 1.11(25) W.u. when the 128 keV transition is considered as decaying from the isomeric state and 0.83(18) W.u. when the 138 keV $\gamma$ ray is assumed to be the $8^+ \rightarrow 6^+$ transition. In both shell model calculations the shell gap was considered the same as in $^{132}$Sn, therefore no quenching was assumed. It is clear that both LSSM calculations are able to describe the nuclear structure of $^{130}$Cd, concluding that the experimental results for the $^{130}$Cd isomeric deexcitation do not present any evidence for shell quenching. Additionally, calculations were performed reducing the size of the $N = 82$ shell gap showing that the isomerism of the $8^+$ state was kept. This observation follows with the conclusion that the decay pattern of $^{130}$Cd is an indirect measurement of the shell gap.

A direct measurement of the gap is obtained by studying the deexcitation of the core excited isomeric state in $^{131}$In [102]. The $^{131}$In decay pattern was compared to LSSM calculations performed by Grawe [102] based on a $^{132}$Sn core and experimental particle(hole) energies [32]. The model space used was $\pi(p_{1/2}, g_{9/2}, g_{7/2}, d_{5/2})$ for protons and $\nu(s_{1/2}, h_{11/2}, d_{3/2}, f_{7/2}, h_{9/2})$ for neutrons. The TBME of the residual interaction were inferred from $^{208}$Pd [111], one harmonic oscillator shell higher, replacing single particle orbits $(n, l, j)$ by $(n, l-1, j-1)$ which maintains the proper radial wave functions following the prescription given in Reference [112]. The interaction was mass scaled ($A^{-1/3}$) and for the intermediate spins in a multiplet interpolated according to their angular orbital overlap [6]. The calculations were performed using the OXBASH [110] code. Only 1p1h (one proton one hole) excitations (t=1) of the valence configuration were considered. Since the t=1 truncation has a stronger effect on the lower spins in a multiplet than on the stretched states, a modification of -200 keV, -200 keV, 200 keV and -250 keV of the ph TBME for the $4^+$, $6^+$ and $9^+$ states of the $\nu h^{-1}_{11/2} f_{7/2}$ configuration and for the $3^-$ state of the $\nu d^{-1}_{3/2} f_{7/2}$ was performed in order to obtain better agreement with the experimental $^{132}$Sn level scheme. Additionally, the monopoles for the $\nu h^{-1}_{11/2} f_{7/2}$, $\nu d^{-1}_{3/2} f_{7/2}$ and $\pi g^{-1}_{9/2} g_{7/2}$ multiplets were tuned to reproduce the corresponding unambiguously identified members of the multiplets in $^{132}$Sn. Effective charges of $1.5e$ [95] and $0.7e$ [113] for protons and neutrons, respectively, were used to calculate the $E2$ and $E4$ transition strengths. The results of this calculation in comparison to the experimental level schemes of $^{131}$In and $^{132}$Sn are shown in Figure 4.2. The $2^+$, $4^+$ and $3^-$ states in $^{132}$Sn are not reproduced due to their collective character which is not accounted for in the model space due to the truncation. The stretched $9^+$ agrees well with the experimental excitation energy. Therefore it is concluded that the discrepancy between calculation and experimental results arises from the truncation while the interaction is considered reliable. The shell model calculations for $^{131}$In supports the spin and parity proposed in present [102] and previously measured $21/2^+$ in [30]. The calculated strength of B(E4; $17/2^+ \rightarrow 9/2^+$) = 2.4 W.u. compares well with the experimental upper limit of 1.6 W.u. which takes into account a possible non-observed $E2$ branch to the $(21/2^+)$ isomer. With the shell model prediction of B(E2;$17/2^+ \rightarrow 21/2^+$) = 0.29 W.u. a branch of $\leq 17$ % is calculated for an upper observational limit of 77 keV. Since the isomeric states in $^{132}$Sn with $\pi(g_{9/2})^{-1}$ $\nu h^{-1}_{11/2} f_{7/2}$ configuration are not coupled to maximum spin, their excitation energies due to residual interaction and truncation are not a quantitative measure of the $N = 82$ shell gap, instead the stretched $9^+$ is a good candidate. In view of the agreement for core excited states in $^{132}$Sn and $^{131}$In, Grawe calculated the shell gap for $^{130}$Cd from the difference in binding energies between the $N = 81 - 83$ Cd isotopes. The results show a reduction of the $N = 82$ shell gap of 0.61 MeV, from 4.94 MeV in $^{132}$Sn to 4.33 MeV in $^{130}$Cd. This reduction is of the same order that the reduction of the $Z = 50$ gap from $N = 82$ to 80 [114] of 0.680 MeV.

Based on these results for $^{131}$In and $^{130}$Cd, it is concluded that there is no $N = 82$ shell quenching at $Z = 48$ and that the reduction of the shell gap can be explained as an effect caused by the monopole component of the nuclear interaction. Therefore, all the mass models based on a $N = 82$ shell quenching should be reviewed as well as the r-process solar abundance calculations in which they are used. The question where the $N = 82$ shell quenching sets in will be answered with the study of lighter systems towards $^{122}$Zr, although those nuclei are still out of reach experimentally.

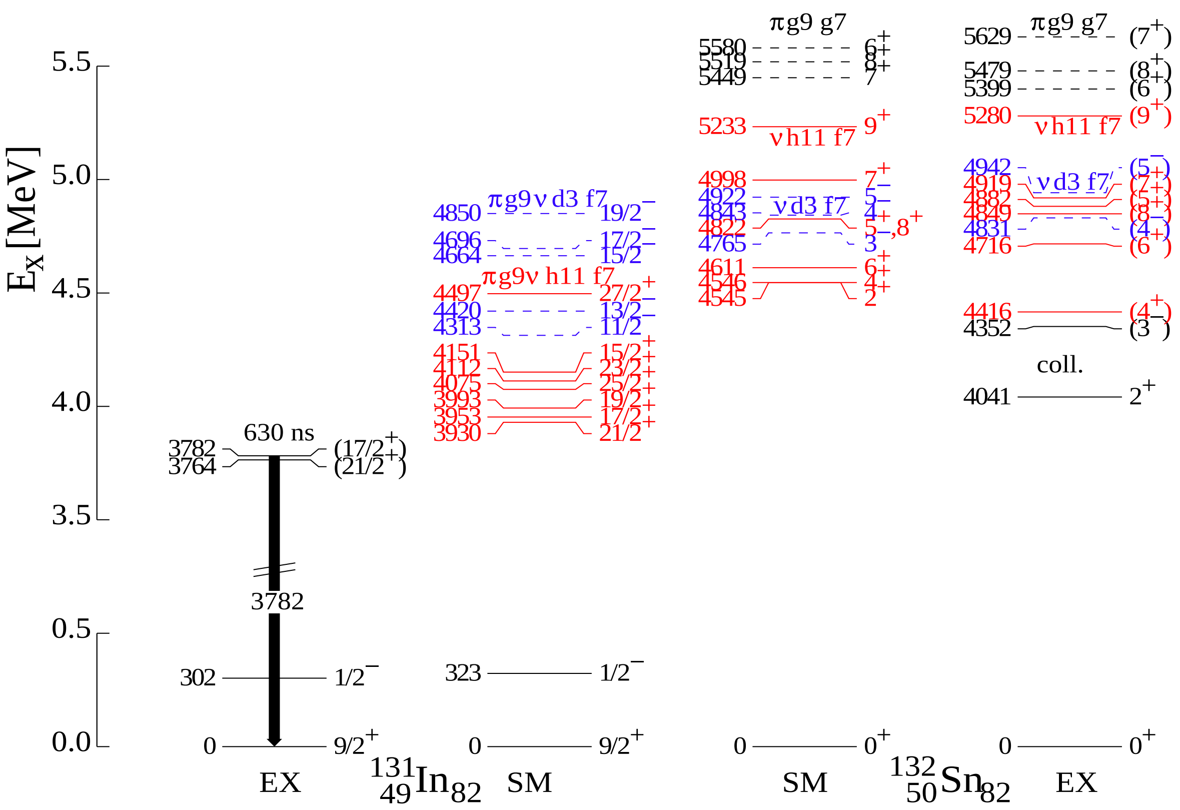


Figure 4.2: *LSSM calculations compared to the experimentally deduced $^{131}In$ and $^{132}Sn$ level schemes. The colored states are labeled accordingly to their configuration; red-full line is the $\nu h^{-1}_{11/2} f_{7/2}$ multiplet, blue-short dashed line is the $\nu d^{-1}_{3/2} f_{7/2}$ configuration and black-long dashed line is the $\pi g^{-1}_{9/2} g_{7/2}$ multiplet.*

### 4.1.1 Astrophysical implications

The decay patterns in $^{130}$Cd and $^{131}$In showed that there is no evidence for any $N = 82$ shell quenching below $^{132}$Sn up to $Z = 48$ and that the 0.61 MeV reduction of the gap could be explained by the monopole migration of the single particle states. The question concerning the solar models is which is the parameter to be modified in order to reproduce the solar r-process abundances and to fill the troughts at $A \simeq 115$ and $A \simeq 175$ closely related to the $N = 82$ and $N = 126$ neutron shell closures.

Recent observations of the r-process abundances of nuclides with $Z > 56$ in old stars lead to the conclusion that the production of nuclides with $Z > 56$ occurs always under similar astrophysical conditions, or that the abundance pattern is independent of these conditions [115] probably because very extreme conditions are reached. As possible explanation for this conditions could be the fission cycle.

As described in Reference [32], the fission during the r-process will start to play a role when the theoretical $N = 184$ magic number is reached. At that moment, the different fission processes that a nucleus may undergo are: spontaneous, neutron-induced fission, beta-delayed, and if the r-process occurs under strong neutrino fluxes, neutrino-induced fission. Considering properly the fission yields and rates, the abundances at intermediate masses will increase due to the fission fragments from heavier masses. Additionally, the neutrons emitted during the fission process will contribute to the continuation of the r-process.

The current solar abundance models include only a simplistic description of the fission process, although a development in this direction started including a full set of fission rates in the calculations ([32] and reference therein). As it is considered in the models, neutron-induced fission starts when the $N = 184$ magic number has been overcome and continuous until all the neutrons are consumed. This process is followed then by beta-delayed fission, which liberates new neutrons that can induce new fission reactions. However if in the r-process models shell quenching is assumed, the nuclei above $N = 82$ are stronger produced. Those neutron rich nuclei exhaust all the available neutrons for fission of heavier nuclei. On the other hand, in the models which consider a strong shell gap more neutrons are left in the process that could induce fission because only a small amount of matter passes through the $N = 82$ and $N = 126$ shell gaps. Once this matter reaches the $N = 184$ shell closure, neutron induced fission of these nuclei starts producing fission fragments at $A = 130 - 190$ and consequently filling the troughts at $A \simeq 115$ and $A \simeq 175$.

## 4.2 Empirical j$^2$ two-body interaction

The isomeric decay of $^{130}$Cd can be compared to its analogue nuclei, $^{76}$Ni and $^{98}$Cd, two neutron and two proton holes in the $g_{9/2}$ orbital, respectively. Their excited states have a pure $(g_{9/2})^{-2}$ configuration, within the simple shell model approach, while the ground state is mixed with the $p_{1/2}$ orbit. This set of three nuclei allows to extract for the first time empirical $j^2$ TBME, for protons and neutrons in the $g_{9/2}$ orbital.

In the shell model approach the radial dependence of the wave function is implicit in the SPE and the TBME [119]. It is common to use the same set of SPE and TBME over a mass range covered by the model space with a scaling of the two body matrix elements.

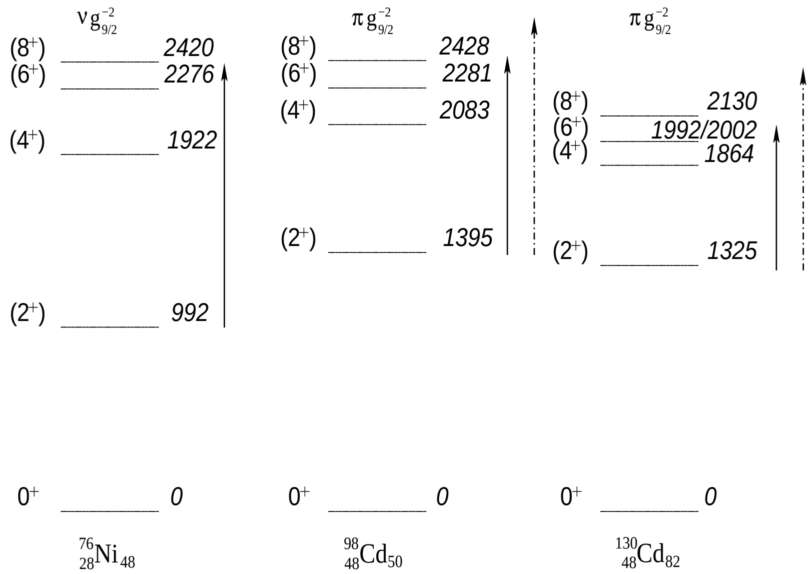


Figure 4.3: *Comparison of the $^{78}$Ni (left), $^{98}$Cd (middle), $^{130}$Cd (right) level schemes. The solid arrows represent the scaling of the TBME assuming a $A^{-1}$ scaling while the dashed arrows represent the scaling when the well establish empirical law $A^{-1/3}$ is used.*

Depending on the potential chosen to calculate the TBME and SPE, the scaling factor will vary accordingly, i.e. $A^{-1/3}$ dependence for a harmonic oscillator and $A^{-1/2}$ in the case of a delta function. This scaling factor accounts for the change of the radial component of the wave function with the mass number. As interesting observation by Grawe [95], the TBME when going from $^{76}$Ni towards $^{130}$Cd passing through $^{98}$Cd scales with $A^{-1}$ instead of the "well established empirical law" $A^{-1/3}$ as it is shown in Figure 4.3 by the solid and dashed arrows, respectively. This result could not be attributed as a Coulomb shifts as they are essentially constant for $I \neq 0$ in this specific model space [10]. If the model space is extended, including excitations across the shell gaps, the $8^+$-$2^+$ $(g_{9/2})^{-2}$ spread from $^{76}$Ni to $^{130}$Cd could be explained as being a consequence of the excitations across the $Z = 28$ closed shell for $^{76}$Ni, across the $N = 50$ closed shell for $^{98}$Cd and the $N = 82$ closed shell for $^{130}$Cd. This concept is understood as follows: in first approximation the $8^+$-$2^+$ spread can be estimated considering only the quadrupole part of the residual interaction which scales as $\mathrm{E}_q \sim \mathrm{m}^2/(\mathrm{D}\cdot\mathrm{A}^{1/3})$ [14], where $m$ is the number of particles at the Fermi level and $D$ is the degeneracy of the shell. In the case of neutron excitations across the $N = 50$ gap in the case of $^{76}$Ni and proton excitation across the $Z = 50$ shell closure for $^{98}$Cd and $^{130}$Cd, $D$ and $m$ are the same in all three nuclei. The situation changes when the excitations across the proton and the neutron shell gaps in the case of $^{76}$Ni and $^{98}$Cd, $^{130}$Cd, respectively, are included. In this case $D$ and $m$ are different leading to a observation of the deviation from the $A^{-1/3}$ scaling factor towards $A^{-1}$.

## 4.3 Proton-Neutron interaction in neutron rich nuclei

The experimental data associated to the isomeric decay in $^{128}$Cd were compared to the results of large scale shell-model (LSSM) calculations performed by Sieja et al. [118] us-

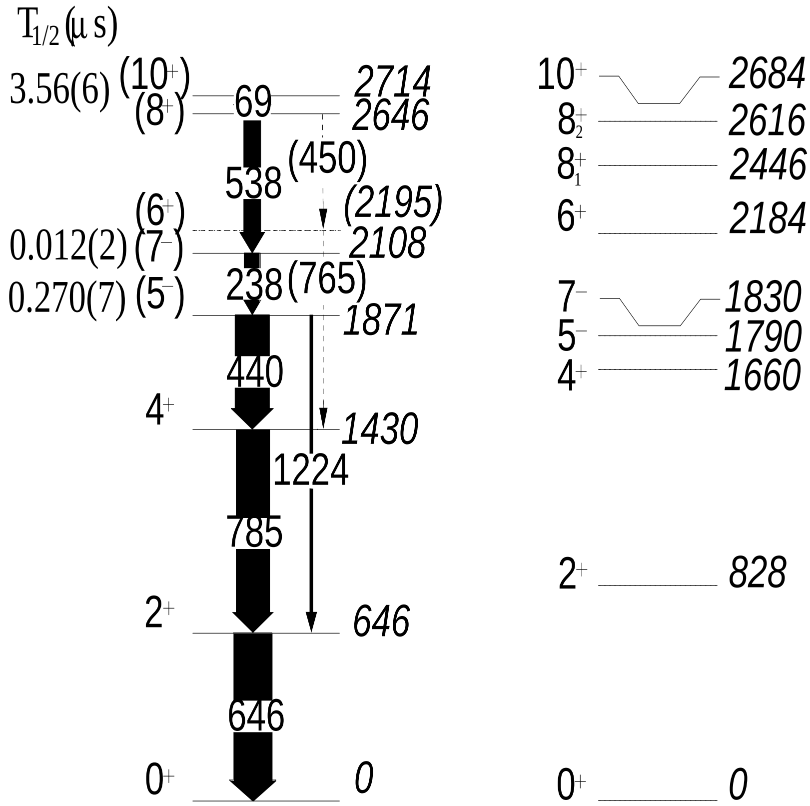


Figure 4.4: *Comparison of the deduced experimental level scheme for the isomeric deexcitation of $^{128}$Cd (left) with shell model calculations (right).*

ing a model space based on a $^{78}$Ni core and comprising the proton $\pi(p_{3/2}, p_{1/2}, f_{5/2}, g_{9/2})$ and neutron $\nu(g_{7/2}, s_{1/2}, d_{5/2}, d_{3/2}, h_{11/2})$ orbitals. The effective interaction was derived from the CD-Bonn nucleon-nucleon potential [116] using G-matrix theory and adapted to the model space using many-body perturbation techniques [117]. Monopole corrections were applied in order to reproduce correctly the excitation energies of the neutron rich nuclei below $^{132}$Sn [38]. In particular, the evolution of the $1/2^-$ and $9/2^+$ proton doublet along the Indium chain as well as the neutron level schemes along the Tin chain were reproduced. The calculations were performed with the code ANTOINE [14]. Electromagnetic transition rates were calculated with the standard polarization charge of 0.5 $e$ for both protons and neutrons.

In Fig. 4.4 the experimental level scheme is compared to the LSSM calculations. The overall agreement between theory and experiment is satisfying in view of the fact that the spectrum is *a priori* rather complex with the coexistence of proton and neutron states. In particular, the high lying $8_2^+$ and $10^+$ states have predominant $h_{11/2}^{-2}$ neutron character (cf. $^{130}$Sn) and are correctly located with respect to the $0^+ - 8_1^+$ $g_{9/2}^{-2}$ and $4^-, 5^-$, $g_{9/2}^{-1}p_{1/2}^{-1}$ proton multiplets (cf. $^{130}$Cd). The shift in the excitation energies of the $2^+$ and $4^+$ states reveals the ground-state sensitivity to the mixing between the $\pi g_{9/2}$ and $\pi p_{1/2}$ proton configuration. An additional binding energy added to the $p_{1/2}$ single particle orbital would reduce the mixing and bring the results in agreement for the $2^+$ and $4^+$ states, however at the cost of spoiling the location of the $5^-$ level. The latter with a predominant $\pi g_{9/2}^{-1}p_{1/2}^{-1}$ proton configuration (59 %) is well reproduced in the calculation, whereas a slight discrepancy concerns the $7^-$ level dominated by the $(d_{3/2})^{-1}(h_{11/2})^{-1}$ neutron configuration which can be possibly traced back to the $\pi g_{9/2}\nu d_{3/2}$ monopole. The $6^+$ has a mixed configuration proton-neutron wave function, which explains why it is populated from the neutron $8_2^+$ and lies well below the unpopulated proton $8_1^+$ state (see below). Excellent agreement is however found for the energy of the isomeric $10^+$ state. It appears to be formed mainly (86 %) by the two maximum aligned neutron holes in the $h_{11/2}$ orbital and decays by an $E2$ transition to the $8_2^+$ state dominated as well by the two-neutron hole configuration. The calculated $8_1^+$ state at energy of 2446 keV is found to have a pronounced (64 %) proton component which explains why it is not populated in the isomeric decay of the neutron $10^+$. The $E2$ theoretical transition rates of $B(E2;10^+ \rightarrow 8_2^+) = 0.59$ W.u. and $B(E2;7^- \rightarrow 5^-) = 0.83$ W.u. agree well with experiment measured values 0.39(1) W.u. and 1.5(3) W.u., respectively. The $B(E2;10^+ \rightarrow 8_1^+) = 0.15$ W.u. though smaller by a factor of four compared to the transition to the $8_2^+$ matches non-observation only if the two $8^+$ states are close in energy.

Based on these calculations, the lowering of the $2^+$ energy could be explained as an effect caused by the mixing of the $g_{9/2}$ and $p_{1/2}$ proton orbitals. However, the discrepancy of energy levels at intermediate spin reveals the need for a further revision of the interaction which could be achieved by minor monopole correction in those multiplets that are experimentally not well determined near the $N = 50$. The experimental data indicate that the isomeric decay pattern is selective to the structure of the populated states and their leading $\pi$ or $\nu$ configuration. This conclusion is further supported by a comparison to LSSM calculations which yields an overall good agreement and additionally strengthens the spin and parity assignments.

Detail spectroscopy in the $^{132}$Sn region is not the aim of the present interaction which is still in the course of being developed, although it is interesting to compare the LSSM calculation with the same interaction as the one used for the $^{128}$Cd with the experimental level scheme in $^{126}$Cd (Figure 4.5). It is observed that a low spin there is an overall good agreement between both the experimental results and the calculations. As in the case of $^{128}$Cd the $2^+$ and $4^+$ states are shift up in energy while the $5^-$ is only 60 keV off. The latter state is very mixed being difficult from the calculation to determined the most probable configuration. The $6^+$ and $7^-$ are reversed in energy, this is probably consequence of the $\pi g_{9/2}\nu d_{3/2}$ monopole which might have to be modified as mentioned above. In $^{126}$Cd there is two neutron-holes more than in $^{128}$Cd causing that the $d_{3/2}$ orbital is less bound and therefore it shifts up in energy and with it the $7^-$. The $8^+$ state has $\sim$69 % neutron component. The high level density and the experimental uncertainties made difficult to extract any further conclusion on the structure of the states above the 2342 keV level.

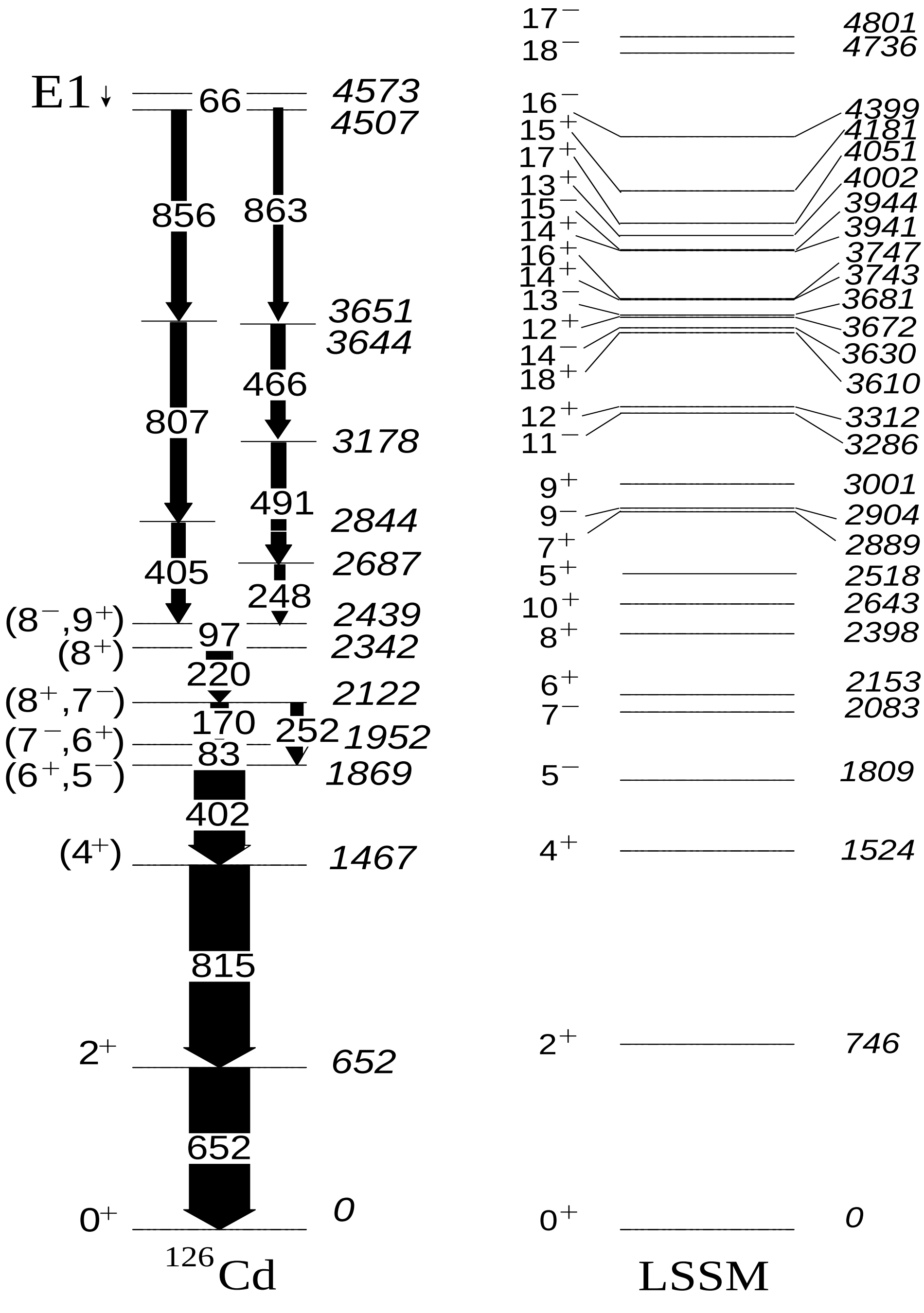


Figure 4.5: *Comparison of the deduced experimental level scheme for the isomeric deexcitation of* $^{126}$*Cd (left) with shell model calculations (right).*

# Chapter 5

# Summary

- The decay pattern associated to the deexcitation of an isomeric state in $^{130}$Cd has been established for the first time. This nucleus is the only waiting-point nucleus for which information concerning excited states is available. Four $\gamma$ transitions with energies of 128 keV, 138 keV, 539 keV and 1325 keV have been reported and the $\gamma\gamma$ coincidence analysis revealed that all of them form a single cascade. The fit of their time distributions with a single exponential decay function yields a half-life of 235(53) ns for the isomeric state at 2130 keV excitation energy. The $(8^+)$ isomeric state in $^{130}$Cd is formed by the maximally aligned two proton holes in the $(g_{9/2})$ orbit as expected in analogy to the $8^+$ isomer observed in $^{98}$Cd. The remarkable agreement between the experimental level scheme and LSSM calculations reveal that there is no evidence of a $N = 82$ shell quenching at $Z = 48$.

- A direct measurement of the shell gap was obtained by studying the decay of a core-excited isomer in $^{131}$In. A single $\gamma$ ray of 3782 keV has been measured, and additional counts were observed at 3271 keV when one of the electrons from the pair production process escaped observation. No additional low energy transition was observed in coincidence with the 3782 keV $\gamma$ ray leading to the conclusion that the $(17/2^+)$ isomer decays by an E4 3782 keV transition to the $9/2^+$ ground state. The comparison of the experimental results to LSSM calculations reveal a reduction of the $N = 82$ shell gap of $\sim 600$ keV in $^{130}$Cd. This effect is understood as being a consequence of the monopole migration and not provoked by the excess of neutrons.

- Up to date, the r-process models which considered shell quenching in the calculations were able to agree well with the observed solar abundances, i.e. filling the troughts at $A \simeq 115$ and $A \simeq 175$. The prove of the no $N = 82$ shell quenching at $Z = 48$ lead to the question which is the parameter to be modified in order to reproduce the solar r-process abundances. The fission reaction may play an important role in the r-process mechanism and could be the solution for the r-process puzzle [32].

- The comparison of the level schemes of $^{76}$Ni, $^{98}$Cd and $^{130}$Cd allow to extract for the first time empirical $j^2$ TBME for protons and neutrons in the $g_{9/2}$ orbital.

Additionally, the $8^+ \rightarrow 2^+$ energy spread scales with $A^{-1}$ instead of the well established empirical law $A^{-1/3}$. This effect is caused by the different shell degeneracy and number of particles at the Fermi level when excitations across the $Z = 28$ proton gap in $^{76}$Ni and neutron excitations across $N = 82$ shell gap in $^{98}$Cd and $^{130}$Cd are considered.

- The level scheme associated to the isomeric decays in $^{128}$Cd has been unambiguouly constructed based on the $\gamma\gamma$ coincidence and lifetime analysis performed for the first time in the present work. Previously reported transitions were confirmed and additional weak $\gamma$ lines of $\sim 1\%$ of the intensity of the main cascade have been observed for the first time. The half-lives of three isomeric states at 1871 keV, 2108 keV and 2714 keV excitation energy were measured yielding to 0.269(7) $\mu$s, 0.012(2) $\mu$s, and 3.56(6) $\mu$s, respectively. The experimental data indicate that the decay pattern is selective to the structure of the populated states and their $\pi$ or $\nu$ configurations. This conclusion is further supported by the comparison to LSSM calculations which yields an overall good agreement and additionally strengthens the spin and parity assignments. However the observed discrepancy for the theoretical excitation energies at intermediate spins reveals a need for a further revision of the interaction which could be achieved by minor monopole corrections in those multiplets that are experimentally not well determined near the $N = 50$. Detailed spectroscopy in the $^{132}$Sn region is however not the aim of the presently used interaction which still is in the course of being developed [118].

- High spin states associated to the isomeric decay in $^{126}$Cd have been observed. The transitions previously reported were confirmed and in addition the $\gamma$-$\gamma$ coincidences in conjuction with detailed half-life analysis performed for the first time in this nucleus allowed to construct the level scheme. The isomeric state at 4573 keV excitation energy with 1710(70) ns half-life decay by an E1 66 keV transition to the 4507 keV level which is depopulated by two competing branches to the 2439 keV state. The no observation of linking transitions between the two branches made imposible the ordering of the $\gamma$ rays within the two independent cascades. The results have been compare with LSSM calculations being an overall good agreement at low excitation energy. The $6^+$ and $7^-$ states are reversed in energy in the calculations with respect to the experimental level scheme, this could be caused by the $\pi g_{9/2}\nu d_{3/2}$ monopole. In $^{126}$Cd there is two neutron-holes more than in $^{128}$Cd causing that the $d_{3/2}$ orbital is less bound and therefore it shifts up in energy and with it the $7^-$, therefore that monopole TBME most probably has to be modified in the calculations. The high level density above the 2439 keV state and the experimental uncertainities made any possible interpretaion in terms of LSSM calculations difficult.

# Resumen

- El patrón de decaimiento asociado a la deexcitación del estado isomérico en $^{130}$Cd ha sido establecido por primera vez. Este núcleo es el primer núcleo de punto de espera ("*waiting point nucleus*") por el que la información concerniente a los estados excitados está disponible. Se han reportado cuatro transiciones $\gamma$ con energías de 128 keV, 138 keV, 539 keV y 1325 keV y el análisis de coincidencia $\gamma\gamma$ reveló que todas ellas forman una cascada simple. El ajuste de la distribución los tiempos de cada transición con una función de decaimiento exponencial simple dió como resultado una vida media de 235(53) ns para el estado isomérico a la energía de excitación de 2130 keV. El estado isomérico $8^+$ en $^{130}$Cd está formado por el acoplamiento totalmente alineado de los dos huecos protónicos en el orbital $g_{9/2}$ como estaba esperado en analogía con el isómero $8^+$ observado en $^{98}$Cd. La concordancia entre el esquema de niveles experimental y los resultados de los cálculos LSSM revelaron que no existe evidencia de la disminución del tamaño de la capa $N = 82$ a $Z = 48$.

- Una medida directa del "shell gap" se obtiene mediante el estudio del decaimiento del isoméro de core-exited en $^{131}$In. Un único rayo $\gamma$ a energía de 3782 keV fué observado y cuentas adicionales se encontraron a 3271 keV causados por el no haber detectado uno de los electrones del la producción de pares. El hecho de que no se observasen otras transiciones a más baja energía llevó a la conclusión de que el isómero tiene espín y paridad $(17/2^+)$ y decae mediante una transición E4 de 3782 keV al estado fundamental $9/2^+$. La comparación de los resultados experimentales con los cálculos LSSM revelaron que el "shell gap" se redujo $\sim$600 keV en $^{130}$Cd. Este efecto es entendido como una consecuencia de la migración monopolo y nos es causado por el exceso de neutrones.

- Hasta la fecha, algunos modelos r-proceso que consideraban la disminución de la capa N=82 eran capaces de reproducir las abundancias solares, a saber, el relleno de los huecos a A$\simeq$115 y A$\simeq$175. Los resultados presentados en esta tesis demuestran que no hay evidencias que demuestren la disminución de la capa. La reacción de fisión puede ser la respuesta al puzzle del r-proceso [32].

- La comparación de los niveles de energía en $^{76}$Ni, $^{98}$Cd y $^{130}$Cd permite extraer por primera vez los TBME empíricos para protones y neutrones en el orbital $g_{9/2}$. Adicionalmente, la difusión de la energía entre el estado $8^+$ y el $2^+$ entre estos tres núcleos escala con $A^{-1}$ en lugar de las bien establecida ley empírica $A^{-1/3}$. Este efecto es causado por las diferencias en la degeneración de la capa y por el número de partículas en el nivel de Fermi cuando se consideran excitaciones a través del Z=28 gap en $^{76}$Ni y excitaciones a través del N=82 gap en $^{98}$Cd y $^{130}$Cd.

- El nivel de energías asociado al decaimiento de tres isoméros distintos en $^{128}$Cd ha sido construido basado en las coincidencias $\gamma - \gamma$ y el análisis de las vidas medias realizados por primera vez en este núcleo. Se confirman las transiciones reportadas con anterioridad y además otras transiciones débiles de ∼1% de intensidad de la cascada principal fueron observadas por primera vez. Las semividas de los tres isómeros a energías de 1871 keV, 2108 keV y 2714 keV son 0.269(7) $\mu$s, 0.012(2) $\mu$s y 3.56(6) $\mu$s respectivamente. Los datos experimentales indican que el patrón de decaimiento es selectivo a la estructura de los estados populados y su configuración $\pi$ o $\nu$. Esta conclusión es avalada por la comparación del esquema de niveles con los cálculos LSSM los cuales están en general de acuerdo con los resultados experimentales, aunque se observa pequeñas variaciones a espines intermedios lo cual demuestra que la interacción ha de ser revisada. La modificación de la interacción podría ser la corrección de aquellos multipolos que no estén bien determinados experimentalmente cerca de N=50. Sin embargo, la espectroscopía detallada en la región del núcleo $^{132}$Sn no es el objetivo principal de la interacción que continua en desarrollo.

- Se han observado los estados a alto espín populados en el decaimiento del estado isomérico en $^{126}$Cd. Las transiciones mencionadas en anteriores publicaciones fueron confirmadas y además el análisis de las coincidencias $\gamma$ en conjunto con un estudio detallado de las vidas medias realizados por primera vez en este núcleo sirvieron para construir el esquema de niveles. El estado isomérico a energía de 4573 keV y con una vida media de 1710(70) ns decae mediante una transición de carácter E1 de 66 keV al estado 4507 keV, el cual es depopulado por dos diferentes ramas que compiten. No se observaron transiciones que comunicaran dichas ramas por lo que la ordenación de los rayos $\gamma$ que componen las cascadas independientes no fue posible de realizar. Los resultados se han comparado con los cálculos LSSM observándose un buen acuerdo a bajas energías de excitación con la excepción de los estados $6^+$ y $7^-$ que se encentran invertidos en energía. Este hecho podría ser explicado por la necesidad de modificar el monopolo TBME $\pi g_{9/2} \nu d_{3/2}$, ya que $^{126}$Cd tienen dos huecos neutrónicos más que en $^{128}$Cd por lo que el orbital $d_{3/2}$ está menos ligado y se encuentra a mas alta energía así como el estado $7^-$. La gran densidad de niveles por encima del estado a 2439 keV y las incertidumbres experimentales dificultan la interpretación de las estructura nuclear de los niveles comprendidos entre ese estado y el isomérico.

# Apendix A: Additional coincidence energy spectra gated by the $\gamma$ transitions observed in the $^{126}$Cd isomeric decay

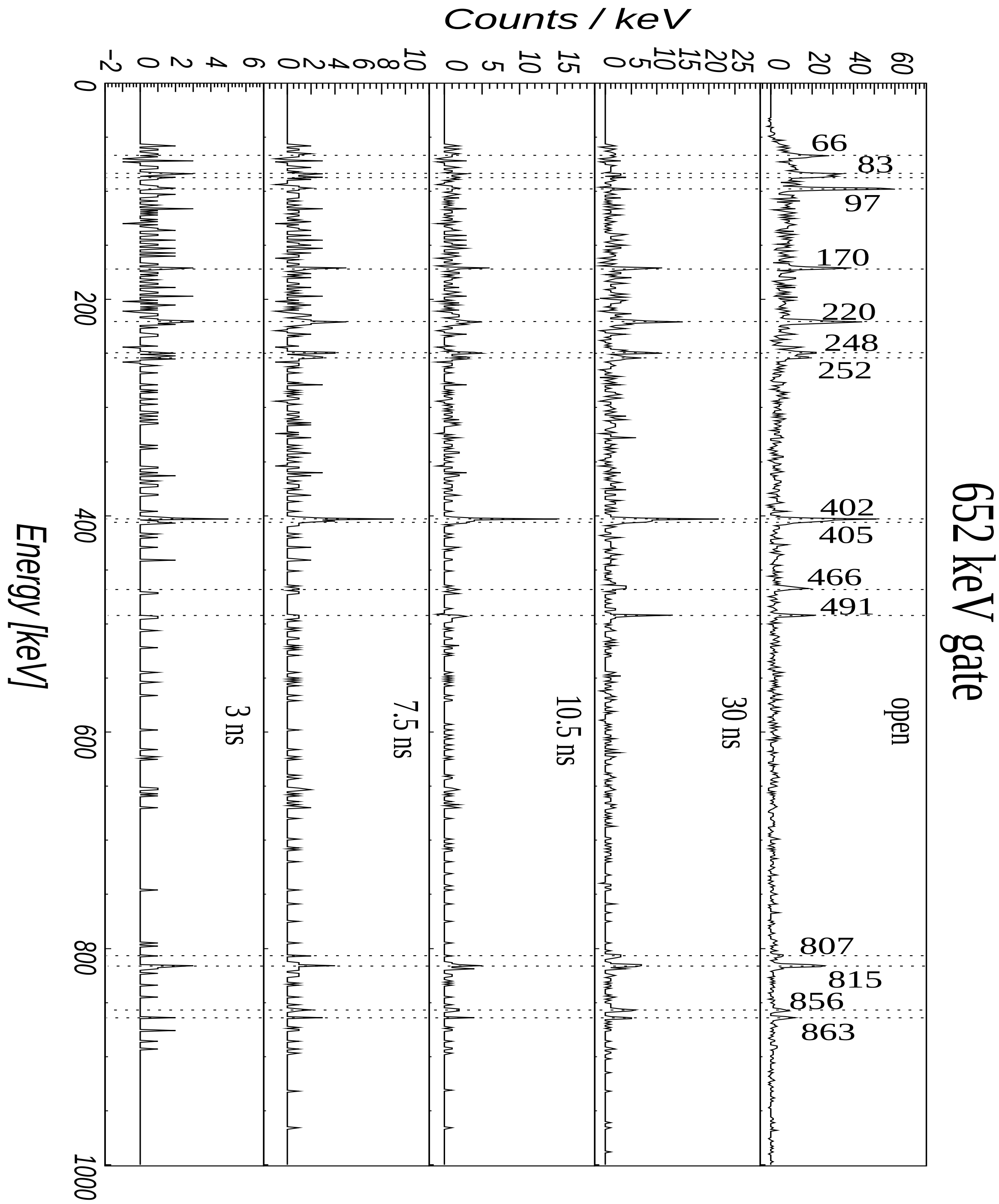


Figure 5.1: *$\gamma$ energy spectra extracted from the $\gamma\gamma$ matrices gated on the 652 keV transition in $^{128}$Cd. The time difference between two coincident $\gamma$ rays conditions applied to the matrices is shown in each spectrum.*

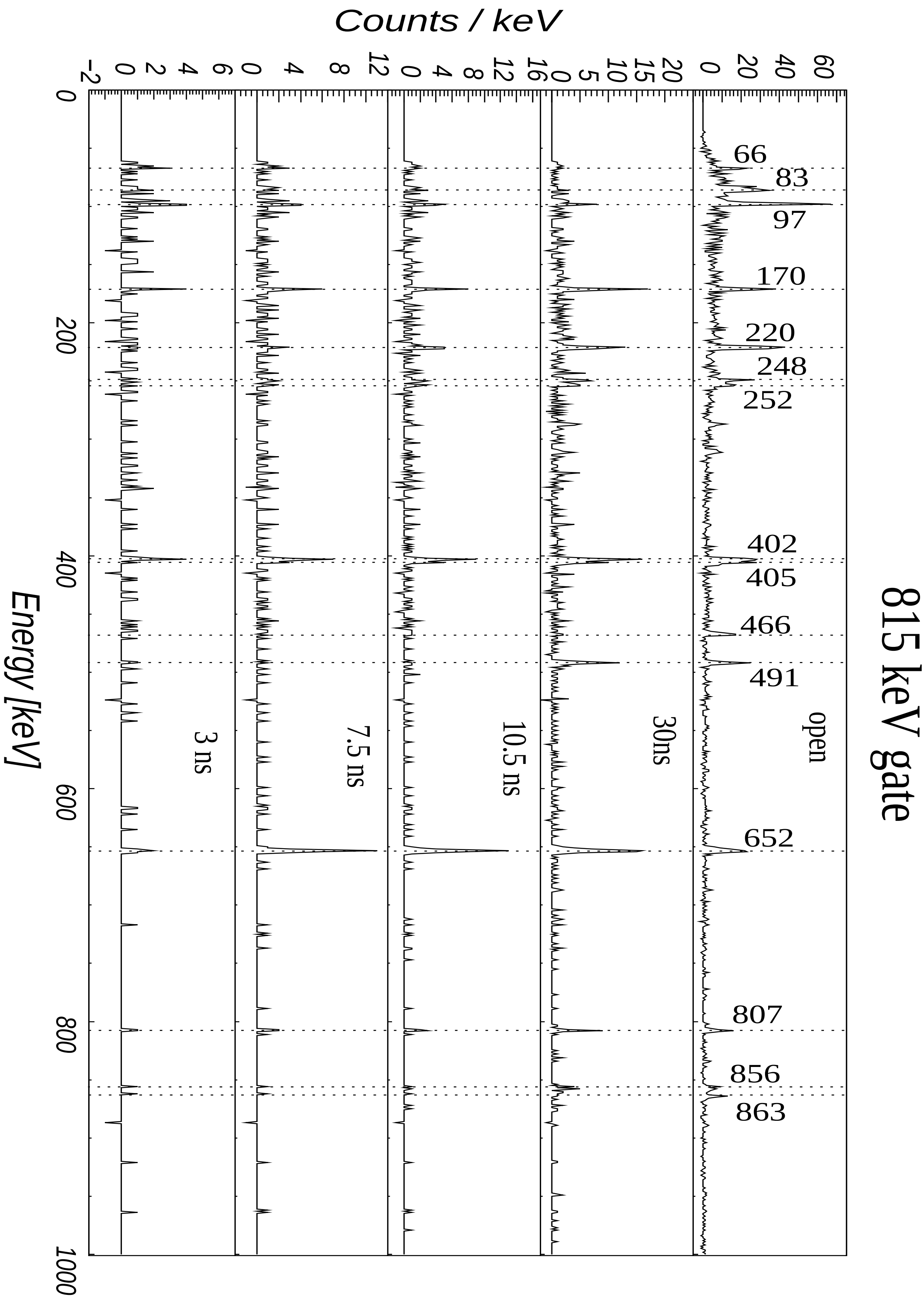


Figure 5.2: *$\gamma$ energy spectra extracted from the $\gamma\gamma$ matrices gated on the 815 keV transition in $^{128}$Cd. The time difference between two coincident $\gamma$ rays conditions applied to the matrices is shown in each spectrum.*

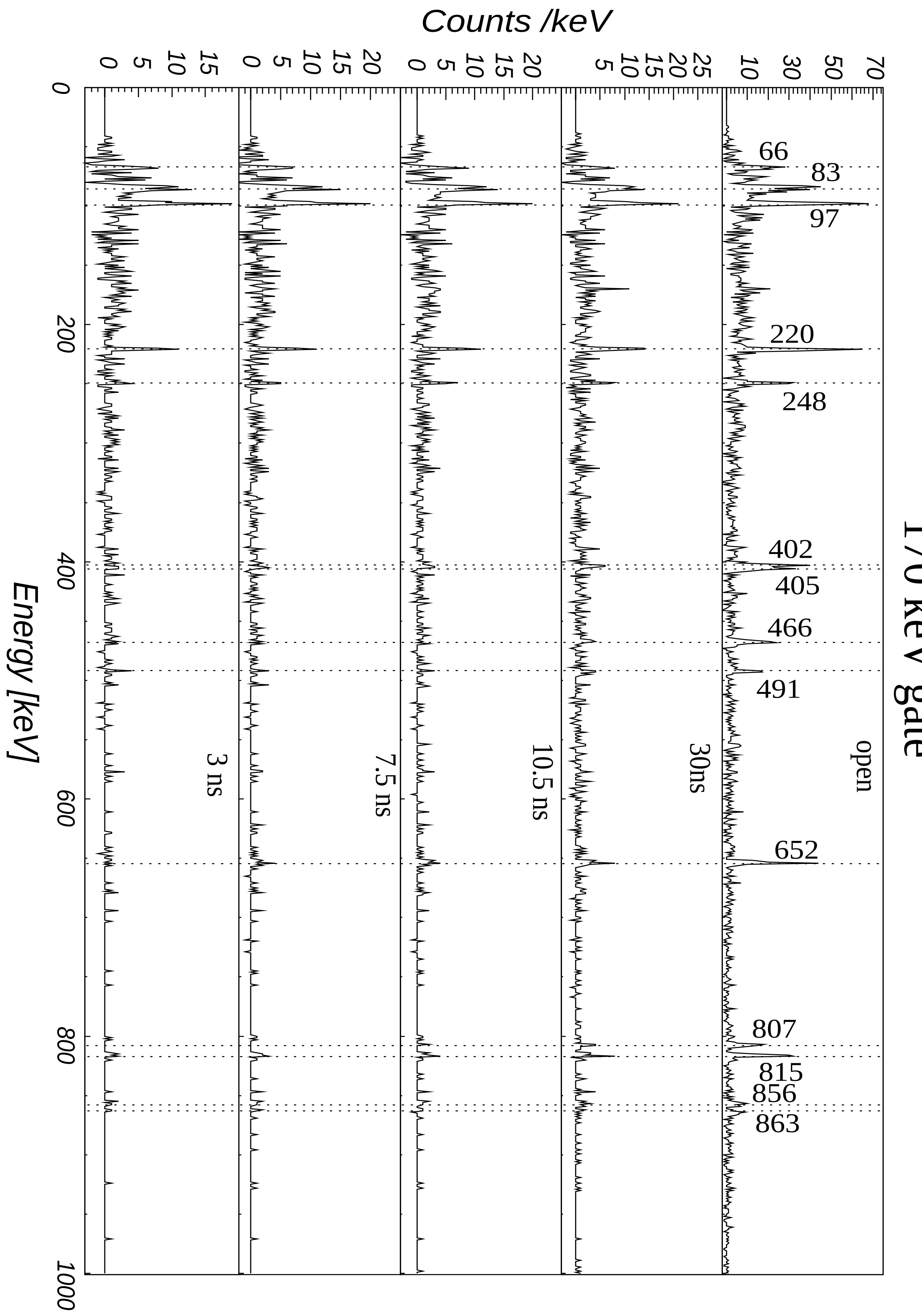


Figure 5.3: *$\gamma$ energy spectra extracted from the $\gamma\gamma$ matrices gated on the 170 keV transition in $^{128}$Cd. The time difference between two coincident $\gamma$ rays conditions applied to the matrices is shown in each spectrum.*

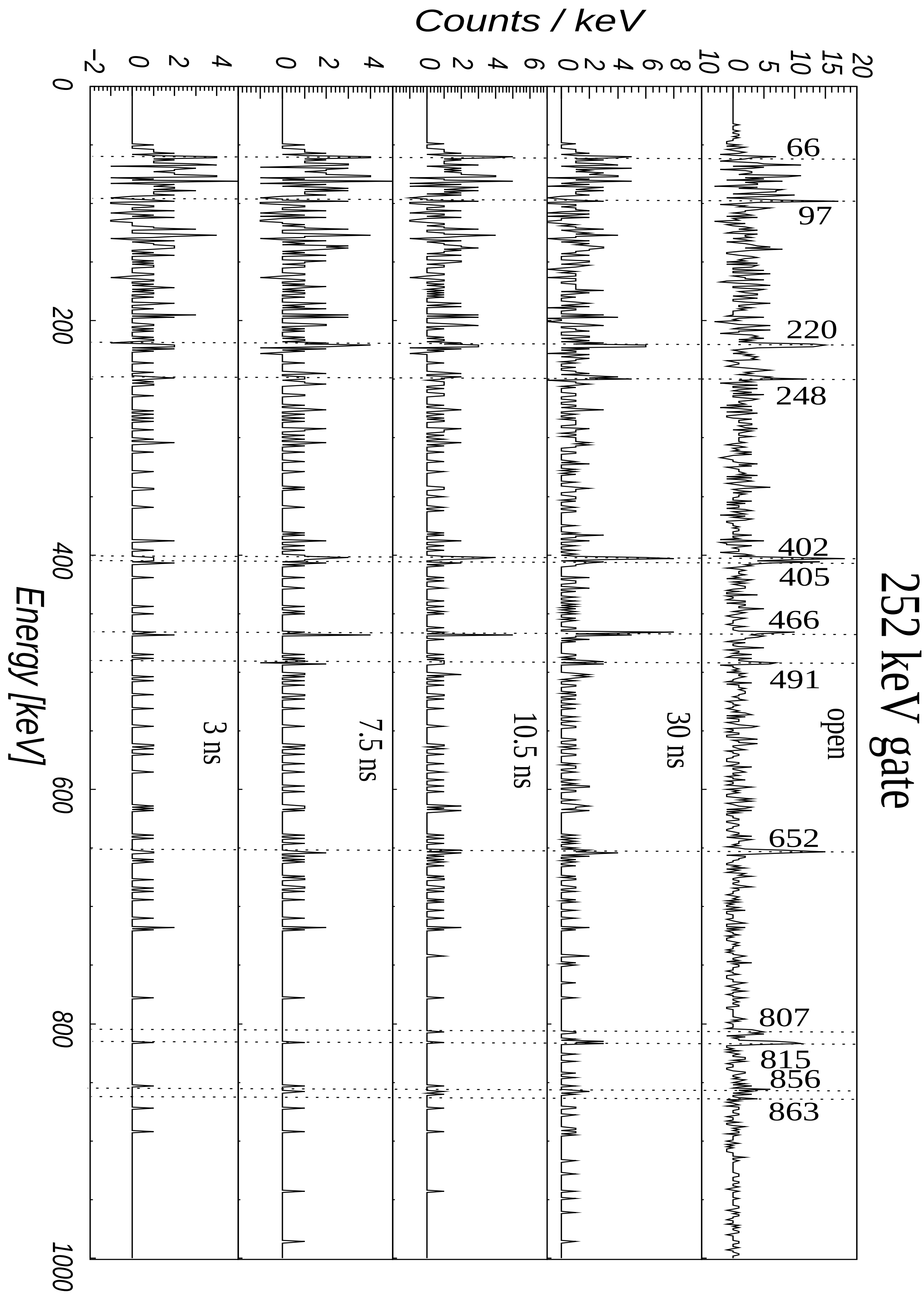


Figure 5.4: *$\gamma$ energy spectra extracted from the $\gamma\gamma$ matrices gated on the 252 keV transition in $^{128}$Cd. The time difference between two coincident $\gamma$ rays conditions applied to the matrices is shown in each spectrum.*

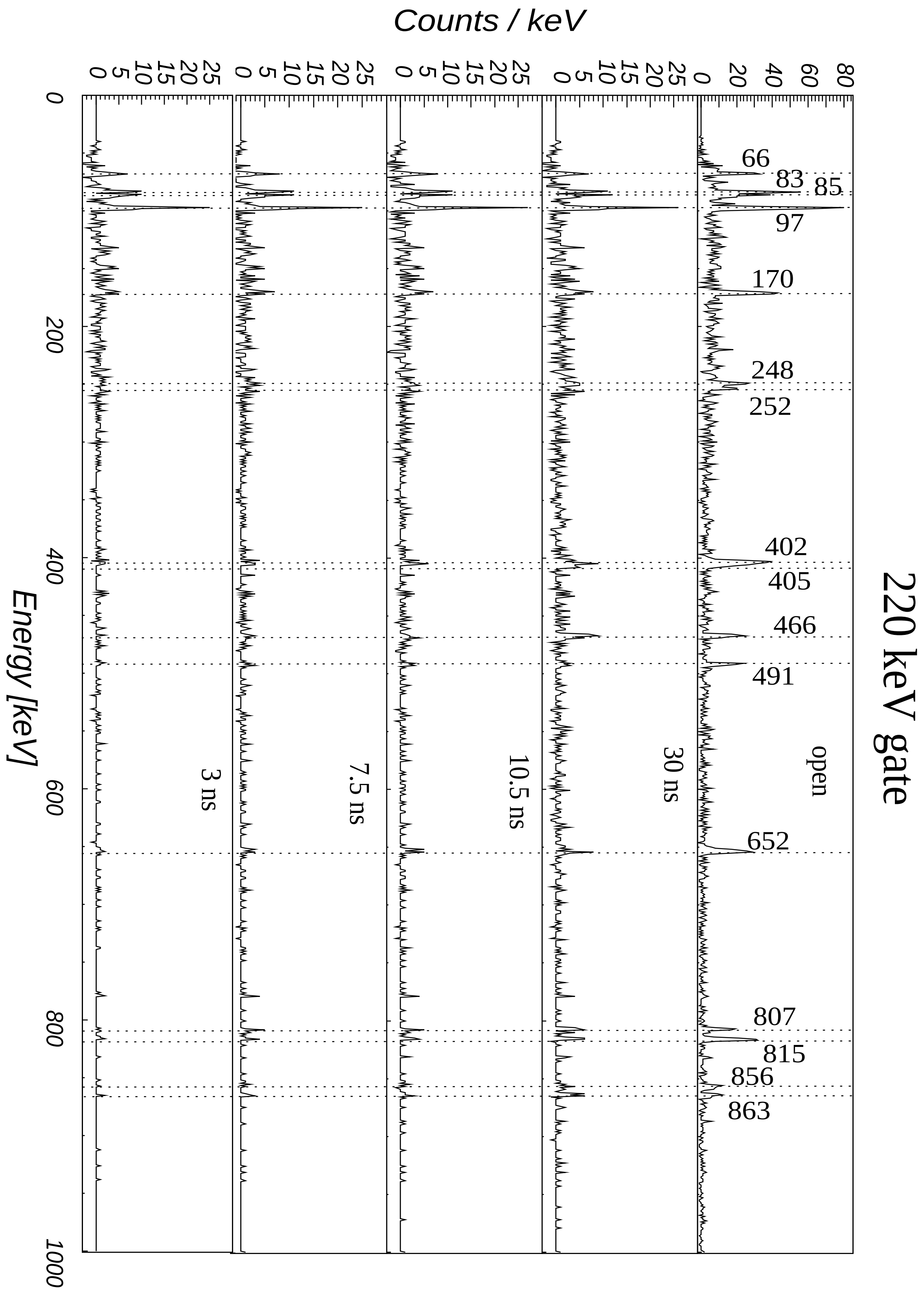


Figure 5.5: *$\gamma$ energy spectra extracted from the $\gamma\gamma$ matrices gated on the 220 keV transition in $^{128}$Cd. The time difference between two coincident $\gamma$ rays conditions applied to the matrices is shown in each spectrum.*

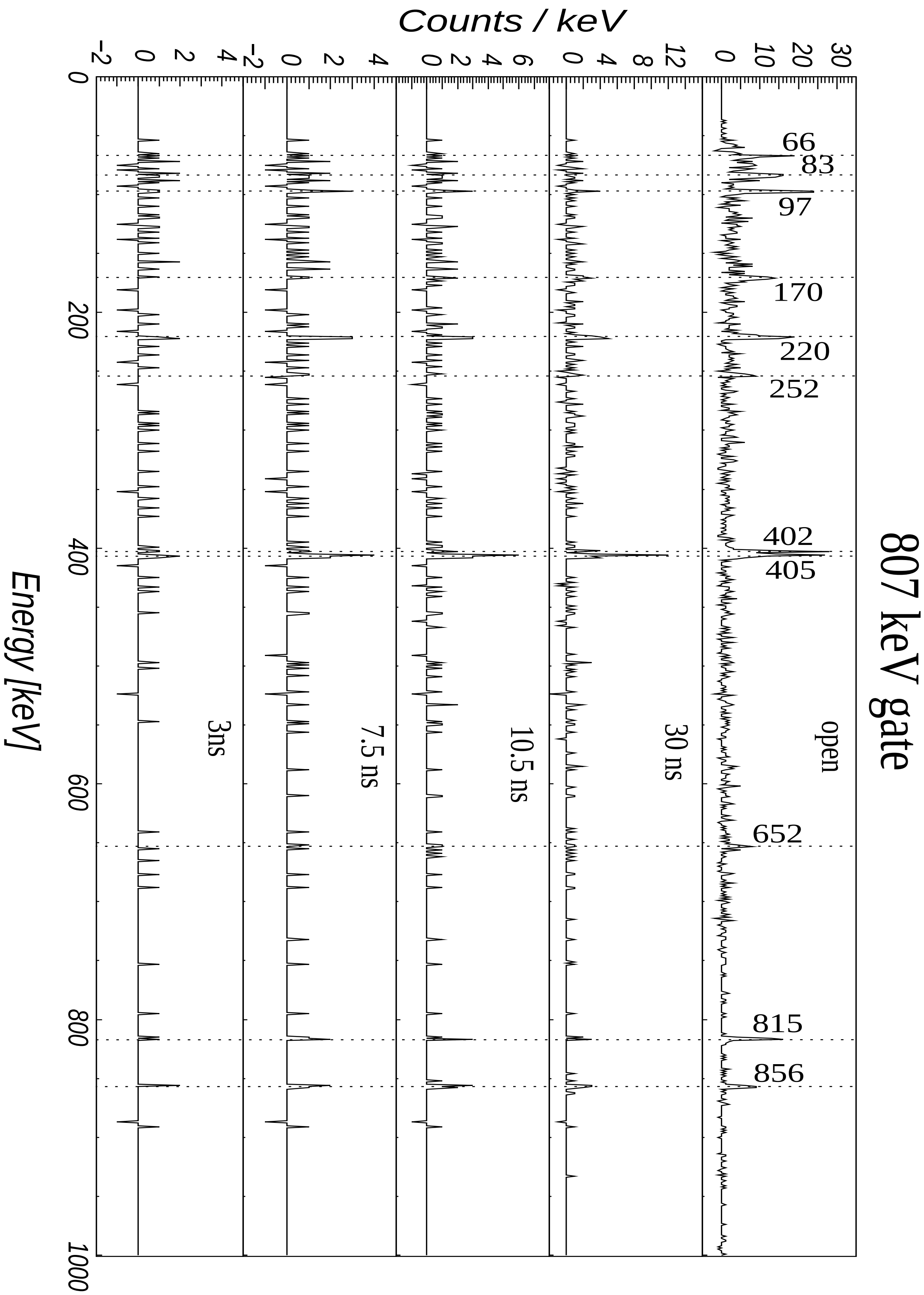


Figure 5.6: *$\gamma$ energy spectra extracted from the $\gamma\gamma$ matrices gated on the 807 keV transition in $^{128}Cd$. The time difference between two coincident $\gamma$ rays conditions applied to the matrices is shown in each spectrum.*

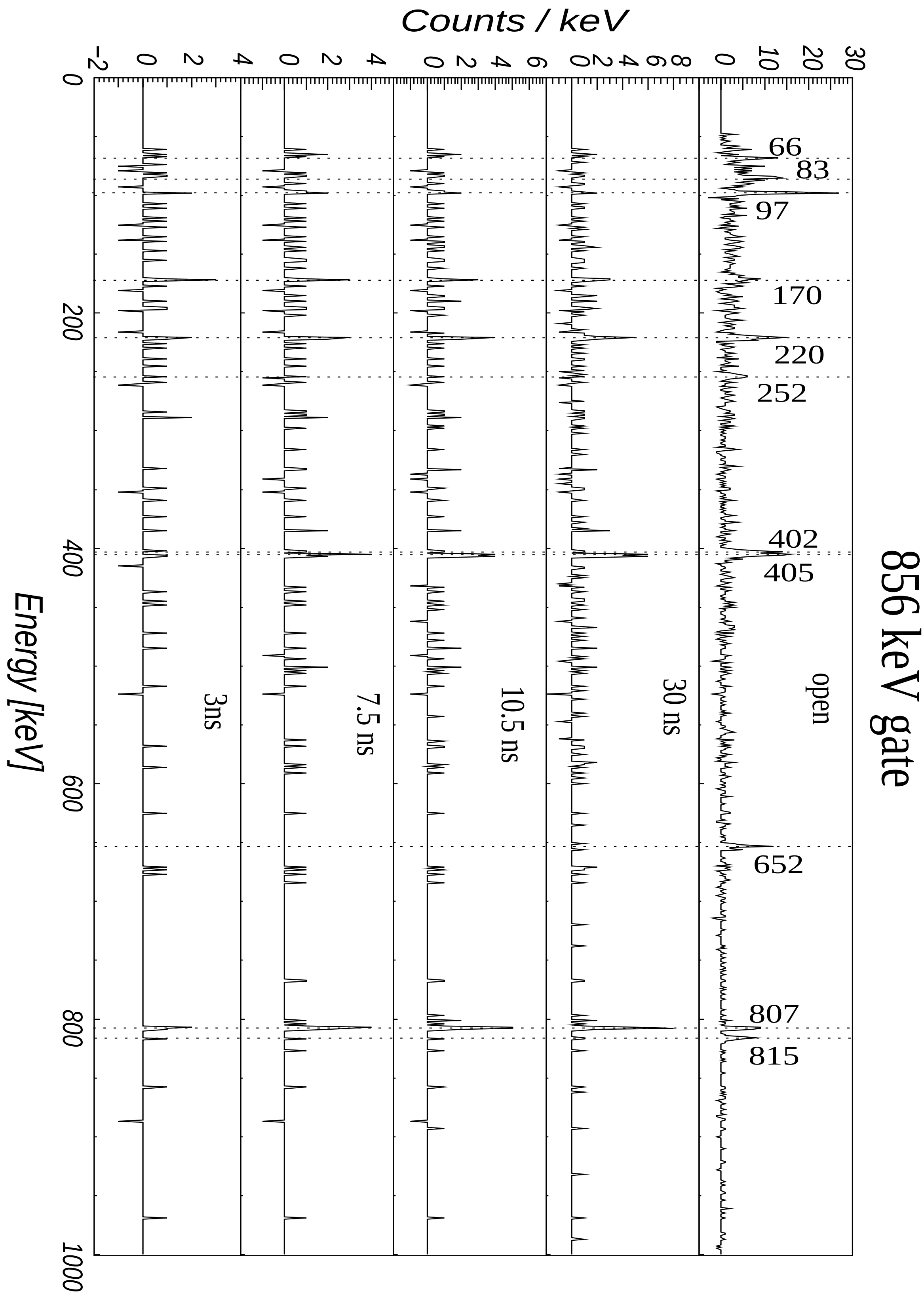


Figure 5.7: *$\gamma$ energy spectra extracted from the $\gamma\gamma$ matrices gated on the 856 keV transition in $^{128}$Cd. The time difference between two coincident $\gamma$ rays conditions applied to the matrices is shown in each spectrum.*

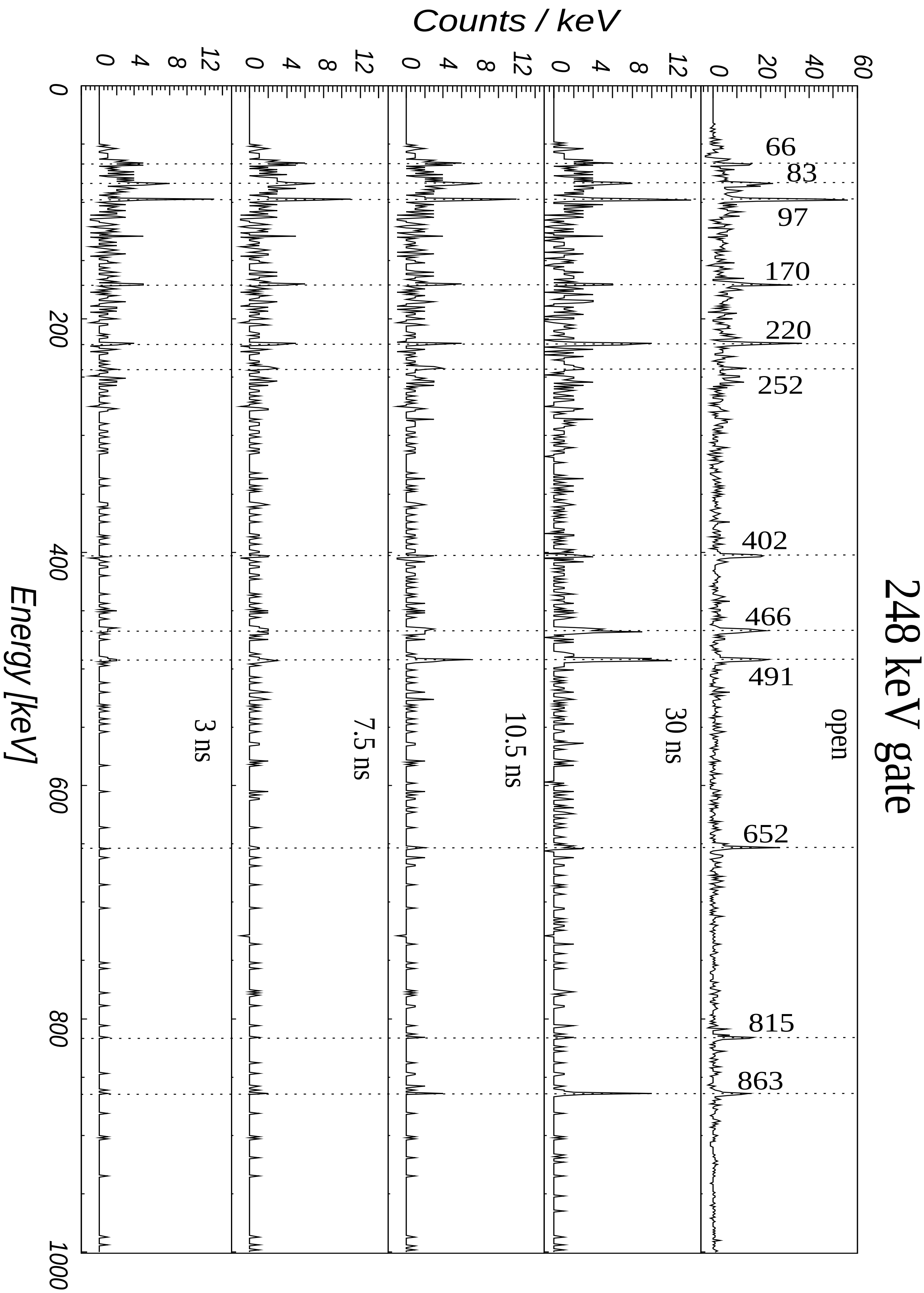


Figure 5.8: *$\gamma$ energy spectra extracted from the $\gamma\gamma$ matrices gated on the 248 keV transition in $^{128}$Cd. The time difference between two coincident $\gamma$ rays conditions applied to the matrices is shown in each spectrum.*

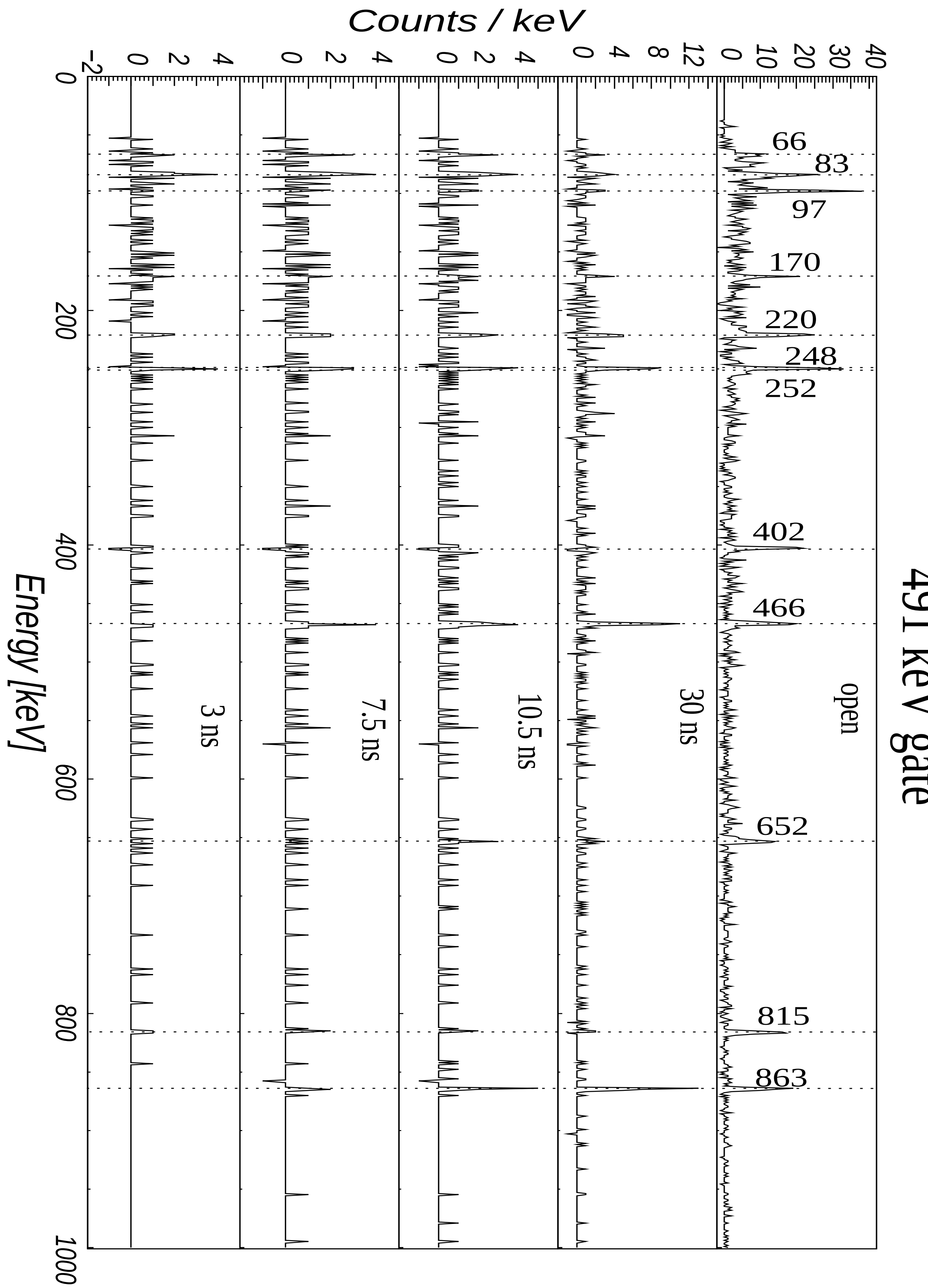


Figure 5.9: *$\gamma$ energy spectra extracted from the $\gamma\gamma$ matrices gated on the 491 keV transition in $^{128}$Cd. The time difference between two coincident $\gamma$ rays conditions applied to the matrices is shown in each spectrum.*

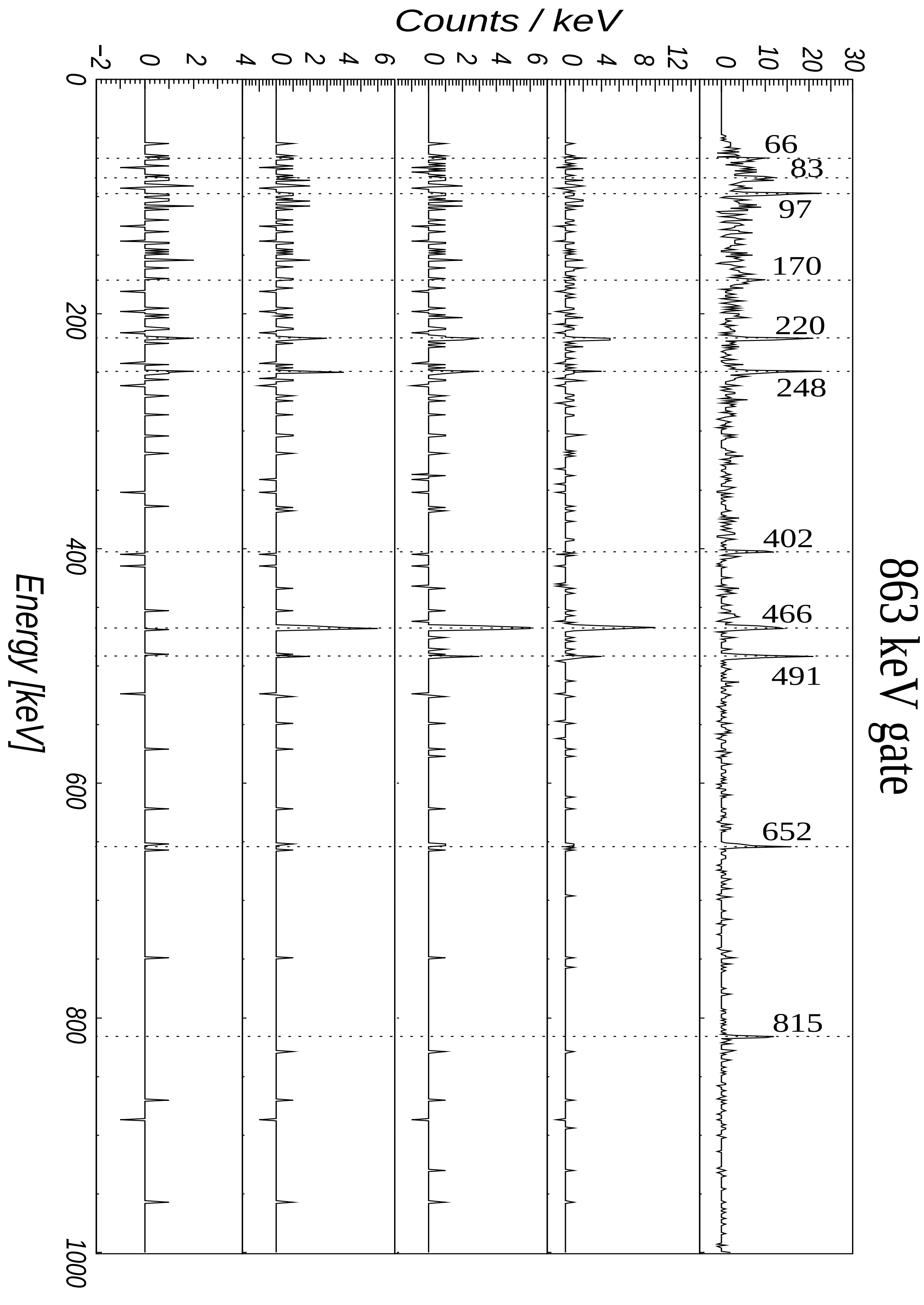


Figure 5.10: *$\gamma$ energy spectra extracted from the $\gamma\gamma$ matrices gated on the 863 keV transition in $^{128}$Cd. The time difference between two coincident $\gamma$ rays conditions applied to the matrices is shown in each spectrum.*

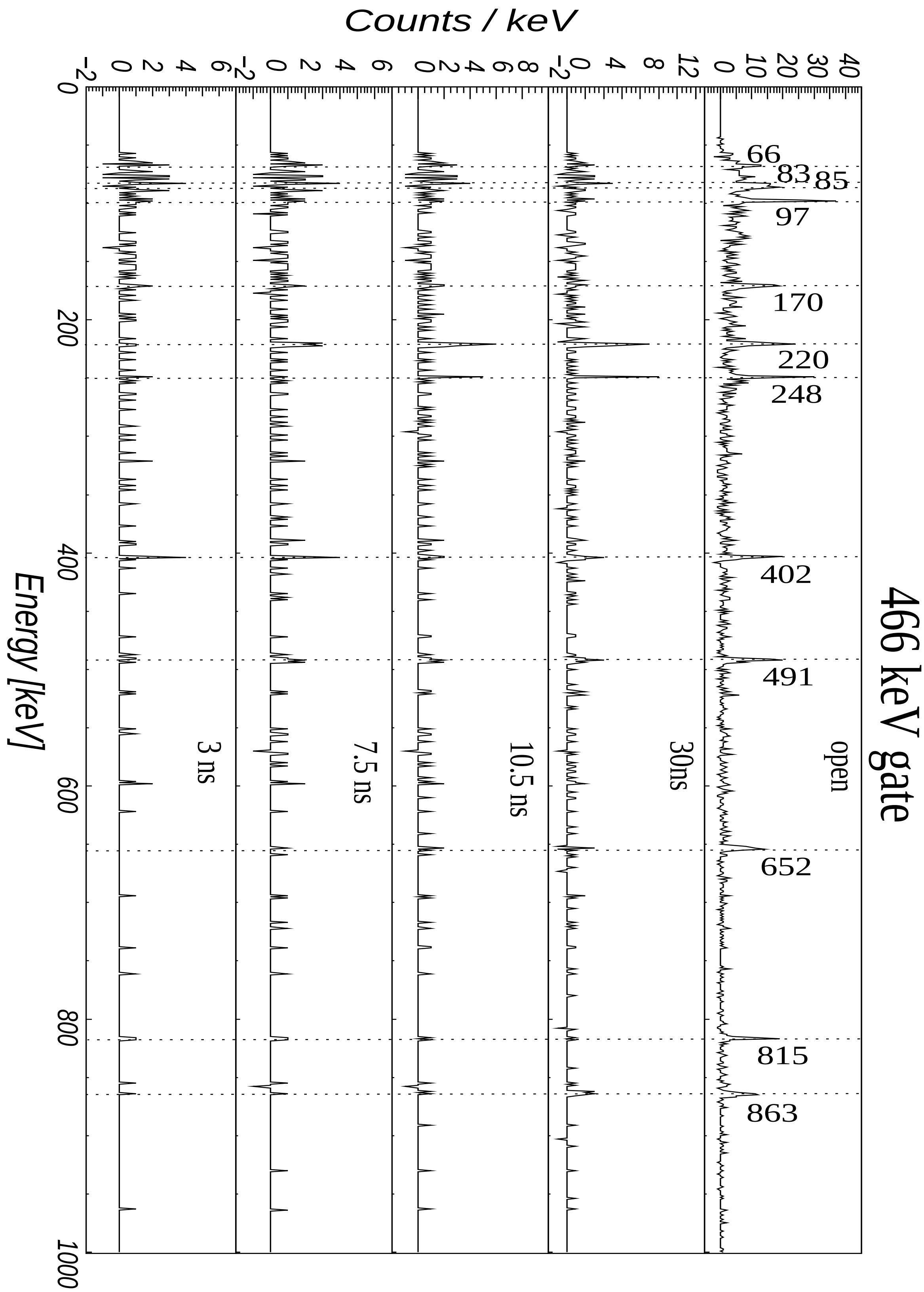


Figure 5.11: *$\gamma$ energy spectra extracted from the $\gamma\gamma$ matrices gated on the 466 keV transition in $^{128}$Cd. The time difference between two coincident $\gamma$ rays conditions applied to the matrices is shown in each spectrum.*

# Apendix B: Time distributions of the $\gamma$ lines observed in the $^{126}$Cd isomeric decay

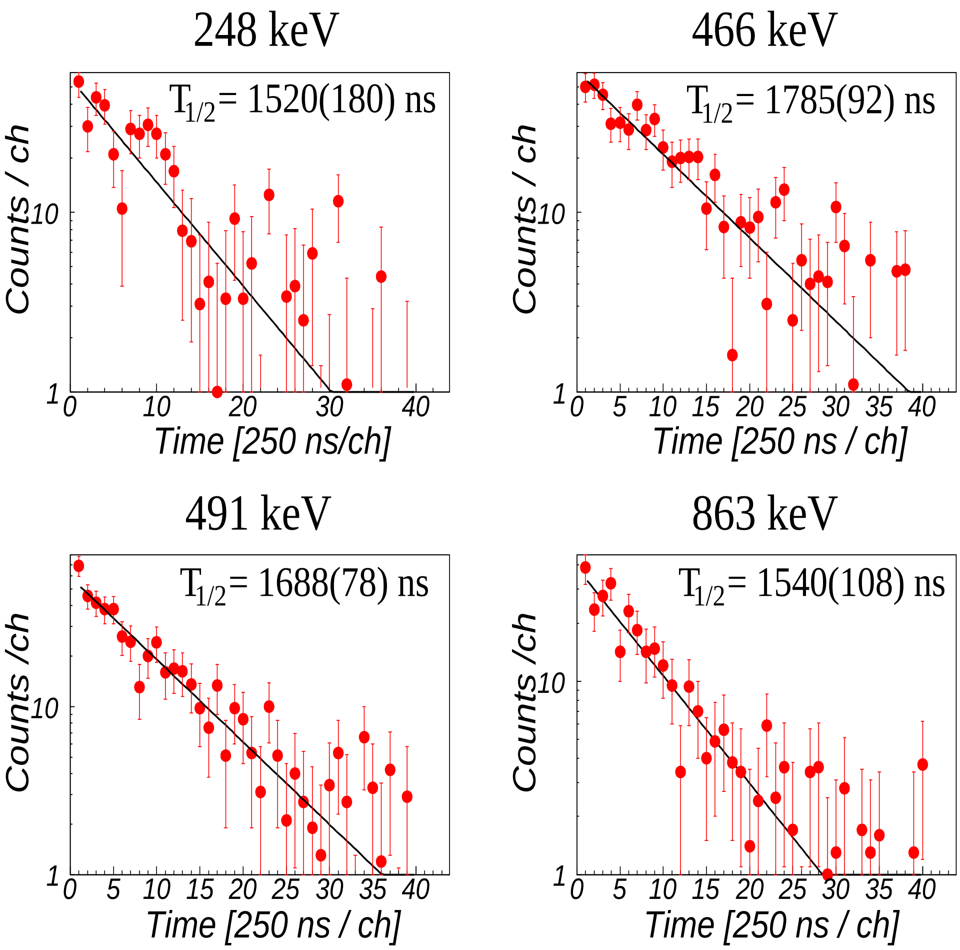


Figure 5.12: *Time distributions of the 248 keV, 466 keV, 491 keV and 863 keV transitions with respect to $^{126}$Cd implantation.*

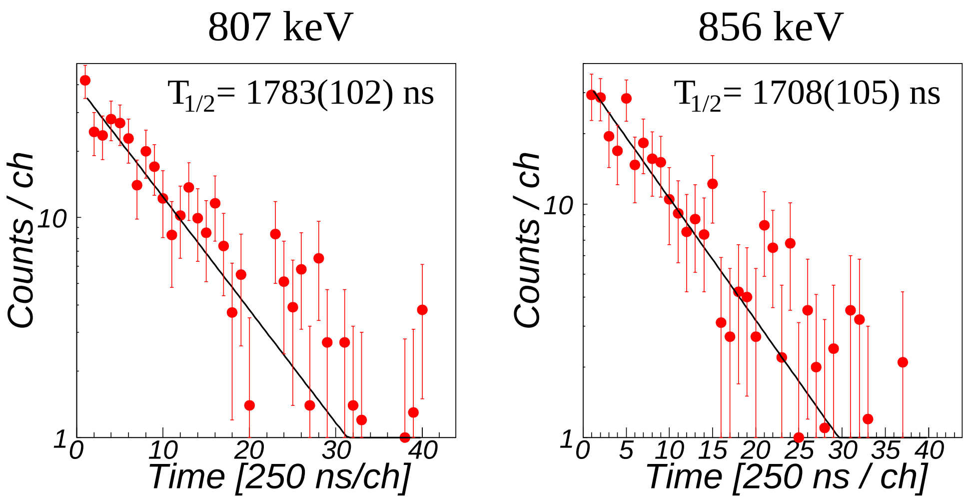


Figure 5.13: *Time distributions of the 807 keV (left) and 856 keV (right) transitions with respect to* $^{126}Cd$ *implantation.*

# Acknowledgments

El camino ya ha terminado y con ello se llega al final de un projecto que empezó hace ya cuatro anos. Tengo que reconocer que no ha sido un camino fácil algunas veces, pero la alegría que le invade a uno cuando consigue ver la transición tan esperada y luchada, creo, en mi opinión, que merece la pena todos los esfuerzos y frustraciones. Una tesis no es solamente el trabajo del alumno, se necesita bastante apoyo y ayuda de personas con más experiencia. Empiezo aquí mis agradecimientos, que van en primer lugar a Andrea Jungclaus y Magdalena Gorska, mis dos jefas. Ha sido muy interesante trabajar con las dos en paralelo. Ambas tienen un punto de vista muy diferente e interesante, dándome la oportunidad de mirar las cosas desde diferentes persperctivas, por ello digo, gracias. Esta tesis no hubiese sido realizada sin la ayuda de Robert, que me apoyo justo al principio cuando estaba intentando conseguir la posicion en la GSI. Tambien mis agradecimientos van hacia Michael Maier, con el que compartí tres anos y que siempre me apoyo en los momentos que buscas el sentido, y en los momentos en los que lo encuentras, preparandome la comida para las "night shift" y esperandome cada vez que se me hacia tarde en el trabajo, gracias de todo corazón. Plamen, todas las peleas que hemos tenido hablando de física....como nos gustan nuestras charlas, así es como siempre hemos encontrado la motivación y la diversión del trabajo, creo que hacemos un buen equipo y estoy segura de que seguiremos colaborando. A todas las personas de RISING, poner el nombre de todos sería una lista the 50 personas...como en todos los artículos ;D. Tengo que reconocer que me siento orgullosa de haber pertencido a la colaboración. Entre ellas me gustaría destacar Andrés Gadea, que me dió la oportunidad de presentar el proposal conjuntamente confiando en mis capacidades, gracias. A Hans-Jurgen y Jurgen, siempre dispuestos a escuchar mis charlas de entrenamiento. Paddy, por su energia, Zsolt por su paciencia, Alejandro por su amabilidad...hay tanta gente, que sería como escribir otra tesis completa. Pero aun así, me gustaría agradecer a Hubert Grawe la ayuda con los artículos y todas las conversaciones interesantes, he aprendido mucho escuchándole. En esta lista de agradecimientos no podria faltar Marek, al que considero un gran amigo y cientifico. También se lo agradezco a las "power puff girls", chicas, ya somos mayores...;D pero "supernenas to the power". Antes de terminar esta ultima seccion de la tesis, querria decirles a mis padres gracias por su apoyo y dedicacion, dandome la fuerza interna necesaria para poder realizar este trabajo... Por último quiero agradecerle y dedicarle esta tesis a Xavier Lopez, SuperLopex. Sin él no lo hubiese conseguido, el apoyo, la energía y la referencia para hacer un buen trabajo, realmente no tengo palabras para expresar lo que significa para mi. My life, my love, my soul...

# Bibliography


[1] M. Goepper-Mayer, Phys. Rev. 74, 235 (1948).

[2] M. Goepper-Mayer, Phys. Rev. 75, 1969 (1949).

[3] M. Goepper-Mayer, Phys. Rev. 78, 16 (1950).

[4] O. Haxel, J. H. D. Jensen and H. E. Suess, Phys. Rev. 75, 1776 (1949).

[5] P. J. Brussaard and P. W. M. Glaudemans, Shell-Model application in Nuclear Spectroscopy, North-Holland, Amsterdam, p.5 (1977).

[6] H. Grawe, The euroschool lectures on Physics with Exotic Beams, Vol. 1, p. 33 (2004).

[7] P. Navratil and B.R. Barret, Phys. Rev. C57, 3119 (1998).

[8] B. R. Barret, P. Navratil and J. P. Vary, Nucl. Phys. A 704, 254c (2002).

[9] R. F. Casten, Nuclear Structure from a Simple Perspective, Oxford University Press Inc., New York, p. 144 (2000).

[10] R. Gross and A. Frenkel, Nucl. Phys. A 267, 85 (1976).

[11] B. A. Brown, B. H. Wildenthal, Ann. Rev. of Nucl. Part. Sci. 38, 29 (1988).

[12] K. Heyde, The Nuclear Shell Model, Springer, Berlin, 1994.

[13] P. J. Brussaard and P. W. M. Glaudemans, Shell-Model application in Nuclear Spectroscopy, North-Holland, Amsterdam, p. 132 (1977).

[14] E. Caurier, G. Martínez-Pinedo, F. Nowacki, A. Poves and A. P. Zuker, Rev. Modern Phys. 77, No 2 (2005).

[15] P. J. Brussaard and P. W. M. Glaudemans, Shell-Model application in Nuclear Spectroscopy, North-Holland, Amsterdam, p.176 (1977).

[16] P. J. Brussaard and P. W. M. Glaudemans, Shell-Model application in Nuclear Spectroscopy, North-Holland, Amsterdam, p.187 (1977).

[17] Aa. Bohr, B. R. Mottelson, Nuclear Structure vol. I, I. Benjamin, New York, p. 379-389 (1969).

[18] V. F. Weisskopf, Phys. Rev. 83, 1073 (1951).

[19] P. J. Brussard and P. W. M. Glaudemans, Shell-Model application in Nuclear Spectroscopy, North-Holland, Amsterdam, p.199 (1977).

[20] Aa. Bohr, B. R. Mottelson, Nuclear Structure vol. I, I. Benjamin, New York, p. 83 (1969).

[21] P. J. Brussaard and P. W. M. Glaudemans, Shell-Model application in Nuclear Spectroscopy, North-Holland, Amsterdam, p. 9 (1977).

[22] I. S. Towner, F. C. Khanna, Nucl. Phys. A 399, 344 (1983).

[23] K. H. Maier et al., Nucl. Phys. A 183, 289 (1972).

[24] H. Grawe, H. H. Bertschat, H. Hass, Hyperfine Interactions 15/16, 65 (1983).

[25] A. Kerek, G. B. Holm, S. Borg and P. Carlé, Nucl. Phys. A209, 520 (1973).

[26] B. Fogelberg, K. Heyde and J. Sau. Nucl. Phys. A 352, 157 (1981).

[27] M. Górska et al. Phys. Rev. Lett. 79, 2415 (1997).

[28] A. Blazhev et al., Phys. Rev. C 69, 064304 (2004).

[29] B. Fogelberg and P. Carlé. Nucl. Phys. A 323, 205 (1979).

[30] B. Fogelberg and J. Blomqvist, Nucl. Phys. A429, 205 (1984).

[31] B. Fogelberg et al., Phys. Rev. C70, 034312 (2004).

[32] H. Grawe, K. Langanke, and G. Martínez-Pinedo, Rep. Prog. Phys. 70, 1525 (2007).

[33] T. Otsuka et al., Phys. Rev. Lett. 95, 232502 (2005).

[34] J. Dowaczewski et al., Phys. Rev. Lett 72, 981 (1994).

[35] B. Fogelberg et al., Phys. Rev. C 70, 034312 (2004).

[36] H. Grawe et al., Eur. Phys. J A 25, s01 357 (2005).

[37] H. Grawe et al., Phys. Scr. T 56, 71 (1995).

[38] ENSDF database, http://www.nndc.bln.gov/ensdf/

[39] B. Fogelberg et al., Phys. Rev. C31, 1026 (1985).

[40] I. Dillmann et al., Phys. Rev. Lett. 91, 16 (2003).

[41] T. Kautzch et al., Eur. Phys. J A 9, 201 (2000).

[42] P. J. Brussaard and P. W. M. Glaudemans, Shell-Model application in Nuclear Spectroscopy, North-Holland, Amsterdam, p. 261 (1977).

[43] Aa. Bohr, B. R. Mottelson, Nuclear Structure vol. I, I. Benjamin, New York, p. 345 (1969).

[44] N. B. Gowe and M. J. Martin. Nucl. Data Tables 10, 205 (1971).

[45] B. S. Dzelepov, L. N. Zyryanova and Yu. P. Suslov. Beta Process, Leningrad, Nauka, 1972.

[46] J. C. Hardy, I. S. Towner, V. T. Koslowsky, E. Hagberg and H. Schmeing. Nucl. Phys. A 509, 429 (1990).

[47] E. Klempt et al., Z. Phys. C 37, 179 (1988).

[48] S. J. Freedman, Comments Nucl. Part. Phys. 19, 209 (1990).

[49] Aa. Bohr, B. R. Mottelson, Nuclear Structure vol. I, I. Benjamin, New York, p. 411 (1969).

[50] S. Raman et al., Phys. Rev. C 43, 556 (1991).

[51] M. Hannawald et al., Phys. Rev. C 62, 054301 (2000).

[52] C. E. Rolfs ans W. S. Rodney, Cauldrons in the Cosmos, The University of Chicago Press, p. 469 (1988).

[53] S. E. Woosley and E. Baron, Astrophys. J. 391, 228 (1992).

[54] B. S. Meyer, Astrophys. J. 343, 254 (1898).

[55] B. Chen et al., Phys. Lett. B 355, 37 (1995).

[56] B. Pfeiffer, K. -L. Kratz and F. -K. Thielemann, Z. Phys. A 357, 235 (1997).

[57] C. Freiburghaus et al., Astrophys. J. 516, 381 (1999).

[58] http://www-inj.gsi.de

[59] http://www.gsi.de/beschleuniger/sis18/sis.html

[60] A.S. Goldhaber, Phys. Lett. B 53, 306 (1974).

[61] H. Geissel and G. Münzenberg. Annu. Rev. Nucl. Part. Sci. 48, 1 (1998).

[62] K.-H. Schmidt et al., Phys. Lett. B 300, 313 (1993).

[63] J.J. Gaimard and K.H. Schmidt, Nucl. Phys. A 531, 709 (1991).

[64] D.J. Morrissey, Phys. Rev. C 39, 460 (1989).

[65] W.A. Friedman, Phys. Rev. C 27, 569 (1983).

[66] O. Tarasov, Nucl. Phys. A 734, 536 (2004).

[67] V. Borrel et al., z. Phys. A 314, 191 (1983).

[68] F. Rami et al., Nucl. Phys. A, 349 (1985).

[69] K. Sümmerer et al., Phys. Rev. C 42, 2546 (1990).

[70] K. Sümmerer and B. Blank, Phys. Rev. C 61, 034607 (2000).

[71] J. Benlliure, A. R. Junghans, and K.-H. Schmidt, Phys. J. A 13, 93 (2002).

[72] H. Geissel et al., Nucl. Instr. Meth. B 70, 286 (1992).

[73] http://www-linux.gsi.de/ weick/mocadi.

[74] http://www-linux.gsi.de/ weick/mocadi/wedge.html

[75] http://www-linux.gsi.de/ weick/atima.

[76] http://www-aix.gsi.de/ scheid/CHARGE.html

[77] http://groups.nscl.msu.edu/lise/lise.html

[78] H. Stelzer, Nucl. Instr. Meth. A 310, 103 (1991).

[79] A. Stolz and R. Schneider, Technical Manual Ionization Chamber MUSIC80 (2000).

[80] O. Frisch, British Atomic Energy Report BR-49 (1944).

[81] G. Knoll, Radiation Detection and Measurement, John Wiley and Sons Inc., New York (1979).

[82] J. Eberth et al., Nucl. Instrum. Methods Phys. Res. A 369, 135 (1996).

[83] J. Simpson, Z. Phys. A 358, 139 (1997).

[84] W. Korten and S. Lunardi, Achievements with the Euroball spectrometer 1997-2003 (2003).

[85] J. Gerl and R. M. Lieder, Euroball III Proposal, 1992.

[86] Zs. Podolyák et al., Nucl. Phys. A 722, 273 (2003).

[87] S. Pietri et al., Nucl. Instrum. Methods Phys. Res. B 261, 1079 (2007).

[88] http://www.caen.it/nuclear/product.php?mod=V767A&fam=vme&fun=tdc#

[89] http://www.xia.com/Manuals/Pixie16_UserManual1.0.6.pdf

[90] D. Forkel-Wirth, G. Bollen (Edts.). Hyperfine Int. 129 (2000).

[91] R. Bennett et al., NuPECC Report, April 2000, 1 (2000).

[92] U. Köster, Nucl. Phys. A 701, 441 (2002).

[93] J. Benlliure. Private comunications.

[94] N. Hoteling et al., Phys. Rev. C 76, 044324 (2007).

[95] A. Jungclaus et al., Phys. Rev. Lett. 99, 132501 (2007).

[96] W. Andrejtscheff et al., Nucl. Instrum. Methods 204, 123 (1982).

[97] W. B. Walters et al., Phys. Rev. C 70, 034314 (2004).

[98] T. Kautzsch et al., Eur. Phys. J. A 25, s01, 117 (2004).

[99] T. Kautzsch, W. B. Walters, K. -L. Kratz, and the ISOLDE-IS333-Collaboration, AIP Conf. Proc. No 447 (AIP, New York), p. 183 (1998).

[100] A. Scherillo et al., Phys. Rev. C 70, 054318 (2004).

[101] L. -E. De Geer and G. B. Holm, Phys. Rev. C22, 2163 (1980).

[102] M. Górska et al. submitted to Phys. Lett. B.

[103] R. Machleidt, F. Sammarruca, and Y. Song, Phys. Rev. C 53, R1483 (1996).

[104] M. Hjorth-Jensen, T. T. S. Kuo, and E. Osnes, Phys. Rep. 261, 125 (1995).

[105] A. Gniady et al., (to be published).

[106] A. Banu et al., Phys. Rev. C 72, 061305(R) (2005).

[107] G. Martínez-Pinedo and K. Langanke, Phys. Rev. Lett. 83, 4502 (1999); J. J. Cuenca-García et al., Eur. Phys. J. A 34, 99 (2007).

[108] K. Langanke and G. Martínez-Pinedo, Rev. Mod. Phys. 75, 819 (2003).

[109] O. Kavetsyuk et al., Eur. Phys. J. A 31, 319 (2007).

[110] A. Brown et al., MSU-NSCL Report No. 1289 (2004).

[111] E. K. Warburton, Phys. Rev. C 44, 233 (1991).

[112] J. Blomqvist, CERN Report No. 81-09, CERN, Geneva, p. 535 (1981).

[113] R. Lozeva et al., Phys. Rev. C 77, 064313 (2008).

[114] A. H. Wapstra, G. Audi, and C. Thibault, Nucl. Phys. A 729, 337 (2003).

[115] J. J. Cowan and C. Sneden, Nature 440, 1151 (2006).

[116] R. Machleidt et al., Phys. Rev. C **63** 024001 (2001)

[117] M. Hjorth-Jensen, T. T. S. Kuo and E. Osnes, Phys. Rep. 261 (3&4), 125 (1995).

[118] K. Sieja et al., K. Sieja, F. Nowacki, K. Langanke and G. Martínez-Pinedo, to be published.

[119] B. A. Brown, Prog. Part. Nucl. Phys. 47, 517 (2001).

# List of Tables

# List of Figures